Drag Reduction by Riblets & Sharkskin Denticles: A Numerical Study

A DISSERTATION
SUBMITTED TO THE FACULTY OF THE GRADUATE SCHOOL
OF THE UNIVERSITY OF MINNESOTA
BY

Aaron Boomsma

IN PARTIAL FULFILLMENT OF THE REQUIREMENTS
FOR THE DEGREE OF
DOCTOR OF PHILOSOPHY

Professor Fotis Sotiropoulos

July, 2015

Acknowledgements

I would like to thank my adviser Professor Fotis Sotiropoulos for his support, guidance, and patience over the past five years. Professor Sotiropoulos is a visionary and has a drive for excellence. I am inspired to foster these traits in my own life. I also would like to thank the committee members, Professors Terry Simon, Ellen Longmire, and Sean Garrick. I sincerely appreciate their time, effort, and valuable feedback.

This dissertation would not be possible without the members of our research group, Mohammad Hajit, Toni Calderer, Saurabh Chawdhary, Daniel Foti, Xiaolei Yang, Dionysus Angelidis, Trung Le Bao, Ali Khosronejad, & Seokoo Kang. I couldn't have asked for a better research group. The technical expertise of every member was instrumental in my research. I'm looking forward to a future with them as colleagues and friends.

I would like to thank George Lauder and Li Wen of the Lauder Laboratory for the opportunity to collaborate and for the denticle CAD model. I would also like to thank the staff at Sandia National Labs for their collaboration. During my Ph.D., I was fortunate to travel to the Sandia National Laboratory and use the RedMesa supercomputer. RedMesa was an integral part of my research. I particularly appreciate the mentorship of David Maniaci. I also want to express my gratitude to my coworkers at TSI Inc. for their encouragement as I've finished this dissertation. I have felt welcomed and appreciated, and I'm looking forward towards a future of development and innovation at TSI.

I would like to thank my father and mother, Steve and Julie Boomsma, for their tremendous support and sacrifice. They have expressed confidence in me from the very beginning. I love them both very much. I am thankful for my wife, Amanda Boomsma. She has shared the burdens of this Ph.D. and has selflessly set her goals aside so that I could work towards mine. Lastly, I want to thank my Lord and savior, Jesus Christ. He is

my rock and my salvation.

This research was made possible through a grant from the United States Department of Energy. Computational resources were provided by the Sandia National Laboratory and the Minnesota Supercomputing Institute.

Dedication

To my wife, Amanda. A capable, intelligent, and virtuous woman. Proverbs 31:10

Abstract

Riblet films are a passive method of turbulent boundary layer control that can reduce viscous drag. They have been studied with great detail for over 30 years. Although common riblet applications include flows with Adverse Pressure Gradients (APG), nearly all research thus far has been performed in channel flows. Recent research has provided motivation to study riblets in more complicated turbulent flows with claims that riblet drag reduction can double in mild APG common to airfoils at moderate angles of attack. Therefore, in this study, we compare drag reduction by scalloped riblet films between riblets in a zero pressure gradient and those in a mild APG using high-resolution large eddy simulations. In order to gain a fundamental understanding of the relationship between drag reduction and pressure gradient, we simulated several different riblet sizes that encompassed a broad range of s^+ (riblet width in wall units), similarly to many experimental studies. We found that there was only a slight improvement in drag reduction for riblets in the mild APG. We also observed that peak values of streamwise turbulence intensity, turbulent kinetic energy, and streamwise vorticity scale with riblet width. Primary Reynolds shear stresses and turbulence kinetic energy production however scale with the ability of the riblet to reduce skin-friction.

Another turbulent roughness of similar shape and size to riblets is sharkskin. The hydrodynamic function of sharkskin has been under investigation for the past 30 years. Current literature conflicts on whether sharkskin is able to reduce skin friction similarly to riblets. To contribute insights toward reconciling these conflicting views, Direct Numerical Simulations (DNS) are carried out to obtain detailed flow fields around realistic denticles. A sharp interface immersed boundary method is employed to simulate two arrangements of actual sharkskin denticles (from *Isurus oxyrinchus*) in a turbulent boundary layer at $Re_\tau \approx 180$. For comparison, turbulent flow over drag-reducing scalloped riblets is also simulated with similar flow conditions and with the same numerical method. Although the denticles resemble riblets, both sharkskin arrangements increase total drag by 44-50%, while the riblets reduce drag by 5%. Analysis of the simulated flow fields shows that the turbulent flow around denticles is highly three-dimensional and separated, with 25% of

the total drag being form drag. The complex three-dimensional shape of the denticles gives rise to a mean flow dominated by strong secondary flows in sharp contrast with the mean flow generated by riblets, which is largely two-dimensional. The so resulting three-dimensionality of sharkskin flows leads to an increase in the magnitude of the turbulence statistics near the denticles, which further contributes to increasing the total drag. The simulations also show that, at least for the simulated arrangements, sharkskin, in sharp contrast with drag-reducing riblets, is unable to isolate high shear stress near denticle ridges causing a significant portion of the denticle surface to be exposed to high mean shear.

Lastly, it has been theorized that sharkskin might act similarly to vortex generators and prevent separation. In order to test this theory, we have conducted simulations with and without sharkskin upstream of a steady separation bubble. Using large eddy simulation, our study shows that sharkskin worsened the weak separation region and enlarged the separation bubble's boundaries. The cause was shown to originate due to the denticles acting as blockages, rather than vortex generators. In fact, our results showed that separation occurred just after the second row of denticles and that the turbulent flow was unable to recover its lost momentum. Streamwise turbulence intensities were decreased compared to the baseline case. Finally, in the present case, the sharkskin induced reversed flow within the denticles–something that was not observed with sharkskin in channel flow.

Contents

List of Tables

List of Figures

Chapter 1

Literature Review

Most practical fluid flows are exposed to roughness. Roughness can vary in size and shape and depending upon these parameters, can have a profound effect on the boundary layer and the friction induced due to the no-slip boundary condition. Early investigations concerning roughness seems to be motivated by friction losses in pipe flows. Pioneers in pressure losses in pipes include Hagen [19], Darcy [20], and Weisbach [21]. Fittingly, today's fluid mechanists are familiar with the Darcy-Weisbach equation for pipe flow resistance and the Darcy friction factor. Of particular importance, is the work of Nikuradse [1]. Nikuradse systematically correlated the Darcy friction factor, f, with Reynolds numbers, Re, for a wide variety of roughness sizes. He accomplished this by gluing different sized sand grains onto pipe walls, then measuring the pressure losses and corresponding flow rates. His results, seen in Figure 1.1 show some important physical insights.

The first insight is that roughness doesn't have an affect on laminar boundary layer friction, i.e., Darcy friction factors depend solely on the Reynolds number. The second is that for each roughness height, there exists a region where friction factor is insensitive to changes in Reynolds number. Roughness in this region are said to be in a 'fully rough' flow. Third, there is a transitional region in which the friction factor is neither insensitive to roughness height or Reynolds number (transitional roughness). This has led to the following roughness classifications:

$$\frac{\epsilon u^*}{\nu} < 5\text{: hydraulically smooth roughness}$$
$$5 \leq \frac{\epsilon u^*}{\nu} \geq 70\text{: transitional roughness}$$

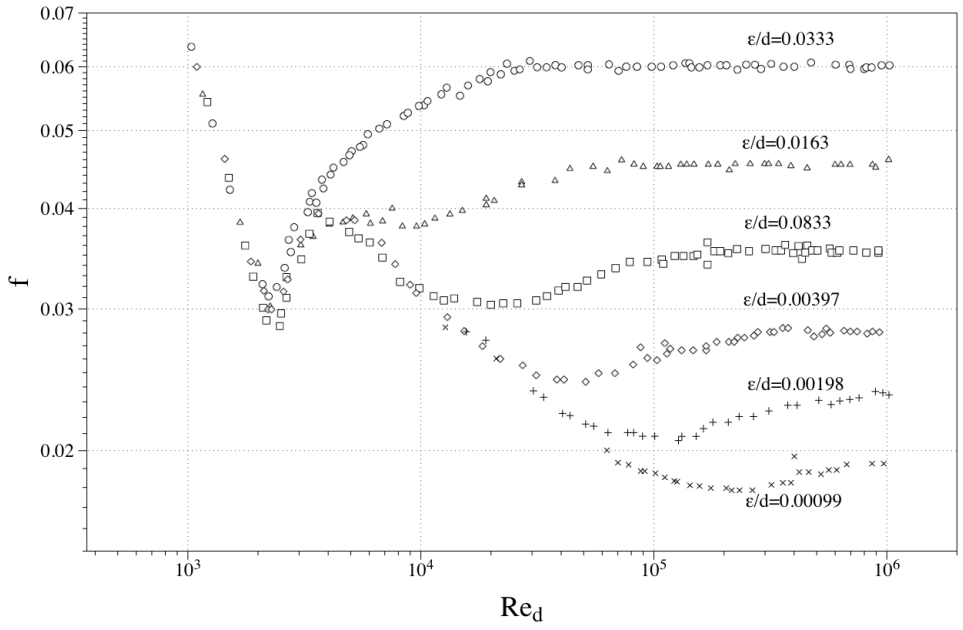

Figure 1.1: Experimental data from Nikuradse [1]. This plot shows the relationship between Darcy friction factor (vertical axis) and Reynolds number (horizontal axis).

$$\frac{\epsilon u^*}{\nu} > 70\text{: fully rough flow}$$

Perhaps even more well known than Nikuradse's results is the Moody diagram, which is essentially a plot of the work by Colebrook [22] to fully describe the relationship among friction factor, Reynolds number, and roughness size. Now, all this has been said to provide historical background and to relay an important point: *roughness typically increases the friction factor*, or at least the work of Nikuradse [1] has set such a trend. In fact, roughness nearly always augments drag in turbulent flows. Increased drag is a result of an increased wetted surface area, induced turbulent mixing, and additional form drag. However, it is possible that roughness can be used to actually *reduce* drag–and that is the primary subject of this dissertation.

In the following sections, past works concerning riblets (a drag reducing roughness) are reviewed. Mechanisms of drag reduction by riblets will be summarized. These sections are followed by a literature review concerning sharkskin (a roughness that resembles riblets). Finally, the objectives of the present research are presented.

1.1 Riblets in Turbulent Flows

The following sections detail past experimental and computational studies concerning riblets. Their inception, performance, mechanisms of drag reduction/augmentation, and application are described.

1.1.1 Background

Riblets are micro-grooved structures that are aligned in the primary direction of a turbulent flow. If sized and shaped correctly, riblets can reduce skin-friction drag by as much as 10%. Riblets were first conceived in the mid 1970s during a time of increasing energy costs. According to Walsh [23], R.L. Ash initially proposed the idea that streamwise fences could modify the boundary layer to reduce skin friction in 1976. The idea that near-wall coherent structures within the turbulent boundary layer could be modified to achieve drag reduction was likely influenced by the pioneering works of Kline et al. [24] and Brown & Roshko [25]. Riblet drag reduction, $\%DR$ is defined as follows:

$$\%DR = 100 \times \frac{F_{riblet} - F_{baseline}}{F_{baseline}} \tag{1.1}$$

In the above equation, the viscous force on the riblets is denoted by F_{riblet} and the baseline skin-friction, $F_{baseline}$ is the force on a surface without riblets.

Walsh [26], [27] pioneered the study of riblet performance and optimization in the early 1980s. He created a database of experimental results for several types of two-dimensional geometries, similar to those seen in Figure 1.2. Using a wind tunnel and a drag balance, Walsh [27] measured the drag reduction/augmentation and related it to characteristic lengths of the particular riblet geometry. Two of the most common lengths are h and s, and are defined in Figure 1.3. He found that the drag reduction/augmentation among different riblet shapes scaled well on the relationship between the riblet geometry and the flow condition to which they were subjected. Therefore, drag reduction is commonly plotted as a function of riblet height and width (plotted in wall coordinates), h^+ and s^+ , as defined in Equations 1.2 and 1.3. Although the optimum width for drag reduction varies with shape, in general, riblets achieve maximum drag reduction at a size near $s^+ \approx 15$.

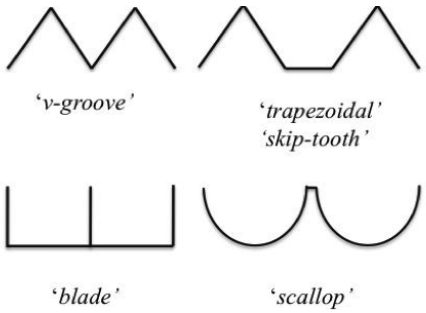

Figure 1.2: Common riblet geometries.

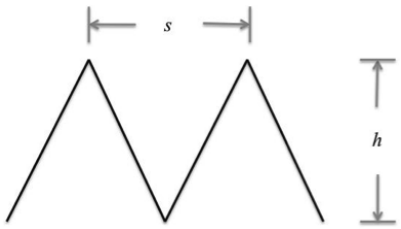

Figure 1.3: Riblet characteristic lengths: width, s and height h.

$$h^+ = hw_{\tau_0}/\nu \tag{1.2}$$

$$s^+ = hw_{\tau_0}/\nu \tag{1.3}$$

In these equations, $w_{\tau_0} = \sqrt{\tau_0/\rho}$ and τ_0 is the shear stress on a reference surface (i.e., a surface without riblets). It shouldn't be all that surprising that s^+ is a good non-dimensional scaling variable, as it is essentially a local (i.e., near-riblet) Reynolds number. Walsh [27] obtained a maximum drag reduction of 8% with two different geometries: 1) a v-groove riblet with $h^+ = 12, s^+ = 12$ and 2) a sharp-peaked scalloped geometry with $h^+ = 8, s^+ = 16$. Note how small the riblet structures are; just 8 to 16 wall units in length. More recently, Garcia-Mayoral & Jimenez [28] have shown that best scaling among riblet geometries occurs with the characteristic length, l^+, where $l = \sqrt{A_{cs}}$ and A_{cs} is the cross-sectional wetted area.

Figure 1.4 is a common plotting technique used to display the correlation between drag reduction and characteristic length. The vertical axis is the percentage of drag reduction

between the tested riblet geometry and a baseline smooth surface.

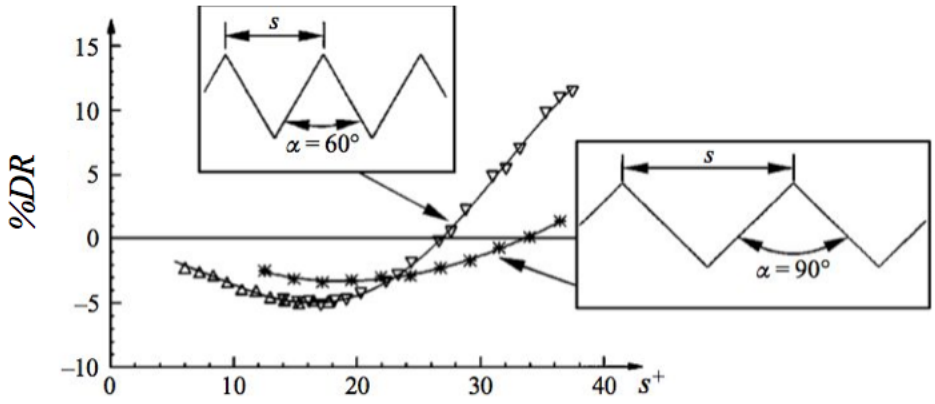

Figure 1.4: Riblet performance curve for v-groove type riblets. Experimental measurements from Bechert et al. [2].

Independent laboratories have added to Walsh's [27] database. Reidy et al. [29] used a water tunnel with a zero pressure gradient boundary layer in conjunction with laser Doppler velocimetry to measure a maximum drag reduction of 8.1% with a v-groove riblet with $h^+ =, s^+ = 13$. Bechert et al. [2] added several riblet performance curves to the literature by testing v-groove, scalloped, and blade shaped riblets in an oil-channel using a drag balance. He determined that the optimal riblet has a *blade* shape by testing progressively thinner trapezoidal riblets like those seen in Figure 1.2. Their corresponding curves are seen in Figure 1.5. The maximum drag reduction achieved with the blade riblet was approximately 10%, which occurred at $h/s = 0.5$ and $s^+ = 16$. Concerning riblets in zero pressure gradients or turbulent channel flow, 10% drag reduction is the largest value reported in the literature, aside from that of Coustols [30], whose measurements do not follow the dominant trends set by Walsh [27] or Bechert et al. [2].

Other than riblet cross-section shape, there are two more riblet geometric properties that are of importance. The first is the parameter, h/s, or the height to width ratio. Bechert et al. [2] tested a variety of ratios as seen in Figure 1.6 for the blade riblet. With this experimental data, it is apparent that $h/s = 0.5$ achieves the greatest drag reduction. There is another trend seen in Figure 1.6, and that is the breadth of the drag-reducing

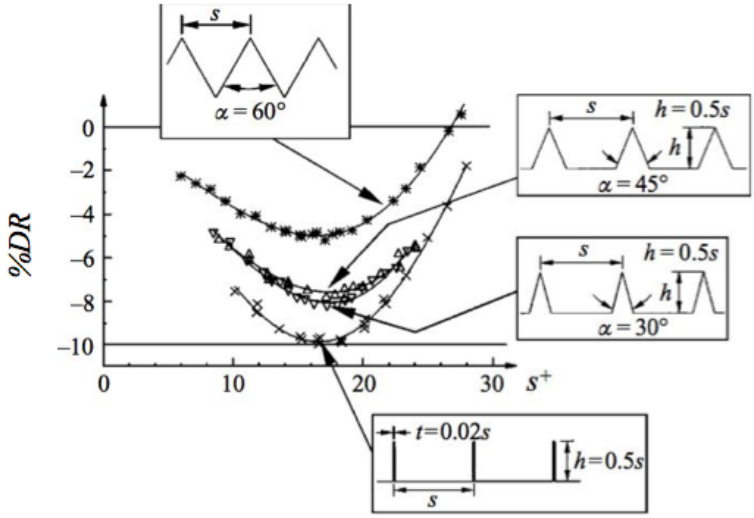

Figure 1.5: Optimization of riblet drag reduction, from v-groove to blade shaped riblets. Experimental measurements from Bechert et al. [2]

region. For example, if an application's w_{τ_0} is near-constant in time, an engineer might be comfortable in choosing $h/s = 0.5$ from Figure 1.6 in order to optimize for maximum drag reduction. However, if w_{τ_0} is known to be unsteady over a certain range, then choosing $h/s = 0.3$ might be a better choice, because the breadth of maximum drag reduction for $h/s = 0.3$ is greater than that of $h/s = 0.5$.

The last geometric parameter of importance is the ratio t/s, or the riblet tip thickness to width ratio. Again, referencing Bechert et al. [2], we see a trend develop in Figure 1.7. As t/s decreases, $\%DR$ increases. Unfortunately, this is more of a qualitative trend (rather than quantitative) due to the author's experimental apparatus. Apparently, the device that altered t/s leaked and did not fully align with the mean flow. After improving alignment and leakage, Bechert et al. [2] saw an improvement in $\%DR$. In other words, although there is evidence that $t/s = 0.02$ is an optimal ratio, due to the experimental ambiguity, it is just thought that as t/s decreases, $\%DR$ increases.

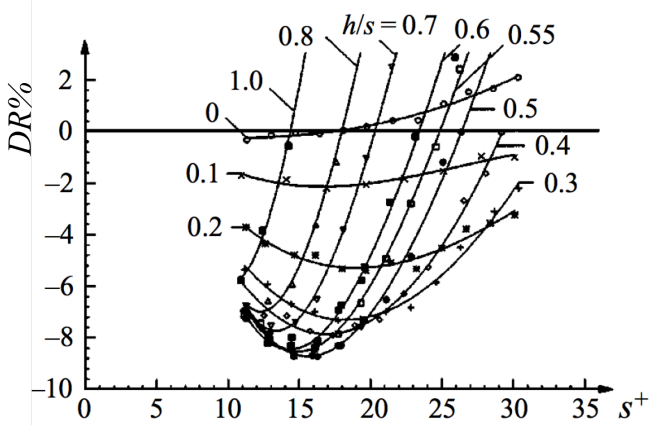

Figure 1.6: Optimization of riblet drag reduction at different h/s ratios for a blade-shaped riblet. Experimental measurements from Bechert et al. [2].

1.1.2 Drag Reduction Mechanisms

This foundation of previous work allows us to examine three distinct regions of a riblet performance curve, which are highlighted in Figure 1.8. The first section is called the viscous region and includes riblets that are nearly fully submerged in the viscous sublayer (almost hydrodynamically smooth). In this region, drag reduction scales linearly with increasing characteristic length. Luchini et al. [3] elucidated the viscous region in 1991. Realizing that the two-dimensional linear Stokes equations govern the flow within the fully submerged riblets, the authors found that riblets impeded cross-flow (spanwise) more that streamwise flow. Because of the no-slip condition, a shear flow exists near the riblet surface, just like that seen on a flat plate, and therefore, a riblet surface can be represented as a flat plate whose origin is somewhere inside the riblet. This *virtual origin* can be defined for both streamwise and spanwise velocities. The major finding of Luchini et al. [3] was that the virtual origin for the spanwise flow was deeper in the riblet than that of the streamwise virtual origin. The difference between these two origins is termed the protrusion height. Luchini et al. [3] argued that a larger protrusion height corresponded to a greater resistance to cross-flow. If cross-flow is hindered, the flow is less susceptible to secondary motion, which could otherwise increase shear by turbulent mixing. Bechert et al. [2] took this physical insight and used Prandtl's law of friction (for a smooth pipe) and the logarithmic portion for the law of the wall and developed Equation 1.4. This equation is plotted in

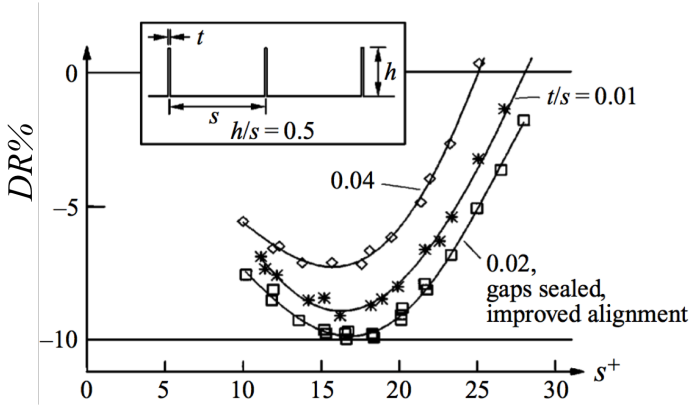

Figure 1.7: Optimization of riblet drag reduction at different t/s ratios for a blade-shaped riblet. Experimental measurements from Bechert et al. [2].

Figure 1.8 as the red dashed line.

In Equation 1.4, Δh corresponds to the protrusion height. As mentioned, this protrusion height is geometry dependent, and so must be calculated for a particular type of riblet. In Luchini et al. [3], the authors presented protrusion heights for a variety of shapes, as seen in Figure 1.9. Evidence that the ideal riblet is a blade shape can be seen from Figure 1.9. As the tip geometries become steeper, $\Delta h/s$ increases over the optimal range of h/s. Again, physically this means that the steeper the tip angle, the greater the impediment to secondary flow.

$$\frac{\Delta\tau}{\tau_0} = \frac{0.785\Delta h^+}{(2c_f)^{-1/2} + 1.25} \tag{1.4}$$

The second region of the performance curve (as seen in Figure 1.8) is the breakdown, or optimal, region. As riblets increase in size, they no longer just affect the viscous sublayer. Garcia-Mayoral & Jimenez [28] shed light on this region via successive Direct Numerical Simulations (DNS) of simple blade riblets. The authors determined that the breakdown is associated with spanwise vortices that appeared over the riblet surface. These rollers have a diameter around 150 wall units and are formed by a Kelvin-Helmholtz type instability of the mean streamwise velocity profile. Without transpiration (i.e., the no-slip condition) the viscous sublayer is stable and the instability isnt present. However, although riblets arent perforated, they do modify the sublayer and reportedly (see Choi et al. [13]) induce

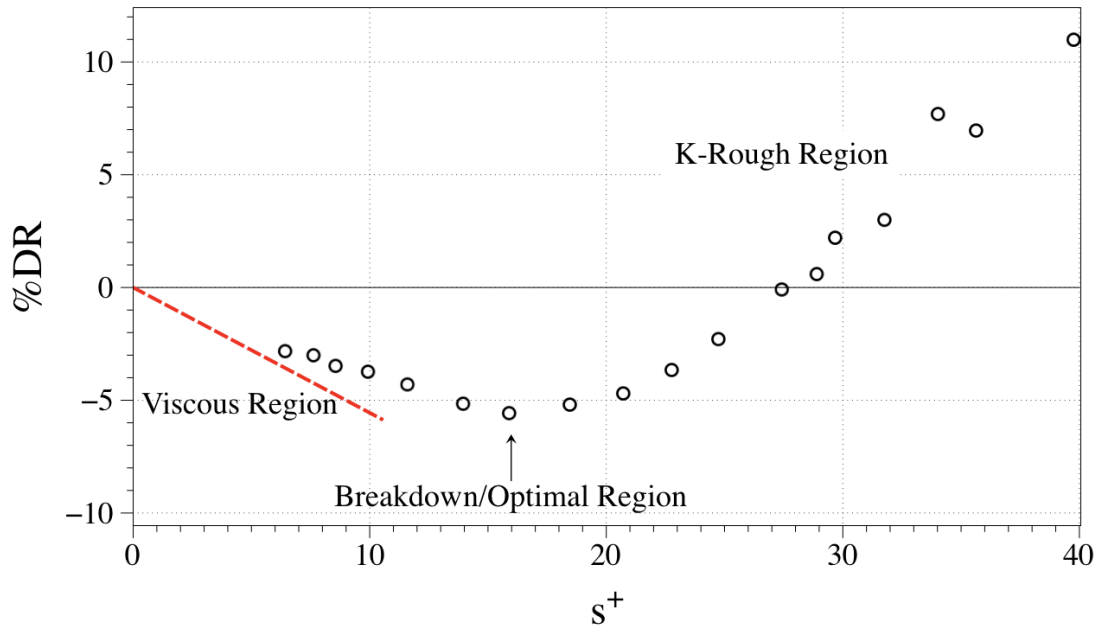

Figure 1.8: Distinct regions of the riblet performance curve. The dashed line is the corresponding viscous region prediction based on Equation 1.4

.

a local vertical flux, which makes the boundary layer less stable. Similar spanwise rollers have been documented over vegetable canopies and permeable walls (see Raupach et al. [31]). This secondary motion increases shear and causes a breakdown of the linearly scaling region.

The final region of the performance curve in Figure 1.8 is the K-rough region. A K-roughness is one that has an effective roughness height, k_s, that is proportional to the actual roughness dimensions. There is a distinction to be made; riblets are not a D-roughness. A D-roughness' k_s is proportional to the boundary layer height, δ. Equation 1.5 is often used to define k_s. To determine a value of k_s, the measured logarithmic region is plotted against Equation 1.5, varying k_s until a match is achieved. It is evident from Figure 1.8 that as the riblet size increases in this region, its drag also increases (which shifts the logarithmic region of the boundary layer, thus altering k_s). For the sake of brevity, the reader is referred

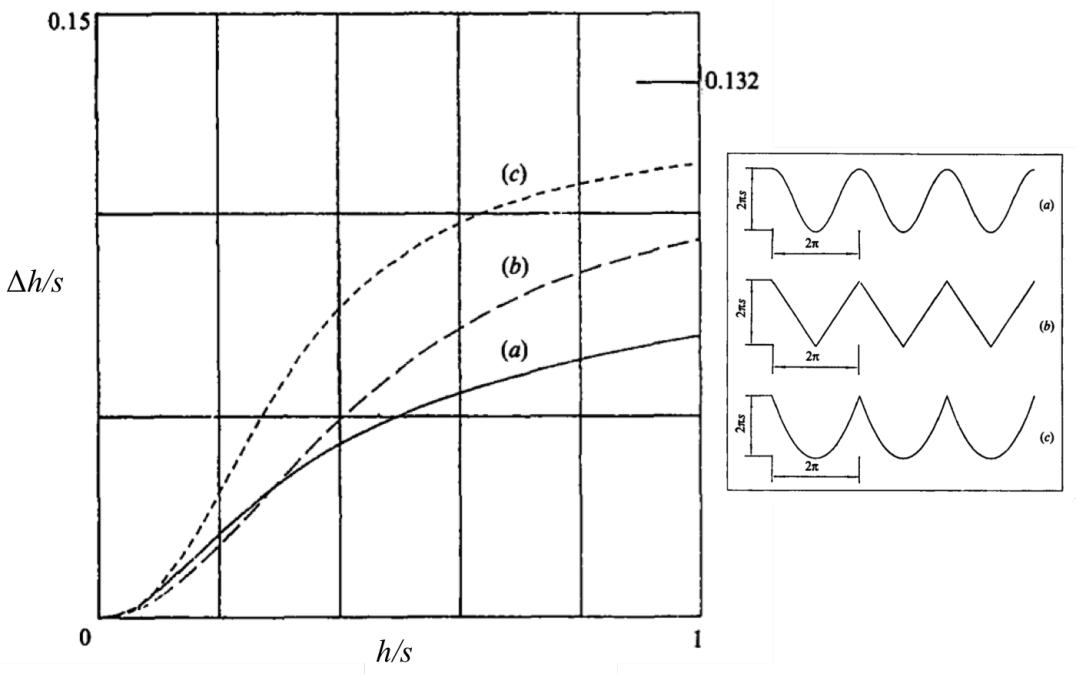

Figure 1.9: Protrusion height as a function of width to height ratio for three riblet geometries; a) cosinusoidal, b) v-groove, c) parabolic. Simulated data from Luchini et al. [3]

.

to an annual review by Jimenez [32] for more detailed information regarding Equation 1.5.

$$U^+(y) = \kappa^{-1} log(y/k_s) + 8.5 + \Pi\kappa^{-1} W(y/\delta) \tag{1.5}$$

Most of the data in present literature is from riblet geometries in the breakdown region. The reason is obvious: researchers desired to study the mechanisms of drag reduction for an optimal geometry. But the studies of Bechert et al. [2] and Walsh [27], although rich in viscous drag data, do not detail the flow inside the actual riblet where such information is crucial in understanding the mechanisms of drag reduction. Walsh [26] once did attempt to described the method of drag reduction when he used a hot-wire placed near the riblet surface. From the anemometry signal, he found that the peak streamwise velocity RMS value over the riblet surface was reduced when compared to a baseline flat plate. With this evidence, Walsh [26] theorized that riblets reduced drag by reducing the strength of

turbulent boundary layer bursts.

Walsh's [26] somewhat crude measurements were qualitatively correct. Literature suggests that riblets effectively shift the boundary layer upwards and reduce RMS values of the different components of velocity near the riblet surface, as was reported by Vukoslavcevic [33] and by Park et al. [34]. Each laboratory utilized hot-wire anemometry within the valleys of v-groove riblets. The riblets were of similar size, $h^+ = 17.5, s^+ = 35$. Vukoslavcevic [33] and by Park et al. [34] each confirmed that near the tip (peak) of the riblet, the mean shear was much higher than that found on a smooth plate. Near the valley, however, the mean shear was far lower. With respect to turbulence intensities, they found that near the peak, intensities were greater than when compared to a flat plate boundary layer. Similar to the mean streamwise profiles, near the valley the turbulence intensities were greatly diminished. The authors from each study concluded that the overall net drag reduction was due to a laminar-like region of flow in the valley of the riblet that exposed most of the wetted area to a low mean shear.

Suzuki et al. [35] provided additional insight into the flow in riblets via three-dimensional Particle Imaging Velocimetry (PIV). Suzuki examined trapezoidal riblets with two different characteristic dimensions: 1) $h^+ = 9.4, s^+ = 15$ and 2) $h^+ = 19.5, s^+ = 31$. The two cases highlighted drastic differences in flow data. This is to be expected since we know that the first riblet case should reduce drag and the second case should augment drag (see Figure 1.5). Their PIV results revealed two counter-rotating streamwise vortices that were located near the peaks of the v-groove riblets, for both cases. The major difference between the two cases was that in the drag decreasing case, the vortices had a vorticity magnitude that was much weaker than vortices from the drag increasing case. Furthermore, the drag increasing riblets induced vortices that were located (i.e., the cores of the vortices) closer to the surface of the riblet peaks than the drag reducing riblets. Such vortices and their differing strengths were echoed in computational studies performed by Choi et al. [13] when they studied four riblet v-groove geometries: two drag reducing and two drag augmenting. The only discrepancy between the counter-rotating vortices of Choi et al. [13] and Suzuki [35] was that the positions of the vortices were insensitive to changes in geometry. The computational results of Choi et al. [13] showed a reduction in peak spanwise and wall-normal turbulence intensities on the riblet surface compared to a flat

plate simulation. Similar results and discussions have come from Chu & Karniadakis [36] and Goldstein et al. [37]. Chu & Karniadakis [36] reported that the spanwise motion of low-speed streaks near the boundary layer was inhibited. They hypothesized the inhibition of these vortices caused reduced effectiveness in sweep and ejection events that cause shear. Sweep and ejection events are used to describe the effects of hairpin vortices that transfer momentum in turbulent boundary layers (Robinson [38] and Smith et al. [39]).

Djenidi & Antonia [40] took detailed flow measurements inside drag reducing and drag increasing riblets via laser Doppler anemometry. Results were similar to the findings of Choi [41]. For drag reducing riblets, the primary Reynolds shear stresses were slightly lower than those of a flat plate, and for drag increasing riblets the same terms were greater. They concluded that drag reduction occurs because streamwise vortices near the riblet surface are weaker than those on a flat plate, and in turn, they are less efficient at transporting high momentum fluid near the wetted surface area.

Lee & Lee [4] have provided the best experimental visualizations to date. Using PIV and smoke, the researchers documented streamwise vortices near two scalloped riblets. The first riblet had a drag reducing geometry, with $h^+ = 12.5, s^+ = 25$. The second had a drag increasing geometry, with $h^+ = 20, s^+ = 40$. Their results were clear in showing that the coherent structures in the boundary layer were displaced upward for the drag reducing case. Sometimes, these streamwise vortices would induce a weaker pair of vortices just above the riblet peak. It is notable that although riblet geometries differ greatly, streamwise vortices are identifiable in every case. Figure 1.10 shows the scalloped riblets with dots that mark peak values of streamwise vorticity over time. These dots essentially represent the cores of these vortices. As mentioned, the drag reducing riblets have moved the vortices away from most of the riblet surface area towards the riblet tip. The drag increasing geometry however, is large enough to allow those structures inside the riblet cross-sectional area, thereby permitting turbulence to transport high momentum fluid from above into the riblet valley.

1.1.3 Riblet Performance in Pressure Gradients

Most riblet research to date has been done in fully developed, turbulent channel flows. While this is an effective method to study fundamental flow physics near riblets, many

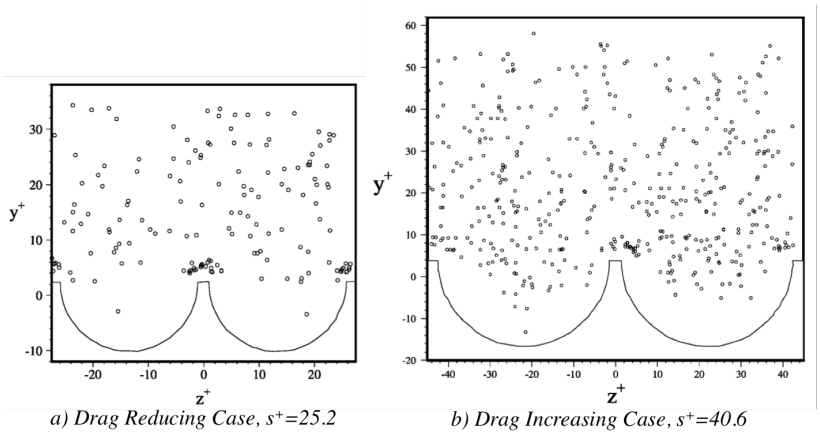

Figure 1.10: Experimental PIV data from two different scalloped riblets: a) drag reducing riblets & b) drag increasing riblets. Dots represent locations of peak vorticity over 100 image frames. From Lee & Lee [4].

practical implementations will expose riblets to varying pressure gradients specifically, Adverse Pressure Gradients (APG). An experiment focusing on the application of riblets to a practical engineering problem was carried out by Szodruch [42]. He reported that riblets attained about a 2% drag reduction when mounted on certain areas of on an Airbus A 320. More recently, Chamorro et al. [43] measured drag reduction on a section of a wind turbine blade. The authors reported a drag reduction of 4-6% with riblets. Importantly, they determined that partially covering the airfoil with riblets actually resulted in more drag reduction than completely covering the airfoil. Sareen et al. [44] also studied riblets mounted on a wind turbine blade, reporting a 5% drag reduction. A common feature among these three studies is that drag reduction is highly dependent upon riblet configuration (i.e., where riblets were mounted on the swept surface), which underscores the need for more fundamental research concerning riblets and APG's. Unfortunately, the few available fundamental studies disagree on how riblets perform with respect to the strength of the APG. The Clauser parameter, β quantifies the APG strength and is defined as:

$$\beta = \frac{\delta^*}{\tau_0}\frac{dp}{dz}$$

where δ^* is the displacement thickness and dp/dz is the streamwise pressure gradient.

Walsh [23] presents a brief summary of riblets in pressure gradients. Specifically, we summarize the past works of Choi [45], Truong & Pulvin [46], and Squires & Savill [47]. Choi [45] tested trapezoidal riblets in a strong APG with $\beta = 5.1$. He was unable to directly measure drag, and instead used a hotwire and skin-friction hot-film sensors to measure turbulent statistics. He reported no appreciable difference in these measurements and conjectured that turbulent skin-friction (as opposed to viscous skin-friction) did not change with pressure gradient. Truong & Pulvin [46] tested riblets mounted to a diffuser and found that as β increased, riblet drag reduction deteriorated, i.e., the riblets were not as effective. Lastly, Squires & Savill [47] tested riblets in two mild APG conditions, $\beta = 0.2$ and $\beta = 0.5$. At $\beta = 0.5$, the drag reducing benefit of riblets was eliminated.

However, Nieuwstadt et al. [5] noted that none of the prior studies measured drag directly, but instead used the momentum integral balance. As described by Nieuwstadt et al. [5], the momentum balance method suffers from a great dependence upon the measured momentum thickness, θ, at upstream and downstream locations–specifically the difference of those, $\Delta\theta$. In their study, just a 2% error in momentum thickness measurement produced a 25% error in $\Delta\theta$. Using a drag balance, Nieuwstadt et al. [5] tested trapezoidal riblets in moderate to strong APG ($\beta > 1$) and showed that riblet effectiveness *increases* with increasing β (just the opposite found by Truong & Pulvin [46] and Squires & Savill [47]). Debisschop & Nieuwstadt [6] used a drag balance to test trapezoidal riblets in a wind tunnel at $\beta = 2.2$, and found that riblet drag reduction had increased from 5% in a Zero Pressure Gradient (ZPG) to 13% in an APG, as shown in Figure 1.11.

As far as computational studies, the only publication to date is that by Klumpp et al. [48]. The authors used Large Eddy Simulations (LES) of turbulent flow around scalloped riblets to claim that even at mild APG ($\beta \approx 0.25$), riblet drag reduction can *double* that seen in a ZPG (drag reduction increased from 4.5% to 9%). Although the authors argued that their computational results mimic the experimental results by Nieuwstadt et al. [5], there are important differences between the simulations and experiments that need to be pointed out. The main difference is that at the same Clauser parameter as that used in the simulations, $\beta = 0.25$, the experimental results from Nieuwstadt et al. [5] showed no increase in drag reduction, while Klumpp et al. [48] reported an increase in drag reduction from 4.5% to 9%. Only at much higher values of β did the experimental results report a

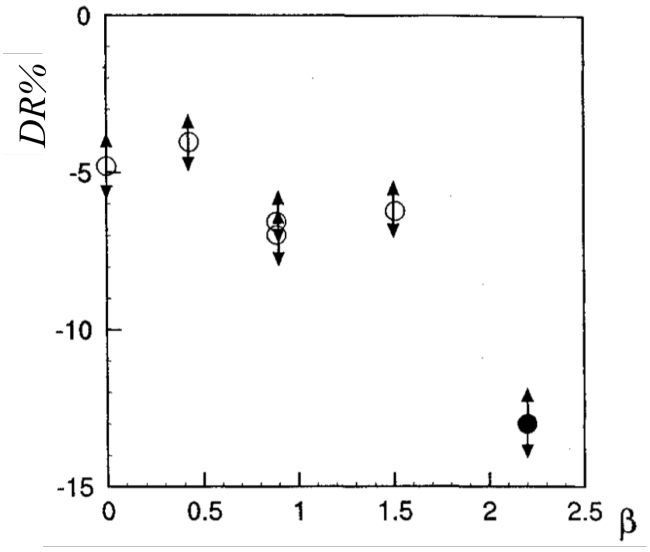

Figure 1.11: Experimental measurements of riblet drag reduction as a function of Clauser parameter. Open symbols fromNieuwstadt et al. [5], closed from Debisschop & Nieuwstadt [6].

significant increase in drag reduction. The reason for the discrepancy between Nieuwstadt et al. [5] and Klumpp et al. [48] is unknown, but one possibility could be that each study tested riblets that had different values of s^+.

It follows from the above literature that the performance of riblets in APG is still a subject of considerable debate, especially with regard to mild APG. Figure 1.12 shows how the Clauser parameter varies according to the angle of attack, α, for a NACA0012 airfoil (from Viswanath [7]). This figure shows that for a typical airfoil at an angle of attack of 4^o, $\beta \approx 0.5$, which corresponds to a mild APG. Therefore, according to the findings of Klumpp et al. [48], riblets could yield significant drag reducing benefits in many flows of engineering practice. This would be especially promising in terms of flow control since riblets are a passive means of drag reduction.

1.2 Sharkskin Drag Reduction.

This section details sharkskin denticles–their shapes, sizes, and flow conditions. The following sections also detail past research concerning denticles and attempts to apply their

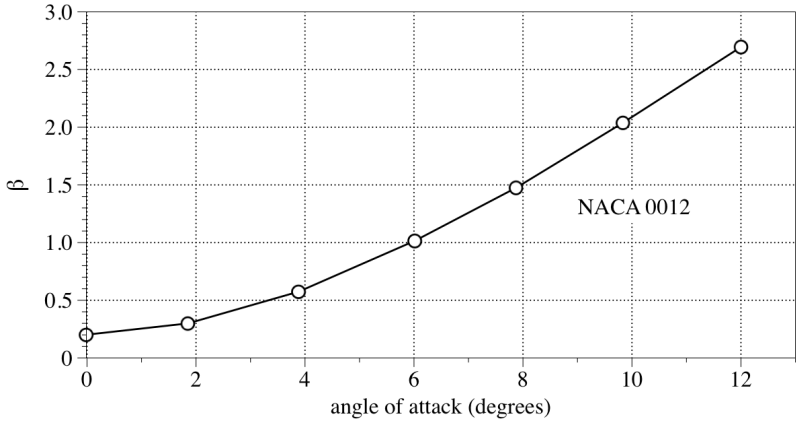

Figure 1.12: Variation of Clauser parameter, β, with angle of attack. β is the average value from $0.4 \leq z/chord \leq 0.95$ along a NACA 0012 airfoil. From Viswanath [7].

shapes to passive drag reduction techniques.

1.2.1 Sharkskin Background and Geometry.

Sharkskin is comprised of small tooth-like structures called denticles, or placoid scales which are affixed to a flexible epidermis/membrane. Fluid dynamicists and biologists have been attempting to elucidate the function of denticles over the past 30 years. In 1986, Raschi & Musick [8] took sharkskin samples from 15 species and measured denticles from different shark-body regions. A denticle taken from *Carcharhinus leucas* is seen in Figure 1.13. The primary keel (i.e., ridge) is labeled, and this particular denticle has secondary and tertiary keels. Sharkskin denticles are aligned parallel to the longitudinal axis of the shark and are directly exposed to water.

Raschi & Musick [8] theorized that denticles might behave similarly to riblets because denticles have a cross-sectional shape similar to scalloped riblets. Furthermore, when denticles overlap each other, this cross-section is preserved in the streamwise direction, further resembling riblets. Figure 1.14 shows a top view of sharkskin from a Bonnethead shark. Although the riblets and sharkskin look alike, the true test of whether they *act alike* is whether or not sharkskin can inhibit turbulent mixing, which is critical in reducing drag.

As mentioned, in Section 1.1.1 the best predictor of whether or not sharkskin can reduce

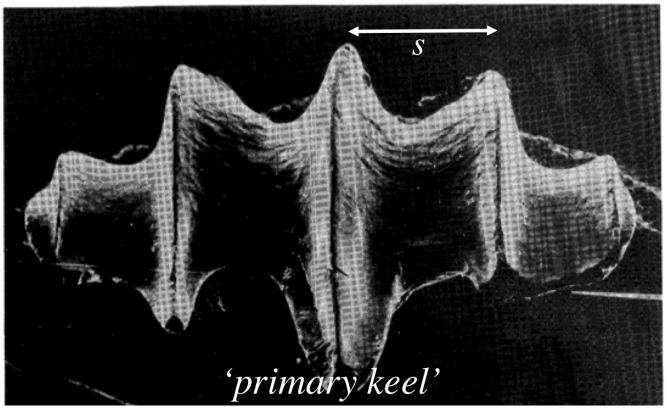

Figure 1.13: Denticle from *Carcharhinus leucas*. Width between keels, s, with the primary keel being centered. Taken from Raschi & Musick [8].

skin-friction is the width between keels in wall units, or s^+. The width between denticle keels was easily measured by Raschi & Musick [8], but the value of $w_{\tau,0}$ was unknown. These authors approximated this value using canonical flat-plate turbulent boundary layer relations–an approximation that does not incorporate any pressure gradient or roughness effects. In any case, the approximation led Raschi & Musick [8] to conclude that at voluntary swimming speeds ($\approx 55cm/s$), the denticle spacing was only $s^+ \approx 1.5$. This s^+ value is much lower than the optimal value for scalloped riblets– $s^+ \approx 16$ (see Bechert et al.[2]), so denticles at voluntary speeds would be suspected to be of little consequence. However, at burst swimming speeds ($\approx 1000cm/s$), the authors calculate that for fast-swimming (e.g., *Isurus oxyrinchus*) species of shark, $s^+ \approx 13 - 15$, which supports the theory that sharkskin is meant to passively reduce drag.

With the aforementioned commonalities aside, there are three crucial differences between denticles and riblets. The first is that the shape of denticles is highly three-dimensional while riblets are two-dimensional. Second, riblets retain a constant cross-sectional area in the streamwise direction, which is definitely not always the case with sharkskin. In fact, the degree to which denticles overlap has not been quantified. It is a function of species and the location on the animal's body. Figure 1.14 shows a bed of denticles that are not tightly packed, but other species (see Bechert et al. [16]) do have denticles that interlock with each other more. Third, each denticle has the ability to bristle

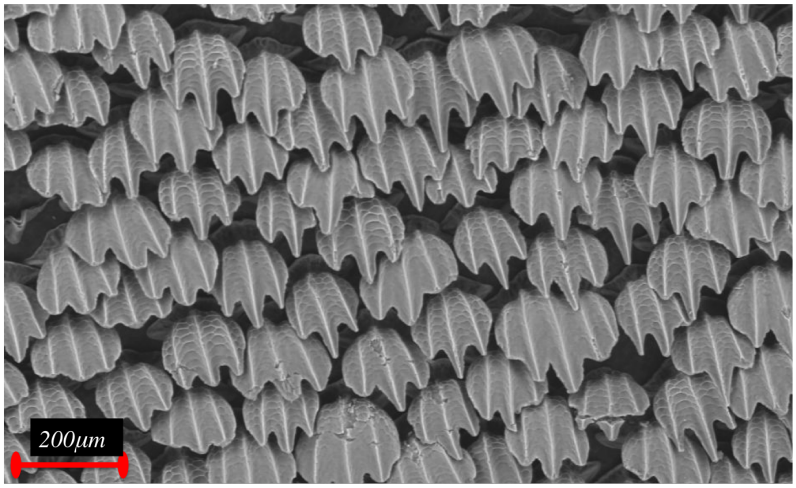

Figure 1.14: Top view of sharkskin from *Sphyrna tiburo*. Image from Lauder Laboratory of Harvard.

(see Lang et al. [49]), or tilt away/towards the epidermis at some Angle of Incidence (AOI). Denticle bristling adds a three-dimensionality that riblets would never introduce.

1.2.2 Denticles as a Method of Viscous Drag Control.

Currently, there is no agreement in the literature as to whether sharkskin is hydrodynamically beneficial to the species (see the review by Dean & Bhushan [50]). Reif et al. [16] created a mold from actual sharkskin and tested it in an air channel. With this apparatus, the authors were able to examine skin-friction at many values of denticle s^+. At two values of AOI (5° and 10°), they found that denticles *increased* drag. It should be noted though that the mold was not a replica because it did not contain cavities under the denticles. In 2000, Bechert et al. [51] created more realistic denticle models and tested them in an oil channel. When the denticles were perfectly interlocked, drag reduction occurred, but again, at an AOI, the sharkskin increased skin-friction drag. A conclusion from both of these experiments is that the *three-dimensionality of the denticles is detrimental to drag reduction.* Interestingly, Bechert et al. [9] reported that each denticle was attached to a spring and a level arm that controlled bristling. The purpose of the springs were to emulate the restoring force provided by muscle tension on actual sharkskin. The plastic denticles

could either experience a 'soft' or 'hard' spring. The author didn't provide any quantitative data as to what extent these two spring conditions went to keeping the denticles in place, so for now one must assume that a 'hard' spring means that the denticles were near rigid and 'soft' spring means that the denticles could flex somewhat in response to turbulent flow. Figure 1.15 shows the denticles affixed to a spring. Bechert et al. [9] tested three different configurations, as shown in Figure 1.16. The first was with the denticles bristled (AOI is unknown) with a hard spring. Very similar results to what was shown in Reif et al. [16]. Again we see that rigid denticles at some AOI increase viscous drag. The second conditions were with the soft spring. Here, we find that denticles increase drag, but less so than when rigid. Third, when gaps between denticles are sealed and at an AOI of zero, typical riblet behavior is exhibited.

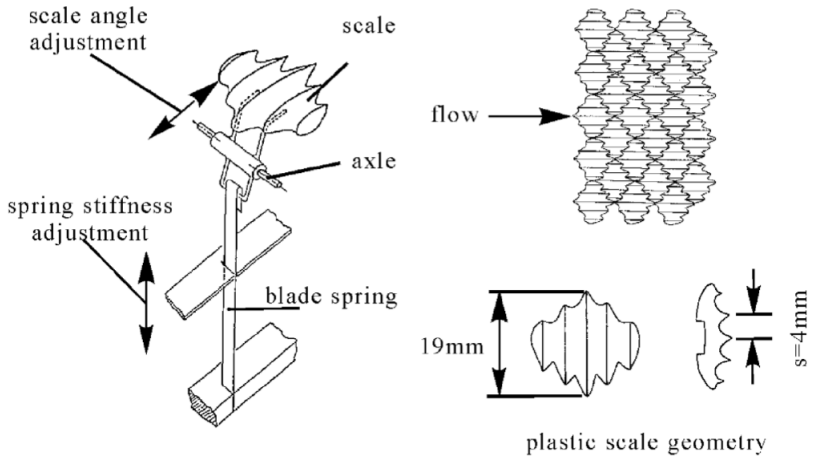

Figure 1.15: Plastic scaled denticles and their restoration force springs. From Bechert et al. [9].

There is however some experimental evidence that sharkskin can reduce drag. Jung & Bhushan [52] created milled denticles (*Squalus acanthias*) and tested them in a micro-channel (hydraulic diameter of $1mm$). They found a 30% reduction in pressure drop compared to a smooth surface. Oeffner & Lauder[53] tested actual sharkskin from *Isurus oxyrinchus* and *Lamna nasus* in a water channel. In this work, the skins were mounted on a flat plate that was heaved and pitched to propel the plate upstream at some self swimming speed (SSP). Oeffner & Lauder[53] found that sharkskin mounted on rigid plates decreased

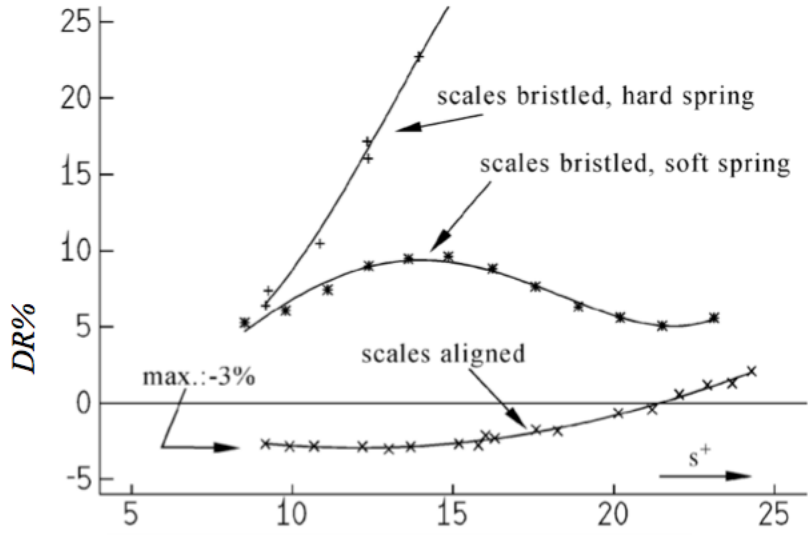

Figure 1.16: Experimental measurements of drag reduction by artificial denticles at three different conditions: bristled with hard spring, bristled with soft spring, and fully interlocking (aligned). From Bechert et al. [9].

the SSP of the test section (suggesting an increase in drag). However, when the same sharkskin was mounted on a flexible plate, an increase in SSP of $\approx$ 12% occurred on average [53].

Wen & Lauder [10] used a three-dimensional printer to create detailed denticles (*Isurus oxyrinchus*) on a substrate. When immersed in a water channel, these authors found that the denticles behaved similarly to riblets, with a maximum drag reduction of about 9% [10], as shown in Figure 1.17.

. This figure 1.17 shows a behavior similar to engineered riblets, though there is an important difference–there is no viscous region. That is, as the keel width trends to zero, it does not approach the flat plate solution.

1.2.3 Denticles as a Method of Separation Control.

Although limited (and conflicting) research contends that denticles cannot reduce viscous drag there is another potential hydrodynamic benefit. Reif et al. [16] first proposed the idea that due to the fact that denticles could bristle (have an AOI), and conjectured that

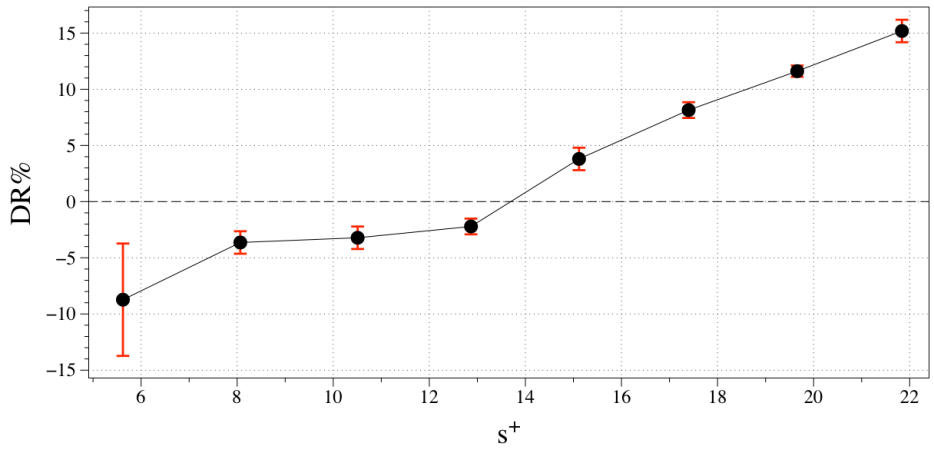

Figure 1.17: Experimental measurements of drag reduction as a function of denticle width. Denticles are 3D printed from an actual *Isurus oxyrinchus* denticle. From Wen & Lauder [10].

denticles could act as vortex generators to prevent separation. Specifically, a denticle somewhat resembles a Sub-Boundary layer Vortex Generator (SBVG) called a forward wedge (also known as a micro ramp). Vortex generators are any structure that creates secondary flow. This secondary flow typically manifests itself as counter-rotating streamwise vortices. These vortices are known to increase the momentum near their mounted surface via turbulent mixing. In turn, the mixing delays separation in adverse pressure gradients, and thus reduces form drag. SBVG's are vortex generators that have a device height to boundary layer height ratio of $h/d \approx 0.5$. The boundary layer height on a Mako shark is unknown, but if one assumes that the keel width is truly about 16 wall units, then from the denticle geometry provided by Wen & Lauder [10], the total denticle height is about 35 wall units. At only 35 wall units, one can say that a denticle would classify as a SBVG. Ashill et al. [11] published studies on a forward wedge (among other types of SBVG's) and produced Figure 1.18. In this plot, the induced streamwise vortices have a mean streamwise vorticity as plotted on the vertical axis as a function of device height (for the forward wedge, $h_e = h$). Note that most vortex generators on the order of 1,000 wall units, but even at very low values of h^+, vorticity is still produced.

There has been very little research on whether sharkskin acts similarly to SBVG's.

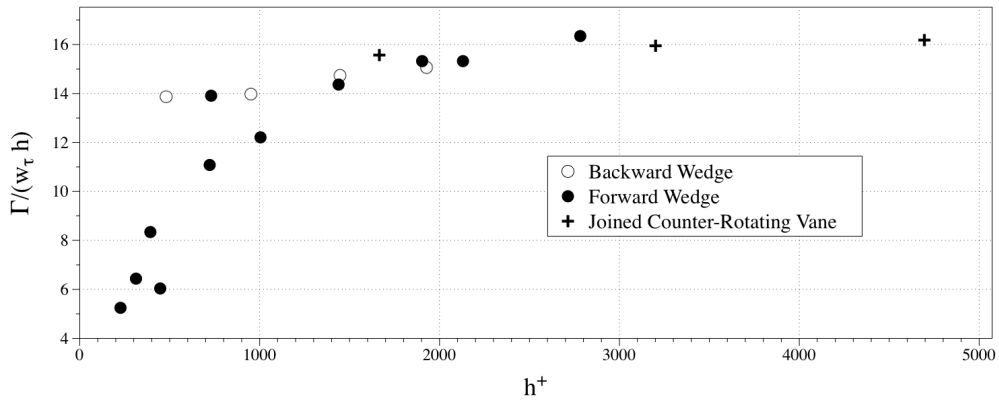

Figure 1.18: Normalized mean streamwise vorticity, Γ as a function of effective device height, h. Experimental data from Ashill et al. [11].

Lang & Hidalgo [54] 3-D printed denticles in a staggered array at an AOI of 90°. The denticles were placed in a water channel that induced only laminar flow. Using PIV, the authors reported that the denticles produced steady state vorticity within the array of denticles. When compared to the vorticity created by simple flaps (at the same height and 90°), Lang & Hidalgo [54] found that the denticles produced a vorticity that was, on average, stronger. The author hypothesizes that denticles are uniquely suited to preventing separation. Mendelsen et al. [55] studied similar bristled denticles using PIV and noticed two points of interests: 1) bristled denticles at 90° increase Reynolds shear stress values near the denticles more than stress values on a flat plate and 2) the existence of a 'development length' along the denticle array that is required to develop the increase in Reynolds shear stresses. Lastly, Lang et al. [49] reported that sharkskin helped to reduce boundary layer separation by mounting actual sharkskin on an airfoil at varying angles of attack. The authors utilized PIV to measure mean flow fields at areas where separation without sharkskin had occurred. At an angle of attack of 18°, the Mako sharkskin had almost fully prevented separation. However, at lower angles of attack (8-12°) the denticles had a negative influence, as they actually promoted separation. Lang et al. [49] theorized that at the higher angles of attack, the denticles were able to bristle, which helped to control the boundary layer by promoting turbulent mixing.

Although current literature has been unable to conclusively say whether or not sharskin

is hydrodynamically beneficial, nearly all can agree that there are two other ways that sharkskin could possibly reduce skin friction: 1) keeping the skin clean from other organisms and debris (anti-fouling) and 2) mucus secreted by the skin could create a slip boundary condition on the epidermis.

1.3 Dissertation Objectives

In this section, we describe the research goals and objectives for this dissertation.

1.3.1 Riblets.

As detailed in Section 1.1.3, knowledge regarding riblet drag reduction in mild APG is particularly important for practical implementations of riblet films. Unfortunately, current fundamental computational and experimental studies disagree in quantifying drag reduction in APG. Furthermore, more practical studies (e.g., riblets on a wind turbine blade) can only provide total drag measurements, as opposed to detailed flow field measurements within individual riblets. Therefore, the first goal of this dissertation is to contribute systematic numerical simulation results seeking to further elucidate the drag reduction capability of scalloped riblets under a mild APG, by considering a broad range of s^+ and also comparing the riblet performance in APG and ZPG turbulent boundary layers. To that end, we carry out high-resolution LES to systematically investigate riblet performance under various conditions and elucidate the fundamental physical mechanisms that govern riblet performance under APG and ZPG.

1.3.2 Sharkskin Denticles.

Although several published works have each investigated the hydrodynamic benefits of sharkskin, as was described in Section 1.2, the current literature has not yet met a consensus. We argue that the existing experimental studies are conflicting and difficult to interpret because of three main reasons: 1) manufactured sharkskin may not accurately mimic real skin, 2) lack of consistency among the turbulent flows in which the sharkskin was exposed in each experiment, and 3) the lack of knowledge regarding the flow-field details in the vicinity of the denticles. Therefore, the second goal of this dissertation is to determine whether or not sharkskin denticles can passively reduce skin-friction similarly to riblets in a systematic approach. The third objective of our work is to elucidate the fundamental physical reason for either case, which will hopefully shed light in the discrepancies in the literature. We undertake a series of DNS for various denticle arrangements using an

immersed boundary method to simulate the complex geometry of sharkskin. We also undertake a DNS for scalloped riblets at similar flow conditions to enable direct comparisons between the riblet and denticle induced flow fields and drag reduction efficiency. While our work does incorporate simplifying assumptions, e.g. denticles are mounted on a rigid flat surface and their AOI is held fixed, our simulations are, to the best of our knowledge, the first to provide detailed insights into the flow fields in the vicinity of denticles and identify specific mechanisms that contribute to the overall drag.

Finally, our fourth objective is to, for the first time, simulate a patch of sharkskin upstream of a separation bubble in order to test the ability of denticles to inhibit separation, thereby reducing form drag. The canonical separation bubble provides us the opportunity to make direct comparisons of the separation bubble with and without upstream sharkskin. We again utilize high-resolution, three-dimensional, time-accurate LES with a spatially developing turbulent boundary layer with a prescribed APG in order to calculate flow fields near the denticles in order to examine their ability to promote turbulent mixing.

This disseration is organized as follows:

- Chapter 2 details the numerical methods utilized to solve the Navier-Stokes equations using DNS and LES methods.
- In Chapter 3 we present four validation cases for the numerical methods.
- Chapter 4 describes the framework for simulating riblets in mild APG and detail their characteristics.
- In Chapter 5 we describe the sharkskin simulations in turbulent channel flow and compare their flow fields with riblets.
- Chapter 6 presents our results from simulating a patch of staggered sharkskin just upstream of a steady separation bubble to investigate the boundary layer control capabilities of sharkskin.
- Lastly, in Chapter 7 we summarize, conclude, and comment on future research concerning riblets and sharkskin.

Chapter 2

Numerical Method

This chapter defines and describes the governing equations for the problems simulated in this dissertation. It also describes the numerical methods in which these equations are solved and their ability to do so using high performance computers. Finally, this chapter details the domain boundary conditions used to simulate developing turbulent boundary layers under various streamwise pressure gradients.

2.1 Governing Equations.

In this dissertation, riblets and sharkskin will be simulated in incompressible turbulent flows. Sharkskin, of course, has water as its working fluid and for riblets, the primary application of interest is wind turbine airfoils. For both of these flows, the assumption of an incompressible fluid is accurate. Therefore, in this work, the governing equations are the incompressible Navier-Stokes equations for the conservation of momentum and mass. The equations are three-dimensional in space and unsteady in time. They are defined in Equations 2.1 and 2.2.

$$\frac{\partial u_j}{\partial x_j} = 0 \tag{2.1}$$

$$\frac{\partial u_i}{\partial t} + u_j \frac{\partial u_i}{\partial x_j} = -\frac{1}{\rho}\frac{\partial p}{\partial x_i} + \nu \frac{\partial^2 u_i}{\partial x_j \partial x_j} + \frac{1}{\rho} f_i \tag{2.2}$$

Here, the equations have been written in Einstein notation (summation occurs over repeated indices $i, j = 1, 2, 3$), where u_i is the velocity vector, ρ is the fluid density, p is the static pressure, and ν is the kinematic viscosity. The f_i represents external body forces (surface tension and gravity), but in this dissertation, f_i is set to zero.

2.1.1 Curvilinear Coordinates.

The Navier-Stokes equations have been defined in reference to a Cartesian coordinate system of space. In practice, however, few domains are solely square or rectangle. In order to simulate complex boundaries with high resolution clustered grids, researchers either typically utilize an unstructured (with some type of polygon) meshing or a structured grid (each cell has only four edges) that conforms to the boundary. In this dissertation, a structured grid is utilized, which mandates that the Navier-Stokes equations be rewritten to accommodate the fact that the grid lines are not necessarily perpendicular to their basis vectors. Therefore, the conservation equations have been rewritten in generalized curvilinear coordinates as shown in Equations 2.3 and 2.4. See Appendix A for a complete derivation of the governing equations.

$$J\frac{\partial U^j}{\partial \xi_j} = 0 \tag{2.3}$$

$$\frac{1}{J}\frac{\partial U^i}{\partial t} + \frac{\xi^i_m}{J}\frac{\partial}{\partial \xi_j}(U^j u_m) = \frac{\xi^i_m}{J}\left(\frac{1}{\rho}\frac{\partial}{\partial \xi_j}(\mu\frac{g^{jk}}{J}\frac{\partial u_m}{\partial \xi_k}) - \frac{1}{\rho}\frac{\partial}{\partial \xi_j}(\frac{\xi^j_m p}{J}) - \frac{1}{\rho}\frac{\partial \tau_{mj}}{\partial \xi_j} + \frac{1}{\rho}f_i\right) \tag{2.4}$$

Here, the spatial basis coordinates are referenced to by the variable ξ_j, where $\xi_j = \xi_j(x_1, x_2, x_3)$. Differential operators include an additional term, ξ^i_j, or the transformation metrics. Its definition, $\xi^i_j = \partial \xi_i / \partial x_j$ is determined from the chain rule as shown in Equation 2.1.1.

$$\frac{\partial}{\partial x_j} = \frac{\partial \xi_i}{\partial x_j}\frac{\partial}{\partial \xi_i}$$

The transformation metric is the basic operator required in making the transformation from Cartesian to curvilinear coordinates. As a consequence of the transformation, new variables U^i, J, and g^{jk} are created. The contravariant flux (physically the flow rate

through a cell surface) is $U^i = (\xi^i_j/J)u_j$, where J is the Jocobian of the transformation metrics, $J = |\partial(\xi_1, \xi_2, \xi_3)/\partial(x_1, x_2, x_3)|$. Notably, the Jacobian physically represents the inverse of the local cell volume. Finally, the contravariant metric tensor is defined as $g^{ij} = \xi^i_m \xi^j_m$. It should be noted that the transformed Navier-Stokes equations are only partially transformed (see Appendix A for more detail). Due to its physical meaning, the contravariant fluxes, U^i are stored at the surface of each grid cell. The static pressure, p, and Cartesian velocities, u_m, are stored at the cell centers. As already mentioned, f_i is set to zero.

2.1.2 Turbulence Closure.

The Navier-Stokes equations are derived by assuming that a fluid's control volume is infinitesimally small (continuous) and are thus are in a differential form. However, when simulating flows with computational tools, the fluid domain is not continuous; the flow is temporally and spatially discretized. Obviously, one would like to make the spatial discretization so fine that every scale of turbulence (or *eddy*) could be resolved, but depending upon the Reynolds number of the flow and computational resources, this could be totally impractical. Direct Numerical Simulation (DNS) takes such an approach to simulating turbulence. When using DNS, Equations 2.1 and 2.2 are discretized in space and time and then solved on a very fine grid to obtain every eddy of interest. Specifically, the grid must resolve small scales of turbulence that are responsible for the dissipation of kinetic energy, otherwise the simulation will be unstable. DNS is utilized for turbulent flows that have relatively low Reynolds numbers because as the Reynolds number increases, the scales of turbulence broaden, and DNS becomes impractical due to increased grid resolution requirements. For higher Reynolds numbers, common practice is to utilize Large Eddy Simulations (LES). In LES, larger scales of turbulence are resolved (i.e., calculated) and smaller scales are modeled. The threshold of eddy size that is modeled is determined by a filter. The filtered incompressible Navier-Stokes equations are shown in Equations 2.5 and 2.6.

$$\frac{\partial \bar{u}_j}{\partial x_j} = 0 \tag{2.5}$$

$$\frac{\partial \bar{u}_i}{\partial t} + \bar{u}_j \frac{\partial \bar{u}_i}{\partial x_j} = -\frac{1}{\rho}\frac{\partial \bar{p}}{\partial x_i} + \nu \frac{\partial^2 \bar{u}_i}{\partial x_j \partial x_j} - \frac{\partial \tau_{ij}}{\partial x_j} \tag{2.6}$$

Here, $\overline{()}$ represents the filtered variable which is also known as the resolved variable; the equations are solved for this variable. After filtering the Navier-Stokes equations, there is an additional term, τ_{ij}, which is the Subgrid-Scale (SGS) stress tensor. Its definition, $\tau_{ij} = \overline{u_i u_j} - \bar{u}_i \bar{u}_j$ represents turbulence that is not resolved, but is rather residual turbulence. The introduction of τ_{ij} poses the problem of *closure* because $\overline{u_i u_j}$ is another unknown. To close Equation 2.6 this work employs the Smagorinsky model [56]. This model uses the concept of an eddy viscosity, ν_t as seen in Equation 2.7.

$$\tau_{ij} = -2\nu_t \bar{S}_{ij} + \frac{1}{3}\delta_{ij}\tau_{kk} \tag{2.7}$$

The eddy viscosity is not a physical viscosity, per se, but instead a numerical construct designed to transport fluid stress via diffusion. First, note that if ν_t is zero, Equation 2.6 reverts back to Equation 2.2. Second, notice that for the general case, τ_{kk} has a value, but for incompressible flows, it is zero (divergence free). The filtered strain rate tensor, $\bar{S}_{ij}$ is defined as

$$\bar{S}_{ij} = \frac{1}{2}\left(\frac{\partial \bar{u}_i}{\partial x_j} + \frac{\partial \bar{u}_j}{\partial x_i}\right)$$

As for the value of the coefficient, ν_t, it is calculated via Equation 2.8.

$$\nu_t = C_s \Delta^2 |\bar{S}| \tag{2.8}$$

where the magnitude of the strain rate tensor is $|\bar{S}| = \sqrt{2\bar{S}_{ij}\bar{S}_{ij}}$, C_s is the Smagorinsky constant, and Δ is the size of the grid filter. The size of the grid filter is determined by calculating

$$\Delta = J^{-1/3}$$

or the cube root of the local cell volume. Now, the Smagorinsky coefficient can take many values, depending upon the flow. In laminar flow, C_s should be zero, but in channel flows C_s=0.065, as reported by Moin and Kim [57] . Each simulated flow can have regions where values of C_s are very different, so in this dissertation, C_s is dynamically calculated so that spatially (and temporally), its value varies. The dynamic Smagorinsky model of Germano et al. [58] is utilized. Germano proposed that to estimate C_s locally, one can examine the

smallest of resolved scales to gain information about the actual C_s. This is accomplished by applying another filter (called the 'test filter') to Equations 2.5 and 2.6. As a result, the Leonard term, $L_{ij} = \widetilde{\bar{u}_i \bar{u}_j} - \tilde{\bar{u}}_i \tilde{\bar{u}}_j$ is produced and can be calculated directly from the resolved velocities. The $\widetilde{()}$ operation refers to test filtering which essentially gathers velocity information from the 26 nodes surrounding grid node i, j, k via spatial averaging. Using the test filtered velocity, C_s is calculated as follows:

$$C_s = \frac{L_{ij} M_{ik} G_{jk}}{M_{np} M_{nq} G_{pq}}, \tag{2.9}$$

$$M_{np} = 2\Delta^2 \widetilde{\bar{S}_{np}|\bar{S}|} - 2\widehat{\Delta}^2 \bar{S}_{np} \widetilde{|\bar{S}|} \tag{2.10}$$

L_{ij} was previously defined and G_{jk} is the covariant metric tensor (needed for curvilinear coordinate transformation, see Equation 2.1.1). In Equation 2.10, $\widehat{\Delta}$ is the test filter, which is two times the grid filter length scale. In terms of discretization, C_s is a scalar calculated at the center of the cell, and when used in Equation 2.8, the value of C_s at the cell surface is linearly interpolated from surrounding cell centers.

2.2 Numerical Solution Methods.

Equations 2.3 and 2.4 constitute a set of equations that are second-order non-linear partial differential equations. To numerically solve them, this dissertation utilizes a fractional step (projection) method originally proposed by Chorin [59]. The fractional step method is useful because it decouples the momentum equations from the continuity equation. This method was developed for curvilinear grids by Ge & Sotiropoulos [60]. The temporal discretization of the momentum equation is shown in Equation 2.11.

$$\frac{1}{J} \frac{2(U^* - U^n)}{\Delta t} = RHS(U^*, u^*) \tag{2.11}$$

The right hand side refers to all terms in Equation 2.4 except the transient and pressure gradient terms. As seen, the temporal term is discretized using a Crank-Nicholson scheme that is second order in time. Here, the superscript asterisk is used to denote an *intermediate* flux. The first step of this method is to solve for the predicted flux, U^*. The superscripts n denotes the current (known) time levels. Spatial derivative terms of the right hand side

are discretized on a three-point, second-order accurate, central difference stencil. Complete detail regarding the finite difference stencils can be found in Appendix B.

The intermediate flux is not divergence free since the continuity equation has not yet been utilized, which will guarantee incompressibility. To incorporate continuity, which is also the second step, is to solve the following Poisson equation:

$$-J\frac{\partial}{\partial\xi_i}\left(\frac{1}{\rho}\frac{\xi_k^i}{J}\frac{\partial}{\partial\xi_j}\left(\frac{\xi_k^j\phi}{J}\right)\right)=\frac{3}{2\Delta t}J\frac{\partial U_j^*}{\partial\xi_j} \tag{2.12}$$

Some fractional step methods will directly solve for pressure, but Ge & Sotiropoulos [60] developed a projection method that solves for $\phi = p^{n+1} - p^n$. It is the unknown and the required correction for U^*. The contravariant flux is corrected by rearranging for the current pressure, $p^{n+1} = p^n + \phi$, and then Equation 2.13 is solved for the current contravariant flux.

$$U_i^{n+1} = U_i^* - J\frac{2\Delta t}{3}\frac{1}{\rho}\frac{\xi_k^i}{J}\frac{\partial}{\partial\xi_j}\left(\frac{\xi_k^j\phi}{J}\right) \tag{2.13}$$

This fractional step method was originally implemented by Gilmanov & Sotiropoulos [61] on a hybrid staggered/non-staggered Cartesian grid. Ge & Sotiropoulos [60] modified the method for curvilinear coordinates.

2.2.1 Solution of the Momentum & Poisson Equations.

The three momentum equations are second order and nonlinear. If the equations were simply linear, when written as a system of equations in matrix-vector notation, together they would resemble the common problem of $Ax = b$, where A is a coefficient matrix to the unknowns vector, x, and vector b refers to the system knowns. Such a linearization is a common technique used in order to solve for x since iterative solvers are rooted in Newton's Method, which is inherently linear. In order to linearize the momentum equations, the set is approximated using the Taylor series expansion. To start, the momentum equations are represented as

$$F(U) = 0$$

where F denotes the set of momentum equations operating on the *intermediate* contravariant flux vector, U^* (note that we here drop the asterisk for the sake of convenience). This general function includes the spatial and temporal derivatives seen in Equation 2.4. Let us now define U^i, which is the known approximation to U^* at the i^{th} iteration so that using Taylor's series expansion one can expand the function about U^i

$$F(U^i + \delta U^i) = F(U^i) + \frac{\partial F(U^i)}{\partial U}\delta U^i + O(\delta^2)$$

where δU^i is an incremental change in U^i that occurs each iteration. We neglect the higher order terms and set the left hand side to zero so that Equation 2.14 can be written:

$$\frac{\partial F(U^i)}{\partial U}\delta U^i = A\delta U^i = -F(U^i) \tag{2.14}$$

where A is the Jacobian of the function, $F(U^i)$. Equation 2.14 is Newton's Method for the linear approximated solution to U^* and is solved numerically using the GMRES method by Saad & Schulz [62]. For additional details concerning the CURVIB momentum solver, the reader is referred to Kang & Sotiropoulos [63]. As shown in Equation 2.11, the momentum equations are solved implicitly, which is unconditionally stable and thus is not subject to the Courant-Freidrichs-Lewy (CFL) time step restriction.

Unlike the momentum equation, the Poisson equation (Equation 2.12) is already linear. In CURVIB, it is also solved using the GMRES method. However, there is an important distinction to be made. The Poisson equation is highly sensitive to grid quality (see Kang & Sotiropoulos [63]) in that, the larger the aspect ratio of the local grid, the greater the numerical stiffness (i.e., the rate of convergence) of the iterative method. Large aspect ratios are commonplace in turbulent flow simulations because in order to resolve high mean velocity gradients near boundaries, the wall-normal grid resolution must be very high. But in the streamwise or spanwise directions, the grid resolutions can be much lower. The reason numerical stiffness occurs is because the differences among Eigenvalues of the Jacobian (defined as coefficient matrix A in Equation 2.14 above) grow as the aspect ratio increases. Another way of stating this is to say that the condition number of the Jacobian increases. To alleviate numerical stiffness, CURVIB utilizes a preconditioner for the Jacobian. A preconditioner is a matrix that when multiplied to some matrix, say M, reduces the condition number (i.e., clusters the Eigenvalues) of M. The preconditioner employed is the

algebraic multigrid (AMG). Originally developed by Kang & Sotiropoulos [63], CURVIB utilizes Petsc library [64] to implement the GMRES solver and the BoomerAMG library [65] to solve the Poisson equation on massively parallel supercomputers.

2.3 The CURVIB Method.

There are, in general, two different approaches for discretizing complex geometries: those that conform (i.e., fit) to a boundary and those that do not. Boundary-fitted grids can either be structured or unstructured. Unstructured grids are commonly triangular in shape and often utilize finite volume algorithms. Structured grids are rectangular and use either finite volume or finite difference methods. For the scalloped riblets simulated in Chapter 4, we utilize a curvilinear, structured, boundary-fitted mesh. This type of mesh is ideal because it allows for high quality clustered grid nodes along the riblet surface in the wall-normal direction.

Although curvilinear-type computational grids provide for high quality meshing, some geometries are simply too complex for boundary-fitted computational grids–a sharkskin denticle being such a geometry. To handle the arbitrary geometric complexity of a channel with a bed of denticles we employ the Curvilinear Immersed Boundary (CURVIB) method of Ge and Sotiropoulos [60]. CURVIB has been successful in modeling cardiovascular flows [66], stream restoration structures [63], and hydrokinetic turbines. The basic idea of the method is illustrated in Figure 2.1. First, the surface of an arbitrarily complex boundary is discretized with a triangular, unstructured mesh. Then, it is immersed in a Cartesian background mesh. Each background mesh cell is then either identified as a node interior to the denticles (cells with an X), a fluid node (filled circles), or an immersed boundary (IB) node (open circles). When classifying cells, a bounding box is placed around each immersed boundary. Then, a ray is cast from each cell within the box outwards. If the ray intersects the triangular mesh an odd number of times, that cell is classified as either a structure or IB node. If even, that cell is outside the boundary. The ray-triangle intersection was implemented by Borazjani et al. [66].

The resulting denticle that *the flow will see* is shown in Figure 2.2. The denticle (whose geometry is fully described in Chapter 5) appears that it was built with blocks. The finer the background grid, the more accurate the denticle surface is approximated.

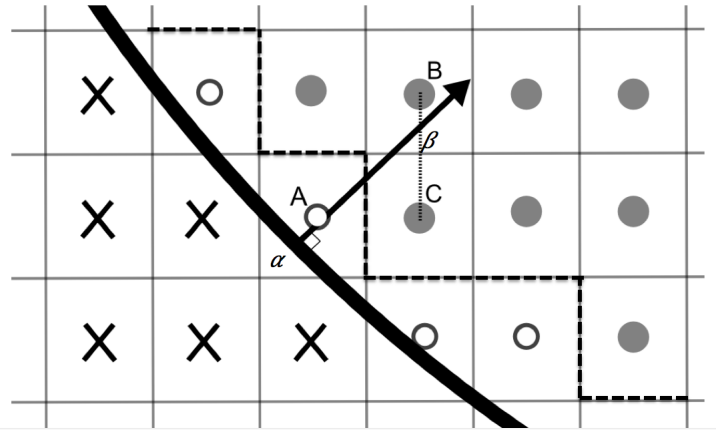

Figure 2.1: IB node classification and interpolation methods. Structure nodes (X), IB nodes (open circles), & fluid nodes (filled circles). Dashed line is the surface area where the viscous stress tensor is computed.

Boundary conditions for the velocity components are reconstructed at the IB nodes using interpolation along the normal to the body originating from the IB node (see Figure 2.1). Assuming the grid is fine enough so that the IB nodes are located within the viscous sublayer, linear interpolation can be used to reconstruct velocity boundary conditions. At the point marked α, in Figure 2.1, a normal vector connects with IB node A and a line (plane in 3D) between fluid nodes B and C, at some location β. Equation 2.15 is used to reconstruct the velocity boundary conditions at IB node A, where u_i^A is the i^{th} velocity component. Overlines denote distances between two points.

$$u_i^A = \left(\frac{\overline{A\alpha}}{\overline{\alpha B}}\right)(u_i^\beta - u_i^\alpha) + u_i^\alpha \tag{2.15}$$

An interpolation is used to obtain u_i^β and u_i^α is known *a priori* as a boundary condition. Again, this interpolation is accurate only when the background grid is sufficiently fine so that cells near the immersed boundary are in the viscous sub-layer. To calculate the drag force acting on the denticles we employ the method proposed by Borazjani & Sotiropopulos [66], namely integrating the pressure and viscous forces along the surface that approximates the IB interface as shown in Figure 2.1. We denote this as the denticle surface, Ω, and

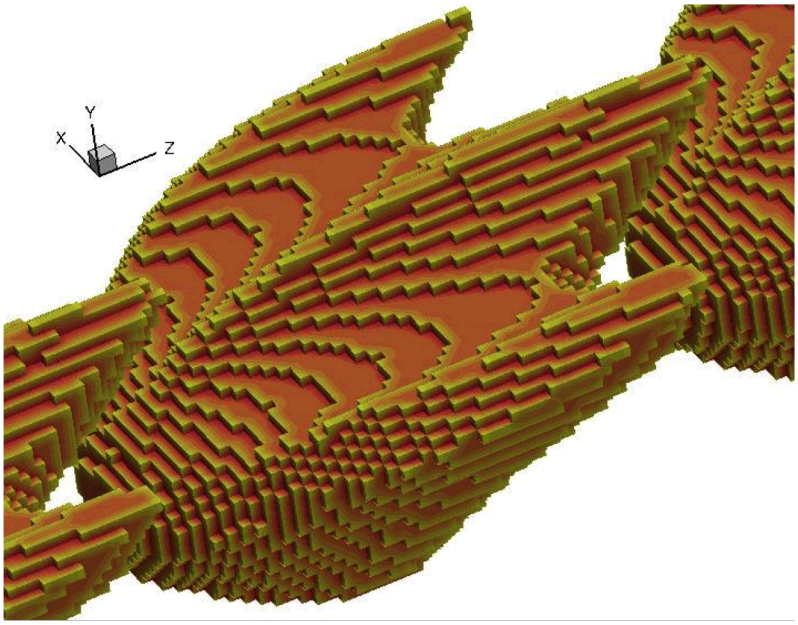

Figure 2.2: Denticle after grid node classification. Coloring used in this figure is for visualization only and does not represent any specific value.

compute the flow imparted force on the denticle surface as follows:

$$F_i = \int_\Omega -pn_i \mathrm{d}\Omega + \int_\Omega \tau_{ij} n_j \mathrm{d}\Omega \tag{2.16}$$

Here, n_i is the normal vector to a triangular element of the immersed body and τ_{ij} is the viscous stress tensor. The velocity derivatives required to calculate the components of the stress tensor are calculated using first order accurate differencing, which is accurate assuming that the IB nodes are all located within the laminar sublayer. To visualize the mean shear stress on an immersed body, we project τ_{ij} at the IB nodes onto the unstructured mesh of the immersed body by averaging the stress tensor from the nearest IB nodes.

Finally, it is obvious that the denticles are not symmetric in the streamwise direction. However, they will be immersed in a periodic simulation requiring that node classification be the same at the inlet and the outlet. To remedy this problem, the simplest solution was to modify the denticles at the inlet and outlet by extruding the denticle a very small distance at a prescribed streamwise location. The extrusion had a constant cross-sectional

area so that each denticle thus had a small symmetric portion at the inlet and outlet. This modification will in no way adversely affect the turbulent flow because the simulation is periodic in the streamwise direction.

2.4 Spatially Developing Turbulence.

When simulating any type of turbulent flow, the inflow boundary condition is of great importance. To acquire an authentic turbulent inflow, one obvious solution is to simulate transition from laminar to turbulence. This however will require a large domain, both in physical size and cell count. The physical size must be large enough to reach the critical Reynolds number and to allow development until a sufficient turbulent boundary layer height is achieved. Due to the computational expense of the this method, we therefore employ the rescaling method of Lund et al. [67]. When compared with other turbulent flow generation methods (e.g., parallel inflow method or synthetic turbulence method), the rescaling technique is superior at generating realistic scales of turbulence that do not dissipate prematurely.

The essential idea of the rescaling method is that, in a computational domain, a boundary layer at some downstream location (which is termed the *recycling plane*) can be scaled and re-fed into the same domain (a pseudo-periodic inlet boundary condition). The rescaling procedure prescribes the mean boundary layer height at the inlet and subsequent growth will occur naturally, thus creating a steady (in time) Spatially Developing Turbulent Boundary Layer (SDTBL). At its fundamental level, the method relies on the observation that turbulent boundary layers have two distinct regions: an inner layer and an outer layer. It also depends on the Reynolds decomposition of velocity,

$$u_i(x_i, t) = \overline{u_i}(x_i) + u'(x_i, t)$$

where the overline denotes time averaging and the prime denotes fluctuations. For upcoming discussions, we now define Cartesian velocities u, v, w that correspond with directions x, y, z, respectively and that w signifies the streamwise, v, wall-normal, and u, spanwise directions. In the inner layer, velocities are rescaled according to the linear portion of the law of the wall in the wall-normal direction:

$$\frac{\overline{w}^{inner}}{w_\tau} = f_1(y^+)$$

where f_1 is some function to be determined, w_τ is the shear velocity, and $y^+ = yw_\tau/\nu$. In the outer layer, velocities are rescaled according to the defect law:

$$\frac{\overline{w}_\infty - \overline{w}^{outer}}{w_\tau} = f_2(\eta)$$

where $\overline{w}_\infty$ is the freestream velocity and $\eta = y/\delta$. The local boundary layer height is δ and f_2 is another general function. The rescaling method uses Equation 2.17 for the inner layer. Note that subscripts, *inlt* and *recy* denote whether the velocities are defined either at the inlet or recycle planes, respectively.

$$\overline{w}_{inlt}^{inner} = \gamma \overline{w}_{recy}(y^+_{inlt}) \tag{2.17}$$

Here, $\gamma = w_{\tau,inlt}/w_{\tau,recy}$, and in the mean should always be greater than one. Equation 2.18 determines the outer layer scaling.

$$\overline{w}_{inlt}^{outer} = \gamma \overline{w}_{recy}(\eta_{inlt}) + (1-\gamma)\overline{w}_\infty \tag{2.18}$$

For the wall-normal mean velocities, Lund et al. [67] assumes that they scale as:

$$\overline{v}_{inlt}^{inner} = \overline{v}_{recy}(y^+_{inlt})$$

and

$$\overline{v}_{inlt}^{outer} = \overline{v}_{recy}(\eta_{inlt})$$

Mean velocities in the spanwise direction are set to zero. The fluctuating velocities are scaled similarly:

$$(u_i')_{inlt}^{inner} = \gamma (u_i')_{recy}(y^+_{inlt})$$

and

$$(u_i')_{inlt}^{outer} = \gamma (u_i')_{recy}(\eta_{inlt})$$

In this dissertation, the rescaling method is applied to the LES filtered variables. Now, due to the fact that inner and outer regions of a boundary layer are not so distinct so as

to say that the positions of the inner and outer layers could be defined by some threshold y^+, a value for each mean and fluctuation velocity is blended between the two layers using a weighting function, $F(\eta)$, as seen in Equation 2.19.

$$(u_i)_{inlt} = \left[(\overline{u_i})_{inlt}^{inner} + (u_i')_{inlt}^{inner}\right][1 - F(\eta_{inlt})) + \left[(\overline{u_i})_{inlt}^{outer} + (u_i')_{inlt}^{outer}\right] F(\eta_{inlt}) \qquad (2.19)$$

The weighting function is defined as:

$$F(\eta) = \frac{1}{2}\left\{1 + tanh\left[\frac{\alpha(\eta - \beta)}{(1-2\beta)\eta + \beta}\right] / tanh(\alpha)\right\}$$

where $\alpha = 4$ and $\beta = 0.2$. When $\eta \geq 1$, $F = 1$.

Putting the rescaling method into practice, one should first note that the Reynolds decomposition requires a running mean velocity that is not fixed *a priori*. Therefore, the following weighted time-averaging scheme is utilized:

$$\overline{u}_i^{n+1} = \frac{\Delta t}{T}\left\langle u^{n+1}\right\rangle_x + \left(1 - \frac{\Delta t}{T}\right)\overline{u}_i^n$$

Here, $\langle\rangle_x$ denotes spanwise spatial averaging and T is some weighting constant. When first starting the SDTBL simulation, $T = 10\delta/\overline{w}_\infty$, as suggested by Lund et al. [67]. As the simulation matures and approaches steady state, $T \approx 100\delta/\overline{w}_\infty$. The value of T is very important, as it can drastically affect turbulent statistics.

There are several nuances to implementing the rescaling method, which are not necessarily mentioned by Lund et al. [67], that were used for the simulations in this dissertation. Each is valuable and is recorded here:

1. The grid-cell aspect ratio, $\Delta z/\Delta x$ should not be too large (approximately > 8) for the rescaling method with LES. The turbulence viscosity in LES is determined in part from this ratio, and if it is too high, ν_t will actually be lower than what is required to correctly model turbulence.

2. To use Equation 2.17, $\overline{w}_{recy}$ must be evaluated at y_{inlt}^+. Since y_{inlt}^+ and y_{recy}^+ are almost never the same, a linear interpolation at the recycling plane was used to determine an appropriate $\overline{w}_{recy}$.

3. The boundary layer at the inlet should be prescribed by the user. The momentum thickness, θ_{inlt} can also be fixed, if desired.

4. The mean shear velocity at the inlet, $w_{\tau,inlt}$, cannot be fixed *a priori* if δ_{inlt} is also fixed. Therefore, as suggested by Lund et al. [67], Equation 2.20 is used for the shear velocity at the inlet.

$$w_{\tau,inlt} = w_{\tau,recy}\left(\frac{\theta_{recy}}{\theta_{inlt}}\right)^{1/8} \tag{2.20}$$

5. Developing authentic turbulence with numerical methods can be difficult since artificial fluctuations easily die out. In this dissertation, the initial solution was Spalding's [68] turbulent boundary layer approximation, given some δ_{inlt}. This profile was superimposed with random fluctuations at 10% of $\overline{w}_\infty$. Keeping T low is crucial to maintain a mean turbulent profile early in the simulation. If the reader is interested, consulting the work of Liu & Pletcher [69] may be of help. Figure 2.3 is a plot of shear velocity at the recycle plane as a function of timestep. Note how the artificial turbulence from the initial solution quickly dissipates, but turbulence naturally occurs at timestep 10,000. At timestep 20,000, T was increased.

6. Velocities at the inlet that are at a height above δ_{inlt} were set as following:

$$\overline{w}_{inlt} = \overline{w}_\infty$$

$$\overline{v}_{inlt} = \overline{u}_{inlt} = 0$$

   Furthermore, all fluctuating velocities at these locations were set to zero. This is appropriate since freestream is usually free from secondary flow and turbulence. Values for $\overline{v}$ are just not known beforehand. Setting $\overline{v}_{inlt}$ to zero will alter the momentum and displacement thickness locally, but these will naturally readjust.

In conclusion, the rescaling method of Lund et al. [67] is a powerful method to create realistic turbulence. Given $\overline{w}_\infty$, δ_{inlt} and a viscosity, nearly any SDTBL can be simulated (given a fine enough grid).

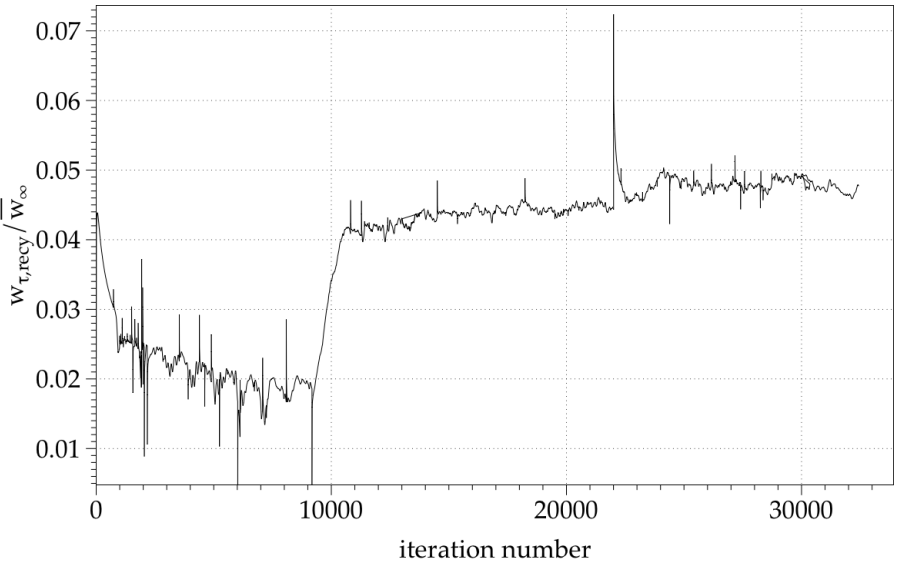

Figure 2.3: Shear velocity at the recycling plane as a function of timestep.

2.5 Boundary Conditions.

There are several different boundary conditions that are applied to the domains used in this dissertation. The first, and most common, is no-slip boundary condition which is a Dirichlet type condition. It is applied to Cartesian components:

$$u_i = 0$$

and also to the contravariant flux *normal* to the no-slip surface:

$$U\Big|_{wall} = 0$$

where $i = 1, 2, 3$. Because CURVIB defines Cartesian velocities at cell centers, $u_i = 0$ is implemented with the help of a ghost node. A ghost node is an extra cell that is added outside the domain. Therefore, the Cartesian velocities only have direct influence through the calculation of spatial derivatives near the wall. For this reason, the contravariant flux is set to zero. For this boundary condition to work as expected, the background grid resolution must be such that the inner part of the boundary layer is well resolved. Usually,

a $y^+ < 1$ for the first grid node off the wall is required. For DNS, it is common to have $y^+ < 0.5$.

The second boundary condition is the slip (or stress-free) boundary condition. This is a Neumann-type condition, where the wall-normal gradient of each Cartesian velocity is set to zero:

$$\partial u_i / \partial n = 0$$

where $\partial / \partial n$ denotes wall-normal gradients. The wall-normal contravariant flux is also zeroed:

$$U\Big|_{wall} = 0$$

This boundary condition is nearly the same boundary condition water flowing through an open-channel would receive at the water's surface. Due to the absence of a mean velocity gradient, no turbulence is produced and the restriction of a fine y^+ is removed.

The third boundary condition is the periodic condition. Unlike the previous two, this condition allows a wall-normal flux and creates, spatially, an infinite domain. To implement this condition, each component of velocity at some boundary is copied to its opposite boundary.

Fourth, is the convective boundary condition. This condition is used at the outlet of a domain:

$$\frac{\partial U^i}{\partial t} + c \frac{\partial U^i}{\partial n} = 0$$

and has the form of a wave equation. Here, $\partial / \partial n$ refers to a derivative in the direction normal to the outlet domain, and c is the integrated bulk velocity across the entire outlet domain. To help ensure convergence of the Poisson equation, a mass flux correction (i.e., the difference between inlet and outlet mass fluxes) is applied to each cell on the outlet. This difference is very small, typically less than 0.005%.

Fifth, is a boundary layer growth boundary condition. As a turbulent boundary layer develops, a small, yet physically significant, wall-normal velocity exists that contributes to the boundary layer growth rate and will actually affect the streamwise pressure gradient. The condition is defined in Equations 2.21 and 2.22. It originates from the integral

momentum and continuity equations as described by Lund et al. [67]:

$$\frac{\partial w}{\partial y} = \frac{\partial u}{\partial y} = 0 \tag{2.21}$$

and

$$v = W_e \frac{d\delta^*}{dz} + (\delta^* - L_y)\frac{\partial W_e}{dz} \tag{2.22}$$

where δ^* is the displacement thickness and L_y is the height of the domain in the wall-normal direction. This boundary condition is applied to the top of the domain where the freestream velocity, W_∞ is defined. In Equation 4.2, $W_e(z)$ is the external freestream velocity. When the boundary layer is in a Zero Pressure Gradient (ZPG), $W_e = W_\infty$, which would also mean that the second term on the right hand side of Equation 4.2 is zero. The contravariant flux through the top of the domain is $V = vA_n$, where A_n is the local cell surface area.

The last velocity boundary condition used in this dissertation is a fixed-flux condition:

$$\frac{\partial w}{\partial y} = \frac{\partial u}{\partial y} = 0$$

and

$$v = v(z)$$

where $v(z)$ is prescribed throughout the simulation and is known *a priori*. This condition will be used to create a separation bubble that's time-averaged shape is known.

2.6 Parallel Computing Capabilities.

Simulating roughness in turbulent flows is challenging due to the small sizes of the roughness elements. Drag-reducing riblets are smaller than 25 wall units in height and width and the sharkskin denticles are less than 35. Modeling such small yet geometrically complex roughness requires high spatial resolution. Additionally, minimum domain dimensions are required to reduce two-point correlations. The result is grid cell counts between 40 million and 183 million points, which are not exceptional, but do require massively parallel algorithms.

CURVIB is coded with the C language and utilizes PETSc libraries [64] for data structure logistics, matrix/vector operations, and momentum equation solves. The BoomerAMG library [65], which is linked within PETSc, is used to condition and solve the Poisson equation. CURVIB has been developed for distributed memory systems and uses openMPI for communication among supercomputer nodes and cores.

As problem sizes increase, it is appealing to utilize very large (tens-of-thousands of cores) compute-clusters. With these systems, application efficiency (especially on systems with hundreds-of-thousands of cores) is of great importance. To evaluate the efficiency and performance of CURVIB, we were granted access to Sandia National Lab's RedMesa cluster. RedMesa is currently rated 114^{th} on the world's fastest supercomputers. It has approximately 24,000 Intel X4470 (2.93Ghz) cores connected via Infiniband. Each node has eight cores with 12Gb of shared memory.

To evaluate the efficiency of CURVIB, two parameters were assessed: strong and weak scaling. They are defined in Equations 2.23 and 2.24, respectively:

$$S(n) = \frac{t_{min}}{t_n}\Big|_{fixed} \tag{2.23}$$

$$W(n) = \frac{t_{min}}{t_n}\Big|_{variable} \tag{2.24}$$

where t_{min} refers to the solution time with the minimum required cores to run the simulation and t_n refers to the solution time with n cores. The true definitions of strong and weak scaling do not use t_{min}. Instead they use t_{seq}, which refers to the solution time achieved with a single, sequential process. However, with such large problem sizes, it would likely be impossible to even achieve a solution with one process (due to lack of memory), so instead, we use t_{min}. Each function is evaluated using a different method. Strong scaling is computed with the problem size remaining fixed. Weak scaling is computed by using a variable problem size.

If the user of an application is focused on acquiring solutions *in less time* (i.e., simulation turnover), strong scaling is most important. To compute $S(n)$, the problem size (say, number of grid nodes) is held constant, while the number of cores, n, is increased. $S(n)$ is an evaluation of the application's ability to decrease computation time with increasing resources. Ideally, $S(n)$ scales linearly with n. If the user is focused on solving *larger* or

more problems, then weak scaling is most important. When computing $W(n)$, the problem size *per core* is held constant, while n is increased. This parameter is an evaluation of the application's ability to distribute work and communicate effectively. Ideally, $W(n) = 1$.

For the scaling tests, a turbulent open channel flow was simulated. The timestep was held constant among tests, as was Reynolds number, grid spacing, and bulk velocities. To increase problem sizes, the length of the domain width (spanwise direction) was increased. The grid was uniform in the streamwise and spanwise directions and clustered in the wall-normal direction to resolve the boundary layer. A fourth-order modified Runge-Kutta method was used to solve the momentum equations. Each case was a DNS and thus required no turbulence closure model. First, weak scaling results from RedMesa are shown in Figure 2.4.

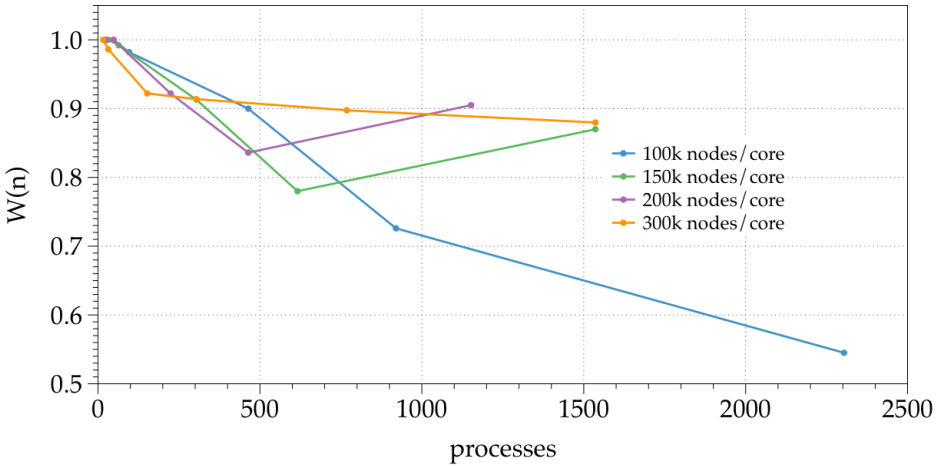

Figure 2.4: Weak scaling on RedMesa, 8 cores per node.

These scaling results are quite typical and show good weak scaling. As the number of grid cells per node increases, the scaling improves. This is due to less MPI communication among nodes. It should be noted that good weak scaling is easier to achieve than good strong scaling. Strong scaling results from RedMesa are shown in Figure 2.5.

The different colored lines in Figure 2.5 correspond to certain grid cell counts (in millions). From this figure, it i seen that at about a speedup of three, a plateu occurs. This translates to an efficiency, E of about 30-40%, where

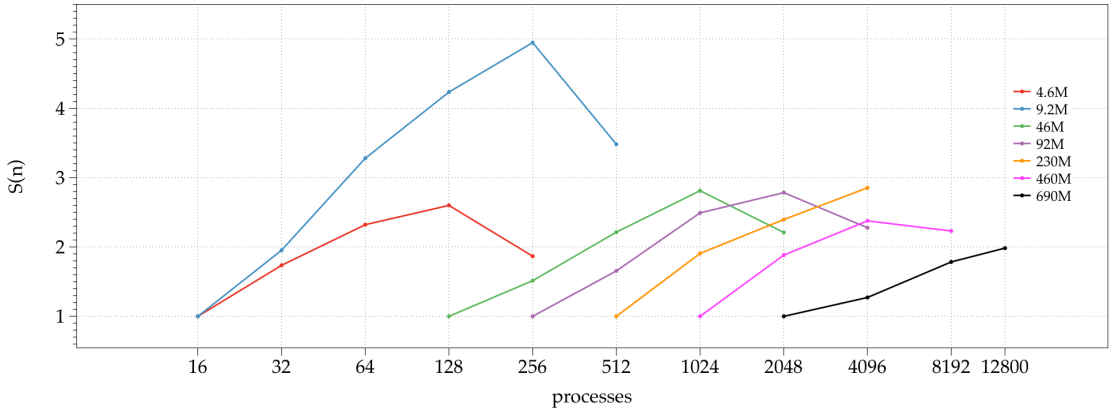

Figure 2.5: Strong scaling on RedMesa, 8 cores per node.

$$E = S/n_{ratio}$$

and $n_{ratio} = n_{max}/n_{min}$. This result is reasonable, but should be improved. To explore possible avenues for increasing E, strong scaling results were calculated by only using *half* of the cores available per node. Results are illustrated in Figure 2.6.

When running with only half the number of cores per node, there is a drastic difference in strong scaling. The reason for completing this test is to examine the effect of intra-node memory bandwidth. Strong scaling is much improved because the four cores now have double the memory bandwidth that eight running cores would have. This result conclusively reveals that CURVIB suffers from an intra-node memory bandwidth bottleneck. Unfortunately, this bottleneck is common and a challenge to address. One solution is to employ both MPI and openMP coding paradigms. For intra-node communication, openMP could be used and inter-node communication could be accomplished with MPI. This type of communication is the state-of-the-art in the field. Second, acceleration with a Graphics Processing Unit (GPU) could be of help. GPU's perform extremely well with embarrassingly parallel algorithms. Even though CURVIB is not so parallel, some sections likely are. Finally, it is important to note that the poor strong scaling results are also due to the Poisson equation. Testing different preconditioners can be of help, as shown in Figure 2.7.

Two different preconditioners are used for the strong scaling results in Figure 2.7:

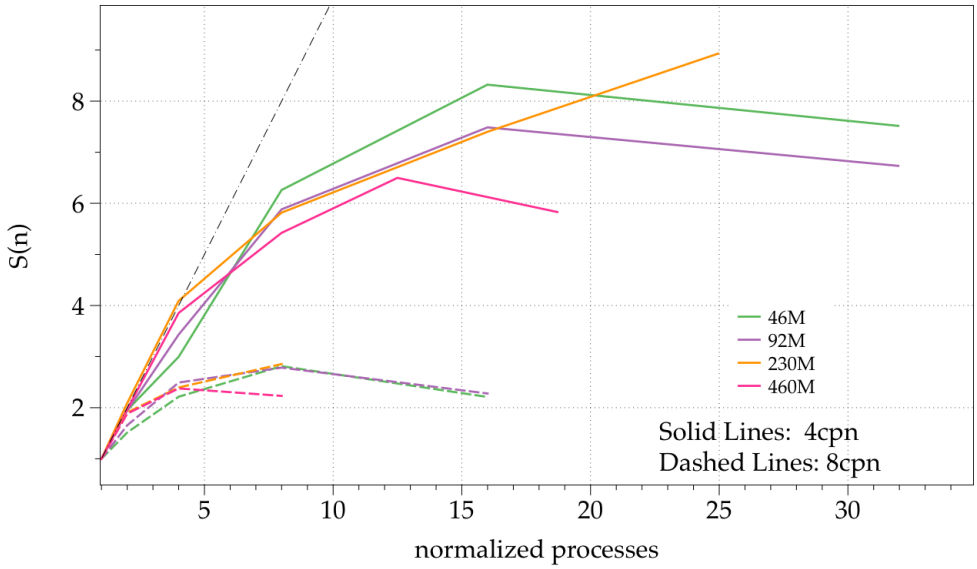

Figure 2.6: Strong scaling on RedMesa, 8 cores per node.

BoomerAMG method and PETSc's AMG method. When using the algebraic multi-grid written in native PETSc, the efficiency is improved to 40-50%. Finally, another possible solution is to move away from using the PETSc libraries. Although time consuming, fine-tuning of the matrix operations and solver could be possible.

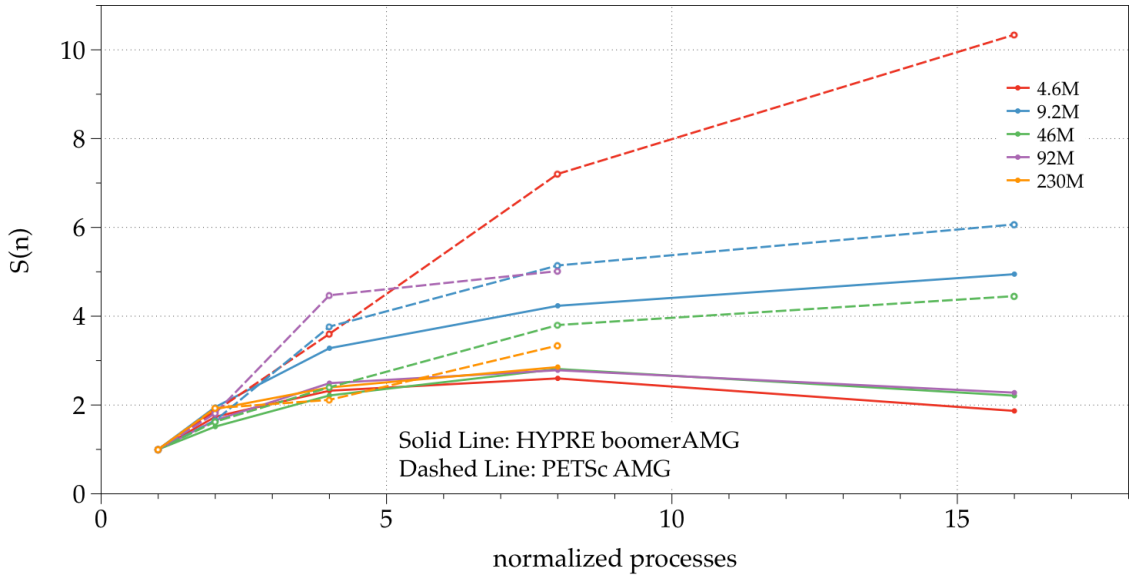

Figure 2.7: Strong scaling on RedMesa, 8 cores per node.

Chapter 3

Validation

This chapter presents validation cases for the DNS, SDTBL, and CURVIB numerical methods used in this dissertation. For each case, directions x, y, z correspond to Cartesian velocities, u, v, w where x is the spanwise, y the wall-normal, and z the streamwise directions.

3.0.1 Channel Flow Validation.

To validate our DNS numerical method, a canonical turbulent channel flow was simulated with $Re_\tau \approx 180$. The corresponding bulk flow Reynolds number is $Re = W_{bulk}\delta/\nu = 2800$. W_{bulk} is the integrated bulk streamwise velocity and δ is the domain height, as shown in Figure 3.1.

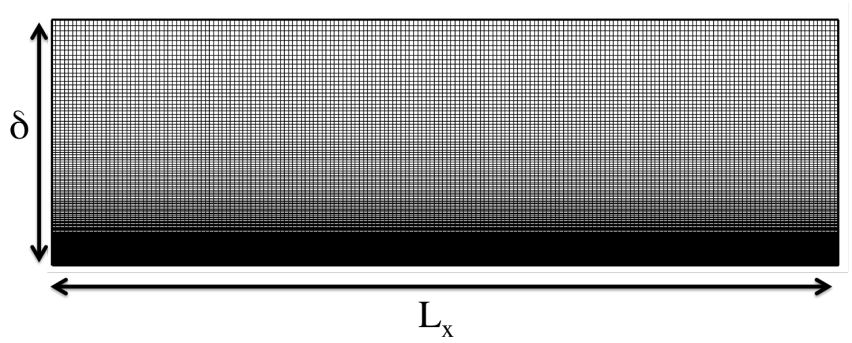

Figure 3.1: Front view of the computational grid for DNS validation case. The turbulent flow travels into the page.

Figure 3.1 also shows the wall-normal grid that is clustered using a constant stretching ratio of 1.05. The computational grid has a uniform spanwise and streamwise spacing. Details concerning the domain size and mesh counts can be found in Table 3.0.1. No grid independence study was undertaken since the grid spacings in each direction (Δy^+, Δx^+, and Δz^+) are known to be adequate (see Kim et al. [12]). The no-slip boundary condition is applied at the bottom of the domain and at the top, we employ a stress-free boundary condition. In the spanwise and streamwise directions, the flow is periodic. The simulation was run until the mean kinetic energy was statistically stationary and then the flow field was averaged for $150\delta/W_{bulk}$ (nondimensional time). The simulation's timestep was such that the maximum Courant-Freidrich-Lewey number, $CFL_{max} \approx 0.5$. It should be noted that low Reynolds number simulations can sometimes be *sticky*–i.e., the flow remains laminar if artificial perturbations are used to initialize the flow field. There are two solutions to initiate genuine turbulence: 1) early on in the simulation, one can decrease the viscosity temporarily and 2) with CURVIB, one can include several spanwise blockages to help trip the flow. We used both of these solutions in this validation case to initiate self-sustaining turbulent flow.

Table 3.1: Computational grid details for the DNS validation case. N_x, N_y, and N_z represent the total number of nodes in each direction.

Case	L_x	L_z	$N_x \times N_y \times N_z$	Δx^+	Δz^+	Δy^+_{min}	Δy^+_{max}
Channel Flow	3.2δ	6.4δ	$190 \times 150 \times 166$	3	7	0.3	7

In Figures 3.2 and 3.3, we present results that have been time and space averaged. In space, the measurements were averaged over the spanwise and streamwise directions. Figure 3.2 plots streamwise velocity in the near-wall region and shows an excellent agreement with the law of the wall. Turbulent statistics were also computed and are shown in Figure 3.3. These too, show good agreement with established turbulent boundary layer profiles from Kim et al. [12]. Spectra near the no-slip boundary condition is shown in Figure 3.4. The Kolomogorov region ($-5/3$ slope) is apparent, as is the turbulence production region (-1 slope). There are high frequencies of turbulence about four decades below low frequencies, which is evidence that there is no apparent buildup of energy at the high frequencies. This, in turn, indicates that the relevant scales of turbulence are present without a closure model (proper dissipation of energy occurs).

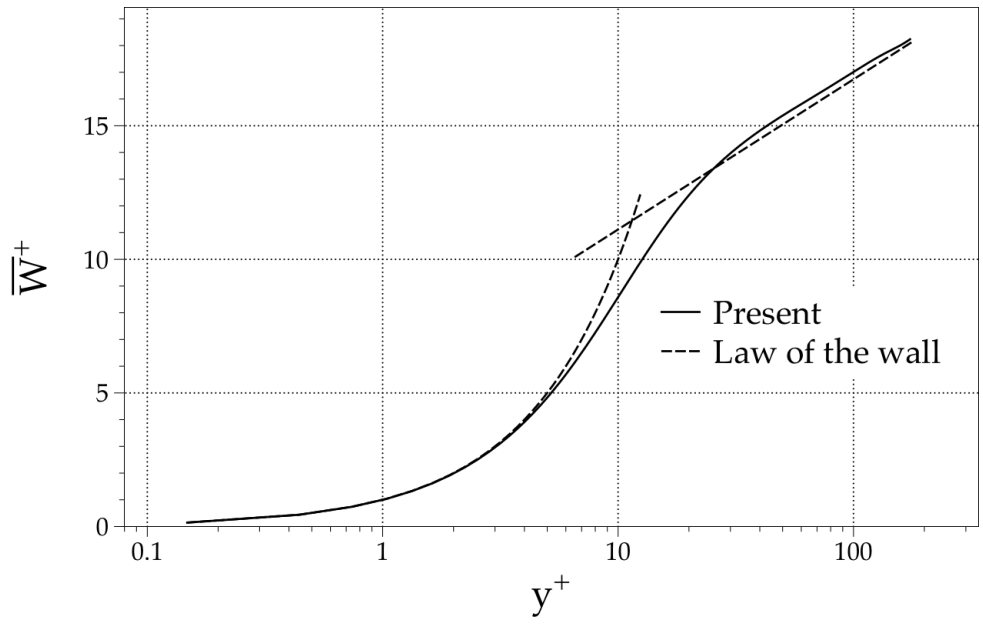

Figure 3.2: Mean streamwise velocity. Compared with the law of the wall: $u^+ = y^+$ and $u^+ = 2.44ln(y^+) + 5.5$.

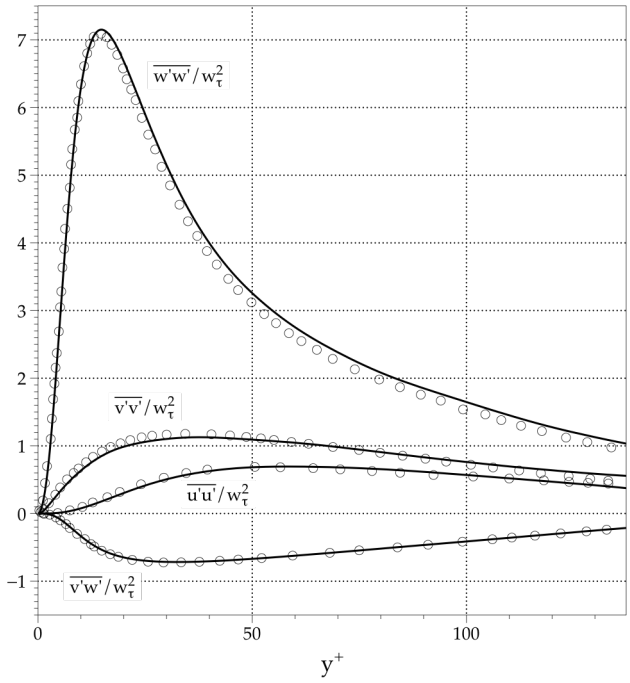

Figure 3.3: Reynolds stresses for the DNS validation case. The open circles represent simulated data from Kim et al. [12].

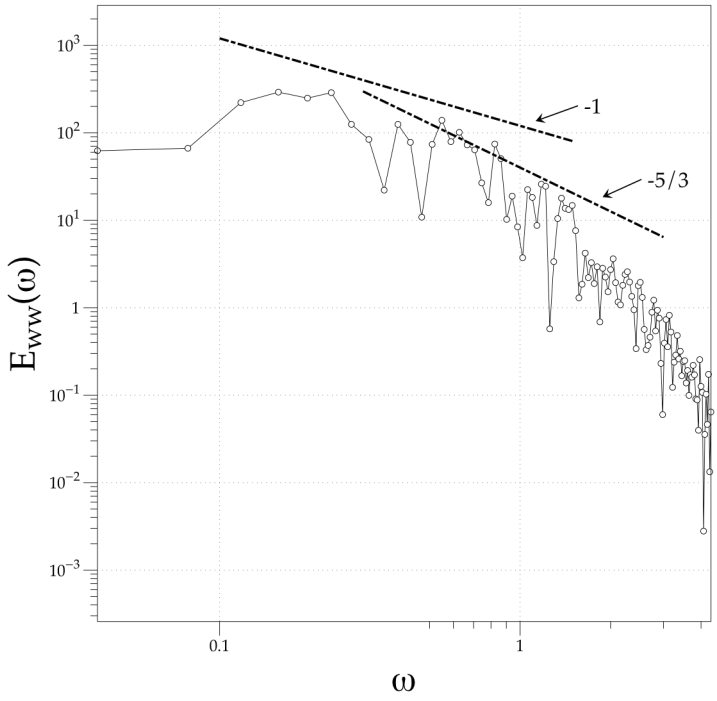

Figure 3.4: Power spectral density of streamwise velocity fluctuations at a point $y^+ = 36$ for the DNS validation case. Spectra is sampled from the middle (in both spanwise and streamwise directions) of the domain.

3.0.2 Riblet Simulation Validation.

In order to gain experience with modeling riblets and to validate the function of the numerical model with a curvilinear grid, a v-groove riblet, previously simulated by Choi et al. [13], was chosen as a validation case. The computational domain is shown in Figure 3.5. An inset is included to show the quality of the mesh used to discretize the domain. Note that here, δ is the half-channel height and s, h denote the riblet's width and height. In this riblet simulation, the total height of the domain, L_y, is actually $L_y = 2\delta + h/2$, similar to the computational domain of Choi et al. [13].

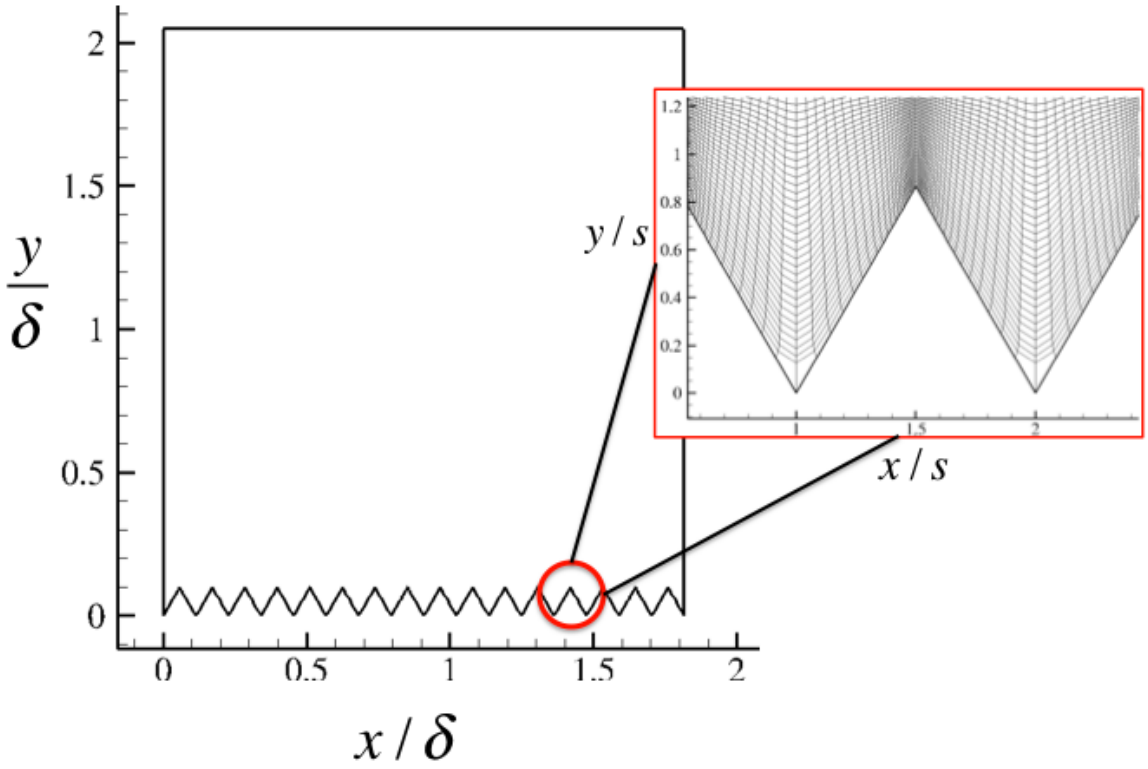

Figure 3.5: Front view of riblet validation domain. Flow is into the page. The inset shows mesh quality near riblet surface.

While simulating this case, we found that the quality of the grid is very important to obtain accurate results–specifically the smoothness of the domain. Obviously, v-groove riblets have very sharp peaks, which means that smooth meshes are difficult to achieve.

For this reason, the riblets simulated in Chapter 4 are smooth-rounded scalloped riblets. Details concerning the computational domain size and grid cell counts are shown in Table 3.0.2.

Table 3.2: Details of the computational grid for the riblet validation case. N_x, N_y, and N_z represent the total number of nodes in each direction.

Case	L_x	L_z	$N_x \times N_y \times N_z$	Δz^+
Channel Flow	1.816δ	3.2δ	$737 \times 193 \times 113$	7.5

The minimum values of Δy^+ and Δx^+ are not included in Table 3.0.2 since they are $<< 1$. The streamwise grid spacing is typical for DNS channel flow (see Kim et al. [12]). Similar to the DNS validation case, the turbulent flow was simulated via DNS at $Re_\tau \approx 180$. The corresponding bulk flow Reynolds number is $Re = W_{bulk}\delta/\nu = 2800$. The non-dimensional riblet spacings are $s^+ = 20.4$ and $h^+ = 17.7$. and the timestep was such that $CFL_{max} \approx 0.7$. After the mean kinetic reached statistically stationary value, time averaging occurred for $350\delta/W_{bulk}$ nondimensional time units. For this validation, a no-slip boundary condition was applied at the top of the domain and also on the bottom of the domain at the riblet surface. Lastly, periodic boundary conditions are employed in the spanwise and streamwise directions.

The results plotted in Figures 3.6 - 3.10 show data that has been averaged in time and space. Spatially, the results were averaged in the spanwise and streamwise directions. However, in the spanwise direction, results were conditionally averaged (i.e., averaging occurred on a per-riblet basis) in order to preserve data within the riblet. Figure 3.6 plots streamwise velocity across the wall-normal direction. The computational data of Choi et al. [13] has been included for comparison.

Figures 3.7, 3.8, and 3.9 plot turbulence statistics. There are some minor discrepancies, but in general, very good agreement is achieved–especially given that the present domain is twice as wide, the streamwise grid spacing is five times finer, and has been averaged for a longer time.

Finally, Figure 3.10 shows the local time and space averaged wall shear stress for the riblet validation case. As one traverses the riblet surface from valley to peak, very good agreement is observed. In the present case, the riblets produced a total drag reduction of 5.4% compared to a flat plate, and Choi et al. [13] reports a drag reduction of 6%.

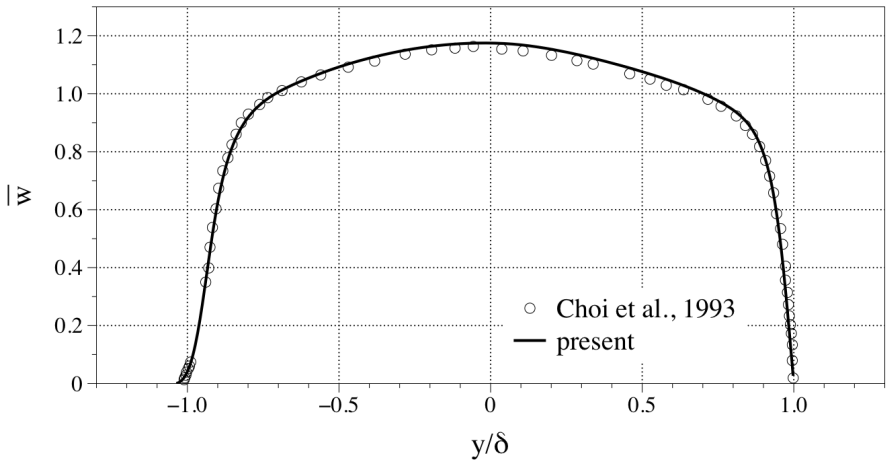

Figure 3.6: Mean streamwise velocity as a function of wall-normal location. Circles are computational data from the work of Choi et al. [13].

With these results, our approach to modeling riblets and numerical solver was considered validated.

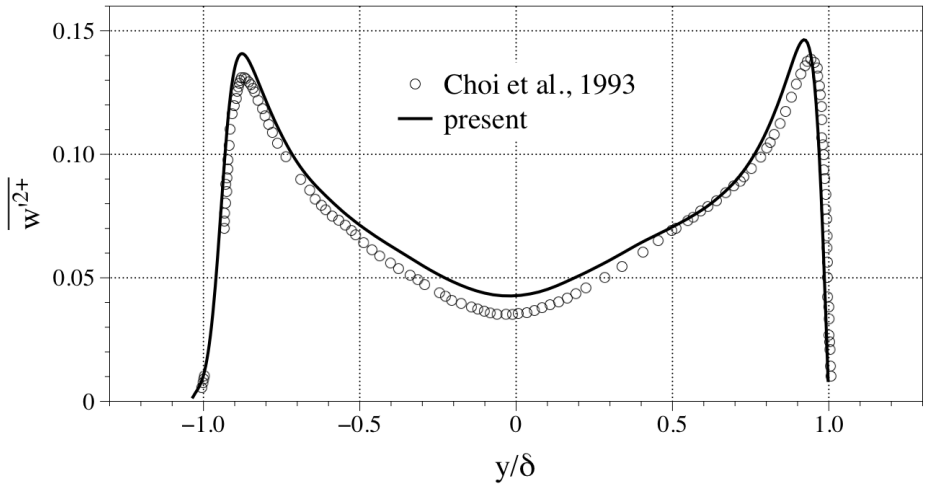

Figure 3.7: Streamwise turbulence intensities as a function of wall-normal direction. Circles from the work of [13].

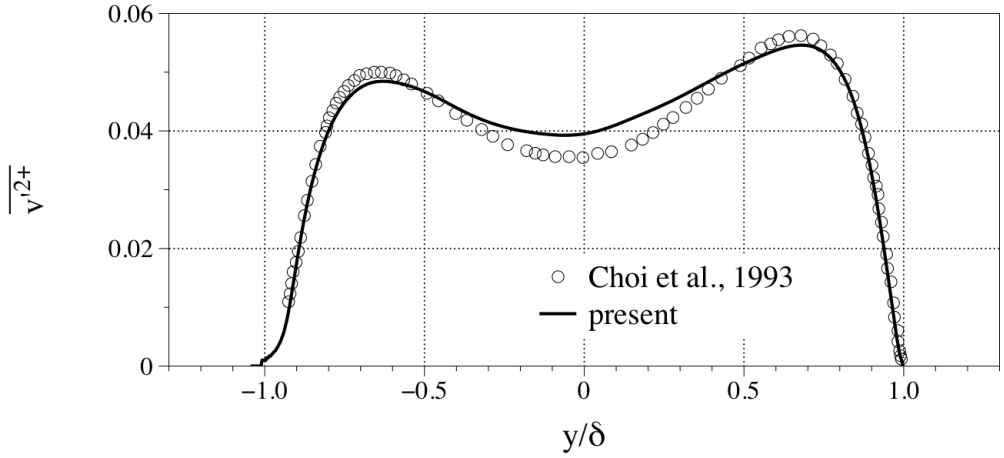

Figure 3.8: Wall-normal turbulence intensities as a function of wall-normal direction. Circles from the work of [13].

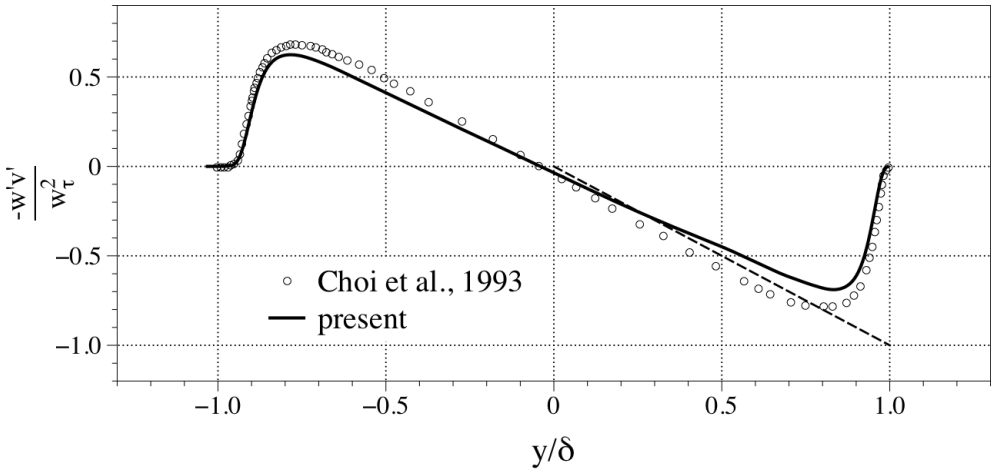

Figure 3.9: Primary Reynolds shear stresses as a function of wall-normal direction. Circles from the work of [13]..

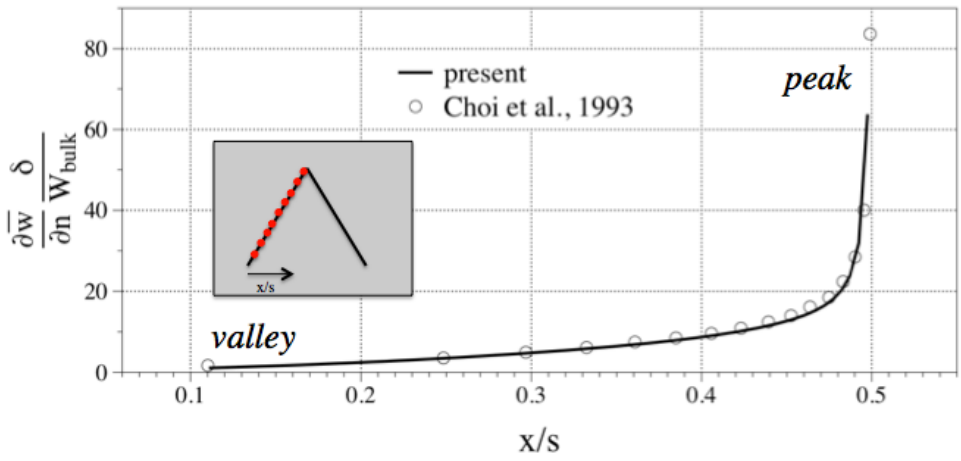

Figure 3.10: Local wall shear stress from valley to peak on a riblet surface. Circles from the work of [13].

3.0.3 Spatially Developing Boundary Layer Validation.

To validate our implementation of the rescaling method of Lund et al. [67], we have simulated a canonical Spatially Developing Turbulent Boundary Layer (SDTBL) with $Re_\theta = 1,750$ and compared it with similar SDTBL found in the current literature. A front view of the test domain is shown in Figure 3.11. The mesh is uniform in the spanwise and streamwise directions. Normal to the wall, a clustered grid is used that has a constant stretching ratio of 1.05. Domain specifications are highlighted in Table 3.0.3. The domain lengths are relative to the boundary layer height at half of the streamwise length, δ_{mid}. This domain is similar to the validation domain of Lund et al. [67].

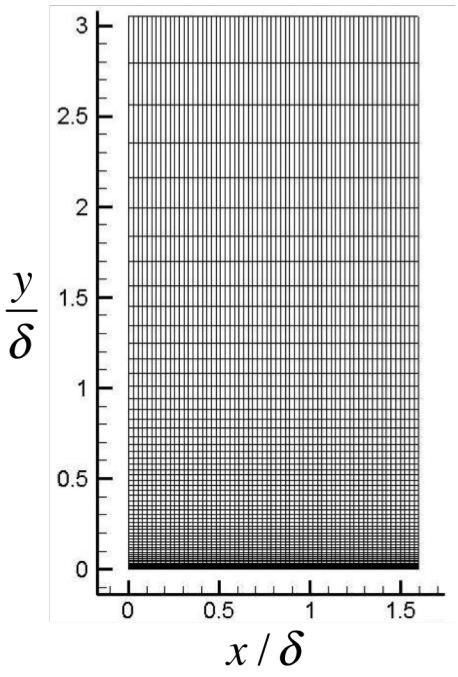

Figure 3.11: Computational domain and mesh for the SDTBL validation case. Streamwise direction is into the page.

Grid spacings are as following: $\Delta x^+ = 15$, $\Delta z^+ = 30$, and $\Delta y^+_{min} = 0.3$. Figure 3.12 shows a side view of instantaneous contours of streamwise velocity. Also plotted are vectors of mean streamwise velocity at the inlet and recycling plane, which is at 85% of L_z. The dashed line is the local mean boundary layer height.

Table 3.3: SDTBL validation grid specifications. δ_{mid} is the boundary layer height at the middle of the domain in the streamwise direction. N_x, N_y, and N_z represent the total number of nodes in each direction.

Case	L_x	L_y	L_z	$N_x \times N_y \times N_z$
SDTBL	$(\pi/2)\delta_{mid}$	$3\delta_{mid}$	$10\delta_{mid}$	$64 \times 100 \times 200$

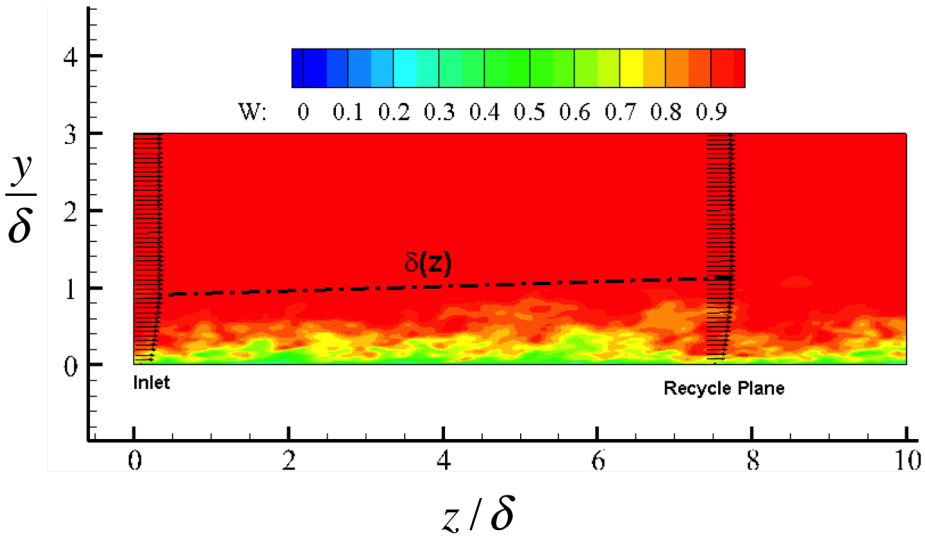

Figure 3.12: A side view of the SDTBL validation case computational domain plotted with contours of instantaneous streamwise velocity. The dashed line is the local mean boundary layer height. Vector profiles are plotted at the inlet and recycling plane.

Mean streamwise velocity is plotted in Figure 3.13, along with the law of the wall. The flow field has been averaged in the spanwise direction only since the boundary layer is developing in the streamwise direction. Excellent agreement with the computational data of Lund et al. [67] is achieved.

Lastly, turbulence statistics are plotted in Figure 3.14. For comparison, Laser Doppler Anemometry (LDA) results from De Graaff & Eaton [14] are also shown. Also plotted are computational results from Araya et al. [15]. There is a slight difference in Reynolds number from both comparisons. In general, very good agreement is seen, though the peak value of streamwise fluctuations varies by about 5%. After many SDTBL simulations, this minor variation seems to be a product of the rescaling method.

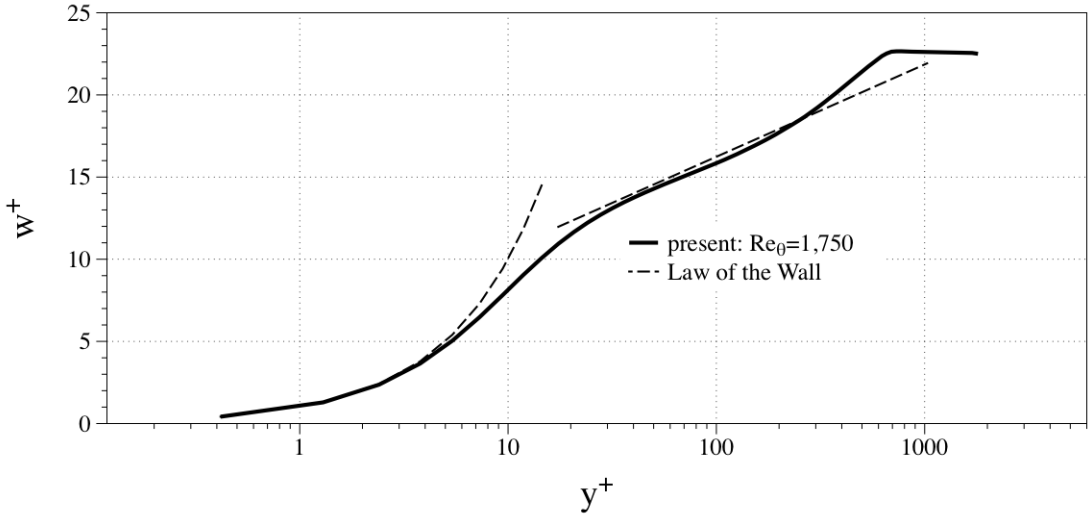

Figure 3.13: Mean streamwise velocity as a function of wall-normal direction. Dashed lines correspond to the law of the wall. In the logarithmic region, $w^+ = 2.44ln(y^+) + 5$.

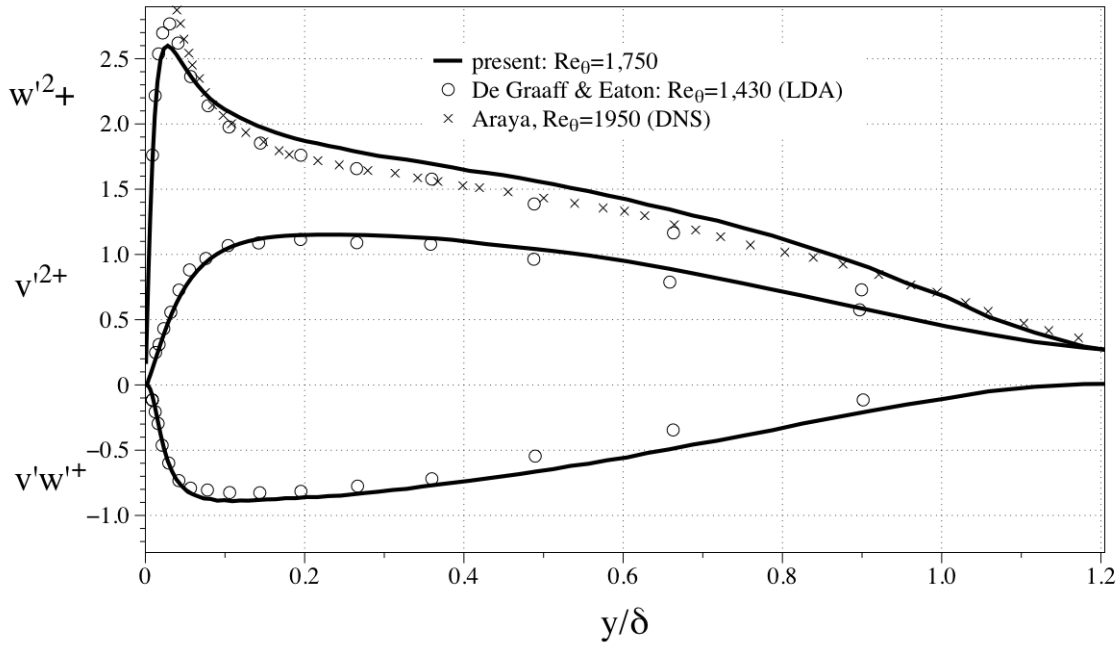

Figure 3.14: Turbulence statistics for the present SDTBL with $Re_\theta = 1,750$. Experimental measurements (circles) are of a boundary layer with $Re_\theta = 1,430$ and are from DeGraaff & Eaton [14]. Computational results (x markers) are of a boundary layer with $Re_\theta = 1,950$ and are from Araya et al. [15].

3.0.4 CURVIB Validation.

Two cases were simulated to validate CURVIB: 1) a case to accurately calculate shear stress on an immersed boundary, and 2) a case to accurately model the flow field around both stationary and moving boundaries. Each of the cases are two-dimensional, laminar flows around a cylinder of diameter, d. The Reynolds number, $Re_d = dW_{bulk}/\nu = 10$.

The first test case is a single cylinder in cross-flow. Figure 3.15 shows the computational domain with the background mesh. The cylinder is centered at $y/d = 0$ and $z/d = 30$ and the mesh is stretched in both directions to reduce computational expense. A uniform velocity of W_{bulk} is provided at the inlet. The slip boundary condition is applied at the top and bottom of the domain, and at the outlet, a the gradients of each Cartesian velocity is set to zero. Figure 3.16 illustrates a view of the cylinder and local discretization. The dark blue filled cells are structure nodes. The light blue indicates IB nodes, and the white cells are fluid nodes. Details concerning the computational grid for this validation case are shown in Table 3.4. The timestep was $0.004d/W$ and the solution was steady in time.

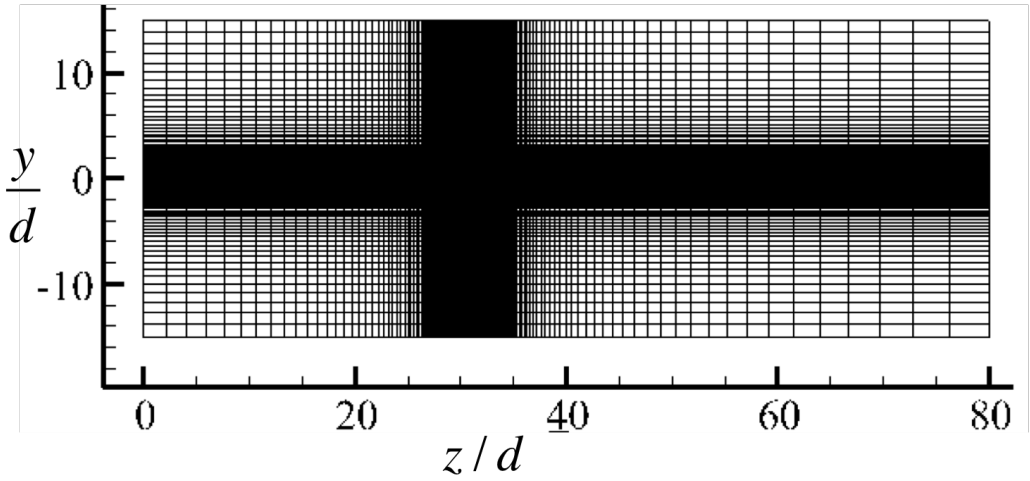

Figure 3.15: Two-dimensional domain and background grid with a single cylinder in cross-flow. Flow is from left to right.

Figure 3.17 shows streamlines around the cylinder. Figure 3.17a is plotted for comparison and is from the computational work of Lange et al. [70]. Figure 3.17b is the present solution. The ratio between separation bubble length to diameter is, $l/d = 0.25$, which is

Table 3.4: Single cylinder in cross-flow computational grid details. N_y and N_z refer to the number of grid nodes in the wall-normal and streamwise directions, respectively.

Case	L_y	L_z	$N_y \times N_z$
Single cylinder in cross-flow	$30d$	$80d$	268×558

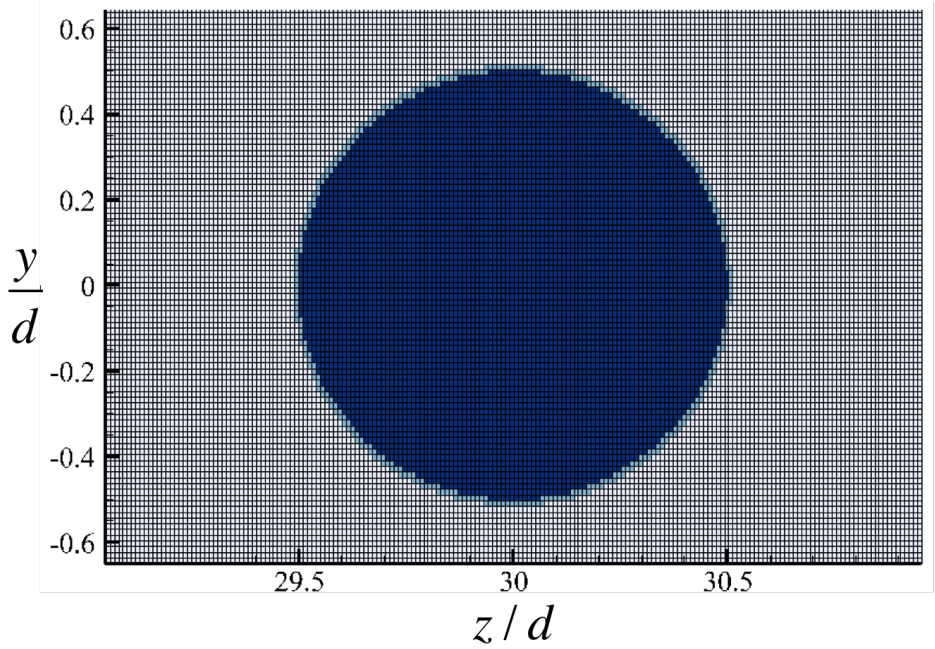

Figure 3.16: Local background grid and CURVIB node classifications: dark blue: structure nodes, light blue: IB nodes, white: fluid nodes.

in agreement with Lange et al. [70]. Lastly, the drag coefficient, C_D, with accounts for pressure and viscous drag was 2.8, also in agreement with that reported by Lange et al. [70].

The second validation case for CURVIB is laminar flow with three cylinders in crossflow– each with a negative (i.e., moving in the opposite direction to the mean flow) constant velocity. The purpose of this validation case is to ensure proper drag calculation even when the immersed body is moving with a relative velocity. We originally planned to simulate dynamic sharkskin, as detailed in Appendix C. Although we later chose to simulate static denticles, this validation case remains important. There are two simulations for this

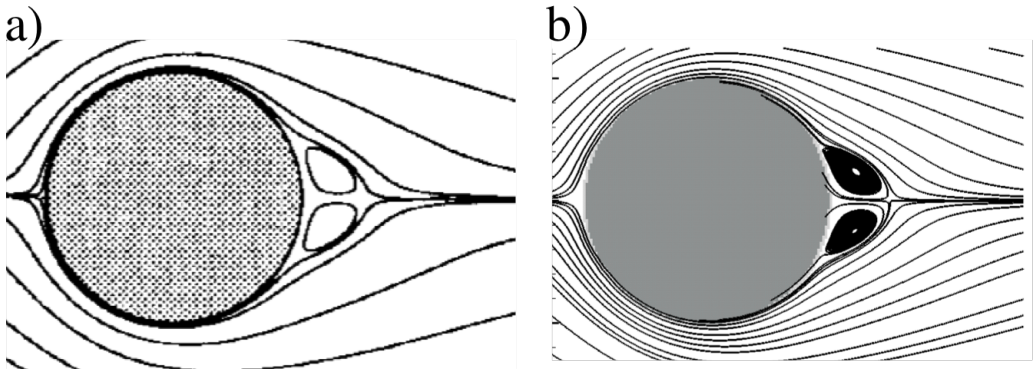

Figure 3.17: Instantaneous streamlines for a single cylinder in cross-flow: a) computational results are from Lange et al. [70], b) present results.

second validation and Figure 3.18 shows the two-dimensional domains used for this case. In Figure 3.18a the cylinders are fixed in space, and for Figure 3.18b, the cylinders move to the left at velocity, c. The Reynolds number is $Re_d = 10$ for both simulations, where the characteristic velocity is the *relative* velocity between the fluid and immersed boundary velocities. The space between cylinders is $6d$ and periodic boundary conditions are applied in the streamwise directions. Domain sizes and cell counts are found in Table 3.5.

Table 3.5: Three cylinders in cross-flow computational grid details. N_y and N_z refer to the number of grid nodes in the wall-normal and streamwise directions, respectively

Case	L_y	L_z	$N_y \times N_z$
Three cylinders in cross-flow	$10d$	$18d$	328×961

Figure 3.19 plots mean streamwise velocity at three different planes downstream from a single cylinder for both moving and stationary immersed boundaries. The location of each measurement plane is shown in the inset figure. Excellent agreement is seen with the stationary cylinders. Lastly, Figure 3.20 plots the drag coefficient (C_D for each cylinder) varying in time. In actual implementation of this case, four immersed boundaries were used, though at any time, only three are in the domain since. During time step $2500 - 3000$, IB_1 exits and IB_3 enters the domain. Afterwards, a stable C_D is seen for all bodies.

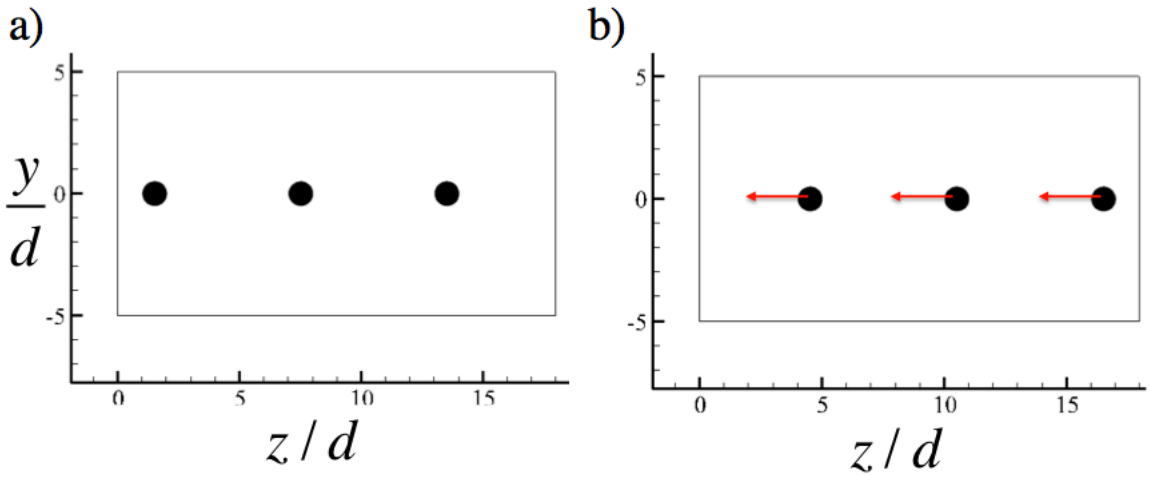

Figure 3.18: Computational domains for the second CURVIB validation case. a) The domain includes three stationary cylinders in cross-flow. b) The domain includes three cylinders with a prescribed velocity in the negative z direction. Reynolds numbers for each case are identical.

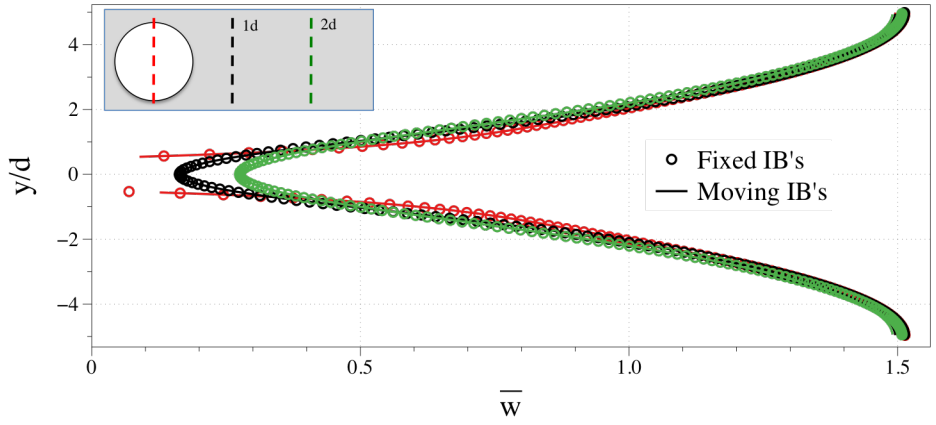

Figure 3.19: Streamwise velocity profiles at three planes at and downstream of an arbitrarily selected cylinder (shown in inset). Circles represent computational data from the simulation with fixed immersed boundaries, whereas the straight line represents data from the case with moving immersed boundaries.

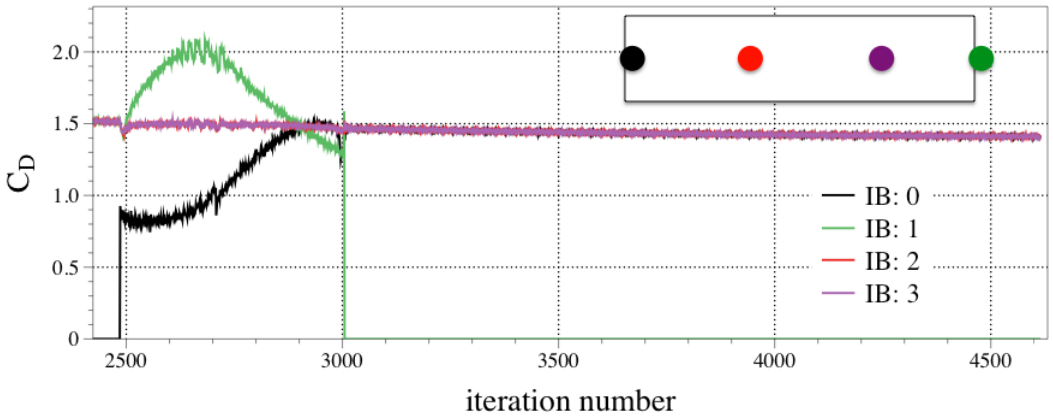

Figure 3.20: Time-varying drag coefficients for each moving cylinder. Four immersed boundaries are used, though at any time only three are in the computational domain.

Chapter 4

Riblets

In this section, we present results from several simulations of drag-reducing riblets in two different pressure gradients. Their drag reducing potential is analyzed as well is flow fields within individual riblets.

4.1 Inlet Turbulent Flow & Boundary Conditions

As was mentioned in Section 1.1.3, most riblet research to date has been done in fully developed, turbulent channel flows. While this is an effective method to study fundamental flow physics near riblets, many practical implementations will expose riblets to varying pressure gradients; specifically, Adverse Pressure Gradients (APG). To further fundamental research of riblets in APG, we have simulated several riblet geometries in both a Zero Pressure Gradient (ZPG) and an APG. Though, in order to simulate a turbulent boundary layer with either type of pressure gradient, it is essential that realistic turbulent inflow boundary conditions are used. To accomplish this, we employed the rescaling method of Lund et al. [67]. When compared with other methods (parallel inflow method & synthetic turbulence), the rescaling technique is superior at generating realistic scales of turbulence that do not dissipate prematurely. A series of domains is used to implement the rescaling method as shown in Figure 4.1. The rescaling domain is seen in Figure 4.1a. In this domain, velocities from a recycling plane (red dashed line at 85% of domain length, L_z) are scaled and re-fed into the inlet. The result is a spatially developing turbulent boundary

layer with a fixed inlet boundary layer height, δ. After reaching a statistically steady state, velocities are saved at the recycling plane and used as an inflow boundary condition for the development domain, (Figure 4.1b). Velocities are stored at the dashed line of the development domain and finally fed into the riblet domain (Figure 4.1c), which contains either the riblet films or the flat-plate baseline. Note that the z direction is normalized with the momentum thickness at the inlet of the development domain, θ_{inlt}.

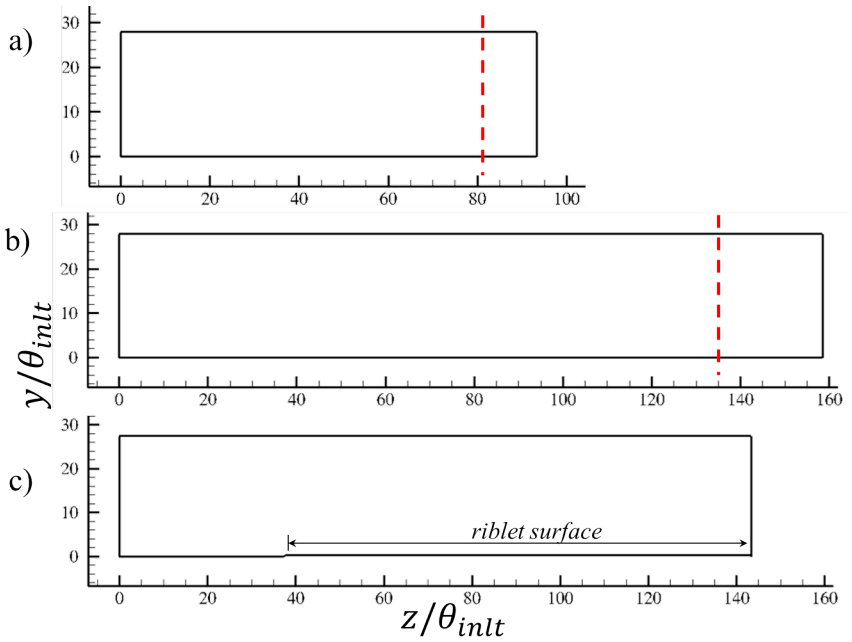

Figure 4.1: Side view (flow is from left to right) of a) rescaling domain b) development domain, and c) riblet domain. θ_{inlt} is the momentum thickness at the inlet of Domain B. The red dashed lines denote planes where velocities are stored and fed into the next downstream domain.

The development domain is used to allow for sufficient development of the APG, creating an equilibrium boundary layer (i.e., $\beta \approx constant$). As mentioned above, riblets often reduce drag by just a few percentage points. So in order to make an accurate comparison among riblet sizes, it was critical that each different riblet size be exposed to the exact same turbulent boundary layer. Therefore, we adopt the following approach: the APG and ZPG flows were each separately matured using the mesh from the development domain. The resulting flow fields from the development domain were then fed into several different

riblet domains. Each riblet domain has a cross-section slightly different (accounting for differing riblet s^+) from the development domain. Thus, velocities from the development domain were interpolated onto the different riblet inlet grids, ensuring each riblet received the same inflow. It is important to note that the interpolation did not adversely affect profiles of mean velocity nor turbulence statistics. Such an interpolation is valid because, as will be seen in Section 4.2, the spanwise grid spacing in the development domain is below one wall unit.

For all APG flows, the streamwise pressure gradient is controlled by the wall-normal velocity (i.e., a flux) at the top of each domain. We took this approach because the hybrid staggered/non-staggered methodology we employ to discretize the governing equations (see Gilmanov & Sotiropoulos [61]) stores contravariant fluxes at boundaries. Equations 4.1 and 4.2 are employed at the top of each domain using Cartesian velocities at ghost cells.

$$\frac{\partial w}{\partial y} = \frac{\partial u}{\partial y} = 0 \tag{4.1}$$

and

$$v(z) = W_e \frac{d\delta^*}{dz} + (\delta^* - L_y)\frac{dW_e}{dz} \tag{4.2}$$

where $W_e(z)$ is the free-stream velocity. Equation 4.2 originates from the integral momentum balance and definition of the displacement thickness, as described by Lund et al. [67]. In ZPG flows, $dW_e/dz = 0$. But for APG flows, $W_e(z)$ is known *a priori*. Figure 4.2 is a plot of the prescribed $W_e(z)$ as a function of the streamwise direction. Here, and from now on, note that $z/\theta_{inlt} = 0$ corresponds to the beginning of the development domain. In this figure, the dashed line at $z/\theta_{inlt} = 160$ represents the boundary between development and riblet domains. From $0 \leq z/\theta_{inlt} \leq 80$ a ZPG exists where

$$W_e(z) = W_0$$

after which the streamwise velocity is specified using Equation 4.3.

$$W_e(z) = W_0 \left(1 - \frac{z}{z_0}\right)^m \tag{4.3}$$

where $m = -0.075$ and $z_0 = -6.53$. This velocity profile is similar to that used in the work of Lee & Sung [71]. The result is an equilibrium boundary layer in the riblet domain where

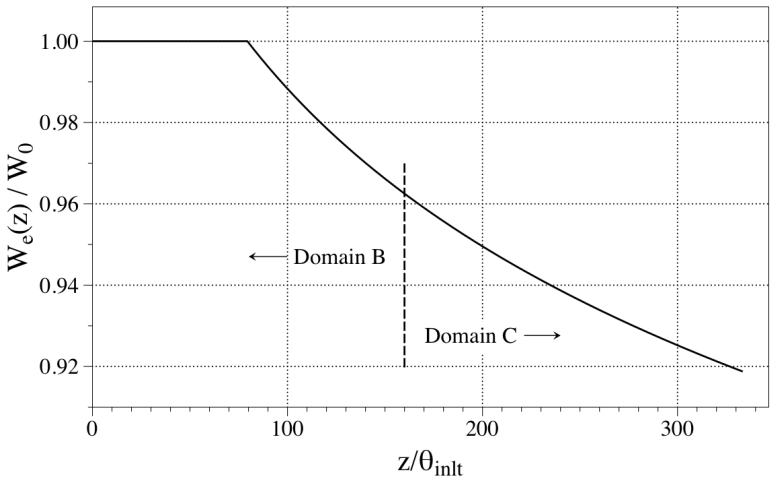

Figure 4.2: Prescribed streamwise variation of free-stream velocity, $W_e(z)$, for the development and riblet simulations. This profile is used in conjunction with Equation 4.2 to specify the boundary condition at the top of the respective computational domain.

$\beta \approx 0.5$, as shown in Figure 4.3. Skin-friction coefficients are also shown for the ZPG and APG baseline cases, i.e. a flat-plate without riblets.

The no-slip boundary condition is employed on the riblet and flat-plate surfaces and in the spanwise direction, the periodic boundary condition is applied. The convective boundary condition, $\partial U^i/\partial t + c\partial U^i/\partial z = 0$, where c is the integrated bulk velocity across the entire outlet domain, is applied at the domain outlets. To help ensure convergence of the Poisson equation to machine zero, a mass flux correction (difference in inlet and outlet mass fluxes) is applied to each cell on the outlet. This difference is typically very small, less than 0.005% of the total mass flux.

4.2 Computational Details

Computational domain lengths, cell counts, and grid spacing for the rescaling and development domains are shown in Tables 4.1 and 4.2.

We consider herein five different riblet geometries and carry out a total of eight separate riblet simulations. Figure 4.4 shows the scalloped riblet geometry we simulate. The riblet height-to-width ratio is $h/s = 0.5$. We have defined the riblet tip thickness, t, at 95%

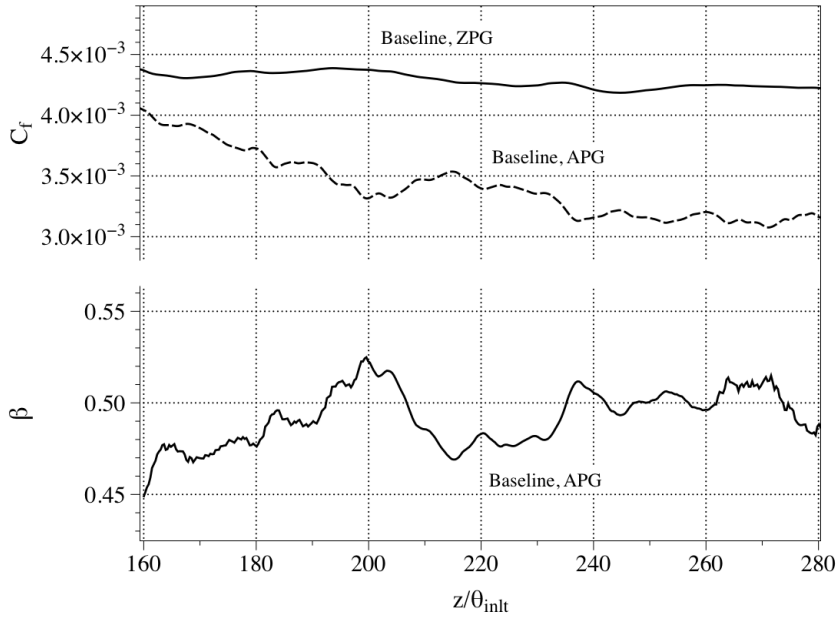

Figure 4.3: (Top) Skin-friction coefficient of the baseline case for ZPG and APG flows. (Bottom) The Clauser parameter for the baseline APG case. Note that $z/\theta_{inlt} = 160$ corresponds to the beginning of the riblet domain.

of the riblet height such that $t/s = 0.06$. This riblet is not an optimally designed blade riblet, but the rounded tips enable better grid quality. The riblets are discretized with a body-fitted, structured grid as shown in Figure 4.4. Since the individual scalloped riblets are only tens of wall units in width, a very fine grid is required to accurately calculate mean shear stresses and turbulence statistics.

Table 4.3 details case-specific domain geometries for the ZPG and APG riblet simulations. The naming convention for each riblet case is such that s^+ increases as one proceeds alphabetically. Note that ZPG and APG flows with the same riblet cases (i.e., Riblets A, C, & E) use the same mesh. Also shown in Table 4.3 is the number of individual riblets in the spanwise direction, N_{ribs} along the spanwise length, L_x. To help reduce the computational expense of these simulations, we used N_{gp} (the number of grid nodes per riblet) nodes for only *half* of the number of riblets, N_{ribs}. In other words, half of the total number of individual riblets are highly resolved and the remaining half are resolved with a coarser resolution. The highly resolved riblets were centered in the spanwise direction,

Table 4.1: Rescaling & development domain specifics (see Figure 4.1 for definitions of the two domains). N_x, N_y, and N_z are the numbers of grid nodes in the spatial directions.

Domain	$\frac{L_x}{\theta_{inlt}}$	$\frac{L_y}{\theta_{inlt}}$	$\frac{L_z}{\theta_{inlt}}$	N_x	N_y	N_z
Rescaling	16.2	28	94	400	80	401
Development	16.2	28	160	721	125	521

Table 4.2: Rescaling & development domain grid spacing.

Domain	Δx^+	Δy^+_{min}	Δy^+_{max}	Δz^+
Rescaling	1.6	0.5	68	9.5
Development	0.9	0.7	45	12

approximately $4.05 \leq x/\theta_{inlt} \leq 12.1$. Flow fields near the coarser regions were not used for any drag calculations. The motivation for retaining the coarsely resolved riblets was to diminish two-point correlations (as defined in Equation 4.4). Table 4.4 shows the domain cell counts. For each simulation, Δy^+ and $\Delta x^+ << 1$, and therefore only Δz^+ is reported.

Table 4.3: Riblet widths in wall units (s^+), total number of riblets in the spanwise direction (N_{ribs}) and the number of grid points used to highly resolve each riblet (N_{gp}).

Case	s^+_{ZPG}	s^+_{APG}	N_{ribs}	N_{gp}
A	10	8.5	66	35
B	14.7	$--$	43	33
C	17.1	15	37	33
D	$--$	17	33	33
E	26.6	23.4	24	39

In Table 4.3, the shear velocity used to normalize the riblet widths is $w_{\tau,0}$, which is set equal to the average shear velocity from the corresponding ZPG and APG baseline (smooth flat plate) cases. Figure 4.5 illustrates how the turbulent inflow was generated for the riblet cases. Our approach ensures that each riblet geometry is exposed to the same turbulent boundary layer. This is crucial because the drag reduction produced by some riblets is often only a few percentage points.

The left side of Figure 4.6 shows a longitudinal plane with contours of instantaneous streamwise velocity in a particular riblet domain. The flow is from left to right. To make the transition from flat-plate ($0 \leq z/\theta_{inlt} \leq 40$) to riblet, a smooth transition was implemented as illustrated in Figure 4.6.

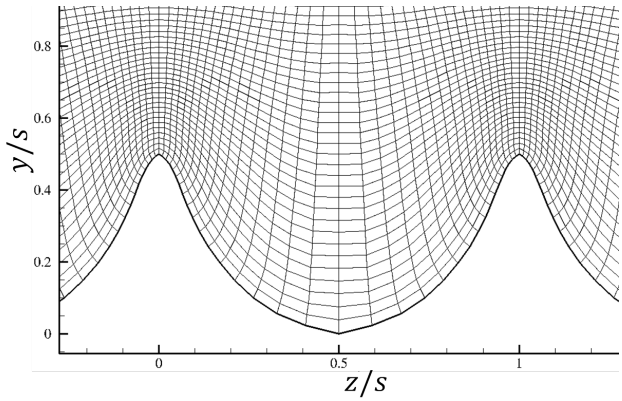

Figure 4.4: Scalloped riblet body-fitted curvilinear mesh from Riblet Case A.

Table 4.4: Number of grid nodes in each direction and streamwise grid resolution for the riblet domains.

Case	N_x	N_y	N_z	Δz^+
A	1565	145	548	11
B	1025	140	520	11
C	897	140	520	11
D	801	140	520	11
E	721	130	513	11

A grid independence study was conducted for each case to ensure that any drag measurements were not a function of grid size or quality. Grid cell counts in the spanwise and wall-normal directions were increased by a factor of 1.5 independently. The grid size was not altered in the streamwise direction since, as shown in Table 4.4, $\Delta z^+ = 11$ is already near DNS quality and it has been well established that the highest velocity gradients occur in the spanwise and wall-normal directions (see Choi et al. [13] and Chu & Karniadakis [36]). Local viscous stresses along the riblet surface and global viscous drag measurements were compared for coarse, medium, and fine grids. When considering varying resolutions in the spanwise direction, global values of viscous drag varied by just 1% between the medium and fine grids. In the wall-normal direction, the same drag varied by less than 0.5%. Therefore, the drag results were considered converged and grid independent.

For each riblet simulation, $L_x/\theta_{inlt} \approx 16.2$, $L_y/\theta_{inlt} \approx 28$, and $L_x/\theta_{inlt} \approx 145$ in the spanwise, wall-normal, and streamwise directions respectively. Following the works of

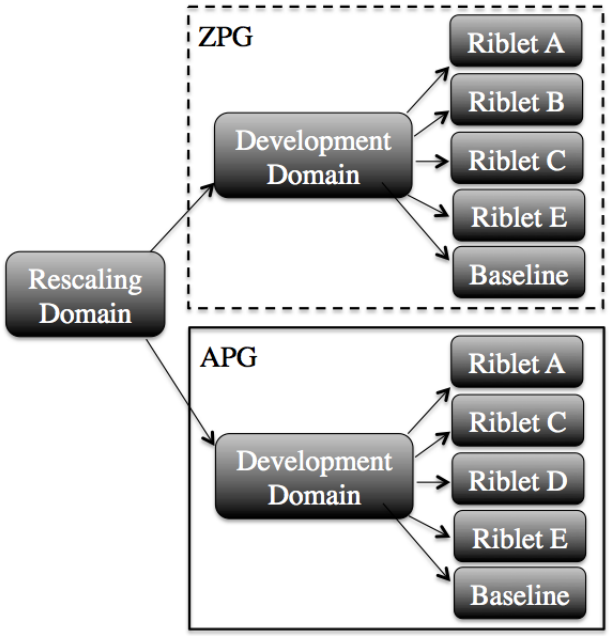

Figure 4.5: Flow chart of the procedure we employ to develop the turbulent boundary layer under zero and adverse pressure gradients to be used as inflow for the riblet and baseline simulations. Working from left to right, the rescaling domain turbulent flow is fed into the development domain for both APG and ZPG flows. Boundary layer growth occurs and then, turbulent flow from the development domains feed individual riblet and baseline cases.

Araya et al. [15] and Lund et al. [67], L_x is approximately $(\pi/2)\delta_{mid}$, where δ_{mid} is the 99% boundary layer thickness halfway between inlet and outlet of the ZPG control case. Two-point correlations were sampled to justify the domain sizes. These are defined as follows for each velocity component:

$$R_{ii} = \frac{\overline{u_i'(\mathbf{x},t)u_i'(\mathbf{x}+r,t)}}{\overline{u_i'^2}} \tag{4.4}$$

The so computed correlations are shown in Figure 4.7 for the spanwise and streamwise directions. The correlations were taken from the baseline ZPG turbulent boundary layer. One correlation was taken very near the wall and another near the boundary layer height. The characteristic length, δ_{mid} corresponds to the local boundary layer height at the middle of the domain in both streamwise and spanwise directions. As seen, the domain is large

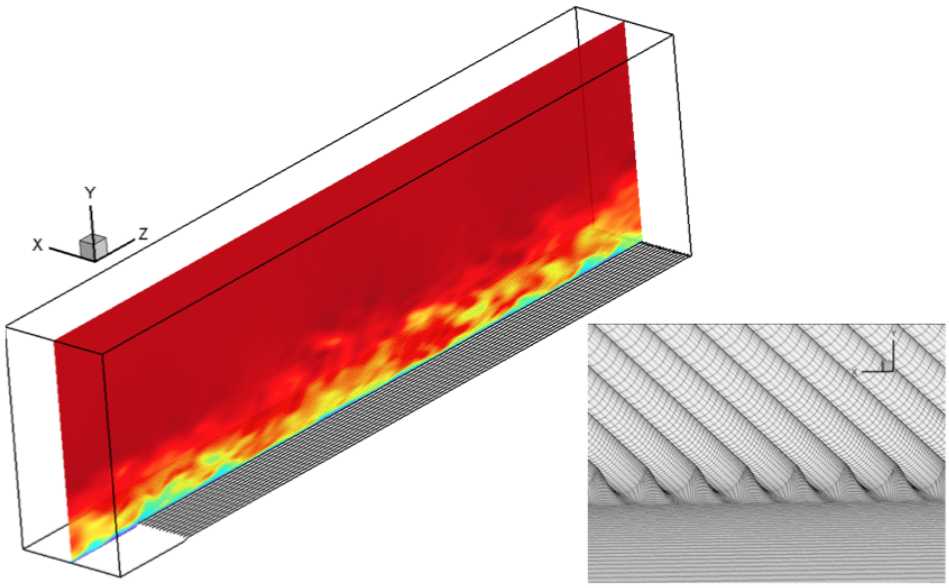

Figure 4.6: (Left) Instantaneous contours of streamwise velocity on a plane in a riblet domain. Flow is from left to right. (Right) Structure of the geometry and curvilinear grid in the vicinity where a swept surface transitions between the smooth boundary and riblet geometry.

enough such that the two-point correlations become uncorrelated for each velocity component in both the streamwise and spanwise directions and at each wall-normal location.

Finally, the Reynolds number at the inlet of the development domain is $Re_{\theta,inlt} = W_0\theta_{inlt}/\nu \approx 860$. The LES cases were initially run until the mean kinetic energy stabilized, then averaging occurred for 2,100 θ_{inlt}/W_0. The averaging time was long enough to ensure the mean viscous drag measurements no longer varied with time. The timestep was such that the Currant-Friedrich Lewis number (CFL) did not exceed $CFL_{max} \approx 0.6$.

4.3 Results

4.3.1 Inlet Turbulent Boundary Layer

Using the rescaling method to generate the boundary layer and the development domain to mature it to equilibrium (for the APG), a plane was recorded and fed as an inlet to the main simulation domain. To ensure the boundary layer's quality, we have compared it with

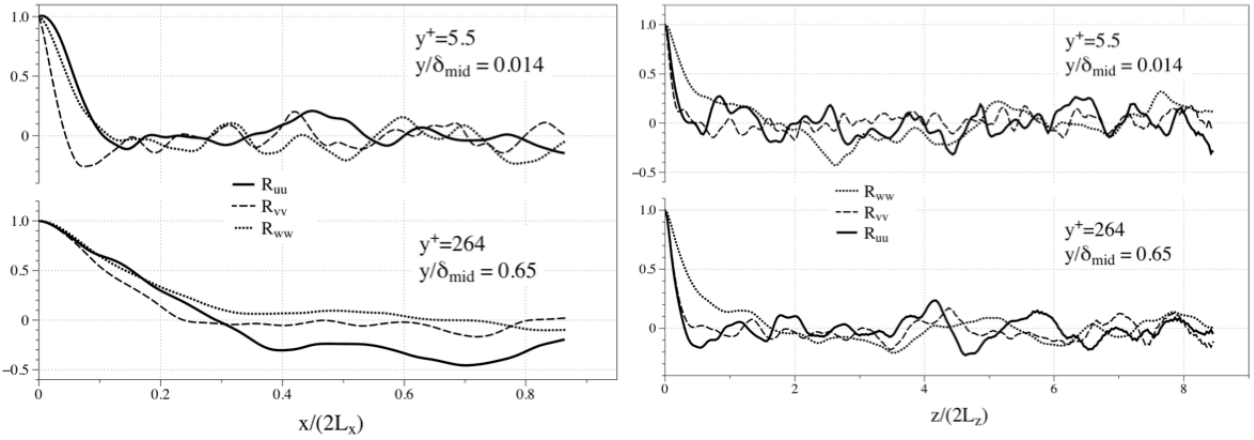

Figure 4.7: Two-point correlations in the spanwise (left) and streamwise (right) directions. Taken from the ZPG baseline case at two vertical locations, $y^+ = 5.5$ and $y^+ = 264$.

the experimental data from DeGraaff & Eaton [14]. Figure 4.8 compares the ZPG and APG baseline mean spanwise averaged streamwise velocity. The location at which this profile was sampled is $x/\theta_{in} = 190$ (near the inlet of the main simulation domain). The law-of-the-wall is plotted as reference. Excellent agreement is seen. The APG mean streamwise velocity has just a slightly different slope in the logarithmic region and as expected, its local $w_{\tau,0}$ is lower than that of the ZPG.

Also near the inlet, Figure 4.9 is a plot of the root-mean-square of the streamwise velocity fluctuations for both baseline cases. In comparison with the experiment, the ZPG case under predicts the streamwise fluctuation peak by about 7%, but otherwise, good agreement is achieved. The APG turbulent boundary layer shows an expected increase in fluctuations in logarithmic region. The maximum value of the secondary peak is a function of β. The present maximum peak for the APG baseline was compared (indirectly) with the boundary layers in Lee & Sung [71] with good results. Figure 4.10 shows mean spanwise-averaged wall-normal fluctuations. Again comparing with DeGraaff, very good agreement is seen.

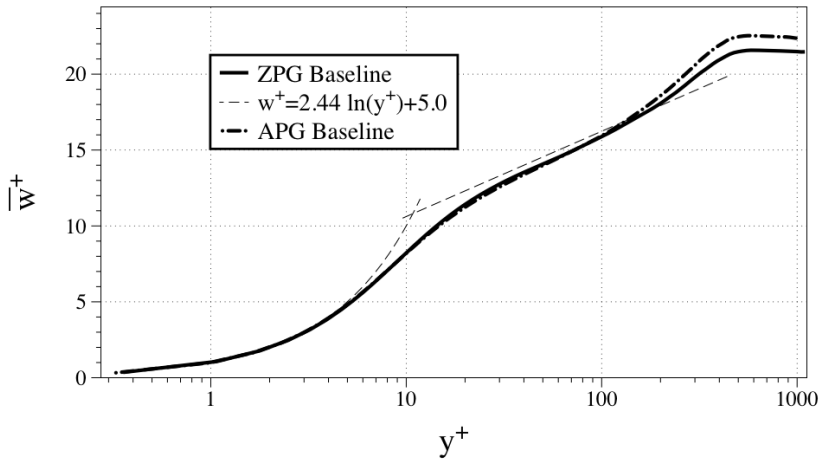

Figure 4.8: Mean spanwise-averaged streamwise velocity from both ZPG and APG baseline cases.

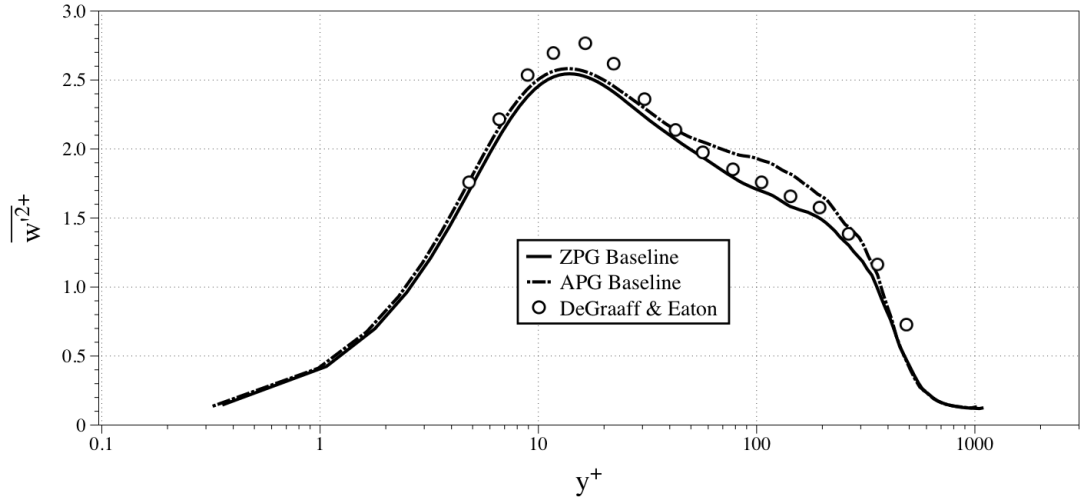

Figure 4.9: Mean spanwise averaged profiles from both ZPG ($Re_\theta = 1,150$) and APG ($Re_\theta = 1,250$) baseline cases. Circles from DeGraaff, 2000 (ZPG, $Re_\theta = 1,430$).

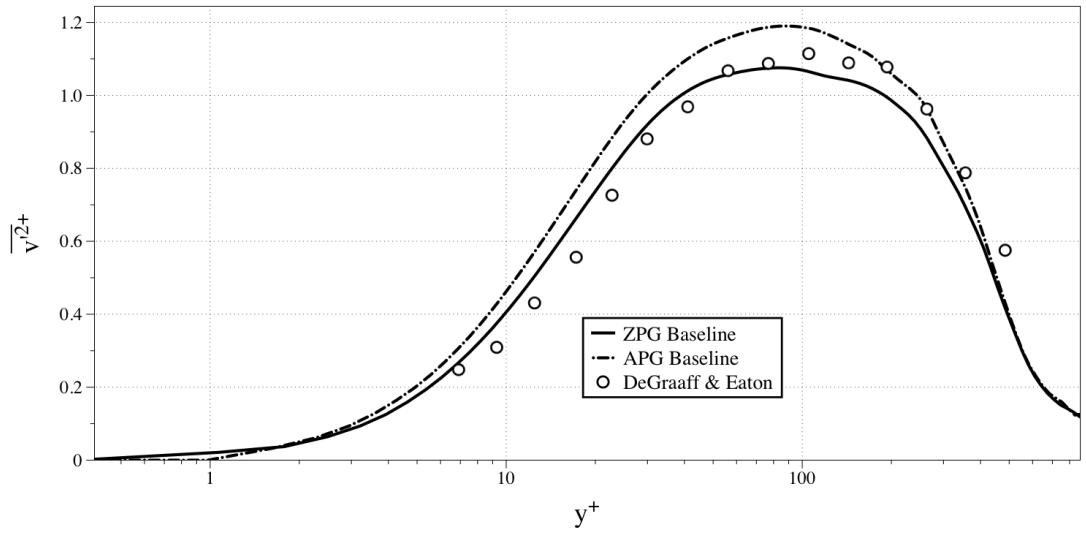

Figure 4.10: Mean spanwise averaged profiles of wall-normal fluctuations from both ZPG ($Re_\theta = 1,150$) and APG ($Re_\theta = 1,250$) baseline cases. Circles from DeGraaff, 2000 (ZPG, $Re_\theta = 1,430$).

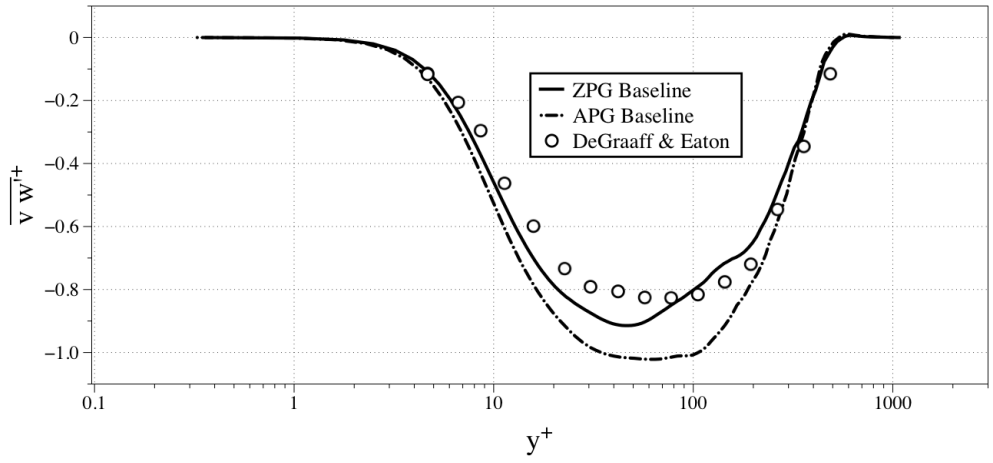

Figure 4.11: Mean spanwise averaged profiles of spanwise-averaged primary Reynolds stresses from both ZPG ($Re_\theta = 1,150$) and APG ($Re_\theta = 1,250$) baseline cases. Circles from DeGraaff, 2000 (ZPG, $Re_\theta = 1,430$).

Finally, the mean spanwise averaged primary Reynolds stresses are plotted for both baseline cases in Figure 4.11. The ZPG baseline case has a good comparison with the experimental data, though there is some difference, which is likely due to the averaging time. But, as was discussed in Section 4.2, despite this difference it was determined that the averaging time was sufficient.

Due to the boundary condition at the top domain, boundary layer properties (momentum thickness, θ and displacement thickness δ^*) grow at different rates depending upon the pressure gradient. Figure 4.12 shows the variation in both of these properties as a function of streamwise location. Due to the convective boundary condition at the exit plane of the domain, an artificial smoothing of the boundary layer growth occurs. As such, drag calculations are limited to $z/\theta_{in} = 310$.

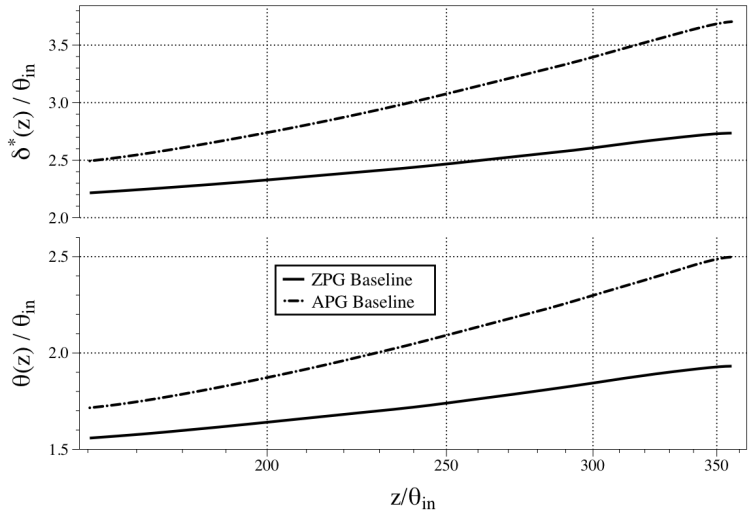

Figure 4.12: Mean spanwise-averaged momentum thickness and displacement thickness variations from both ZPG and APG baseline cases.

4.3.2 ZPG Riblets

Drag reduction by riblets will be reported in terms of $DR\%$, which is defined as:

$$DR\% = -\frac{D_{rib} - D_0}{D_0}$$

where D_{rib} is the viscous drag on the riblet surface and D_0 is the viscous drag on the baseline, flat place surface. The drag on the riblet surfaces are calculated as:

$$D_{rib} = \|D_i\| = \| \int_A \tau_{ij} n_j \mathrm{d}A \|$$

where τ_{ij} is the time-averaged wall-shear stress evaluated at the wall, n_j is the normal unit vector, and $\mathrm{d}A$ is the local cell area at the wall. The local shear stresses were only evaluated for the finely resolved riblets in the middle of the domain, which extended from $4.05 \leq x/\theta_{in} \leq 12.1$ in the spanwise direction. In the streamwise direction, the region from which drag forces were calculated extended from $218 \leq z/\theta_{in} \leq 310$.

Figure 4.13 shows the drag reduction by each riblet in the ZPG flow. The riblets have an optimum drag reduction of about 7%. The individual data points are from Walsh [27] and Bechert et al. [2]. The present data match very well with Walsh [27]. It is also important to note that the actual shape from either of these cases is not known. The problem is that many publications test 'scalloped riblets', but the definition (i.e., geometry) of a scalloped riblet has been quite arbitrary. Furthermore, neither author mentions the value of riblet tip-thickness and Bechert et al. [2] has already shown that the tip-thickness can affect drag reduction. Regardless, excellent agreement is achieved and our method of calculating riblet drag reduction in a spatially developing turbulent boundary layer is validated.

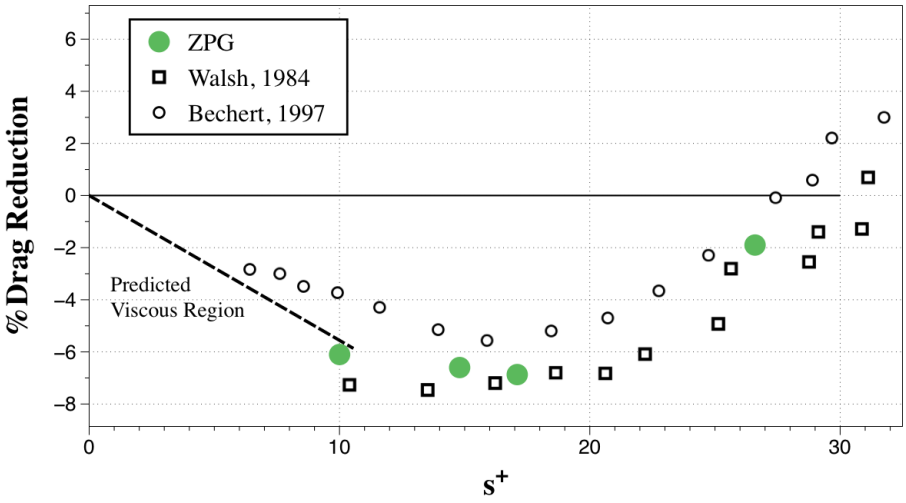

Figure 4.13: Time-averaged drag measurements from ZPG cases A, B, C, & E.

The dashed line in Figure 4.13 is the predicted viscous slope for the present riblet shape. As originally detailed by Luchini et al. [3], this theoretical slope is a function of the protrusion height, Δh. Briefly, the spanwise and streamwise velocity profiles each have a virtual origin i.e., where the no-slip condition would be applied if it were just a flat plate and an actual origin (the riblet surface). The difference between these two origins can thus be calculated in each direction, Δh_{span} and Δh_{stream}. Using these values, the protrusion height is calculated as $\Delta h = \Delta h_{span} - \Delta h_{stream}$. The protrusion heights were calculated using velocity profiles from 2D steady, laminar simulations, as prescribed by Luchini et al. [3]. To make the connection between protrusion height and the predicted viscous region, we have used Equation 4.5 from Bechert et al. [2]. As another validation, the predicted viscous region matches very well with the ZPG riblet cases.

$$DR\% = \frac{0.785(\Delta h/s)s^+}{(2c_f)^{-1/2} + 1.25} \tag{4.5}$$

In order to elucidate the physical reasons for drag reduction, we have conditionally averaged (again, coarsely resolved riblets were not considered) riblets in the spanwise direction. Here, conditionally averaging means spatially averaging flow fields on a *per riblet* basis. The result is a single flow-field within a riblet. Results were not averaged in the streamwise direction because the boundary layer is spatially developing. Unless otherwise mentioned, the coming figures use data sampled at $z/\theta_{in} = 275$. In the spanwise direction, profiles are either sampled at the riblet valley or the tip, as specified.

Figure 4.14 is a plot of the RMS of the streamwise velocity fluctuations, taken from the riblet valley. The riblet cases are defined in Table 4.3. Riblet width increases as the letters proceed alphabetically. From the plot, it is apparent that peak RMS value scales with riblet width, though all riblets have a peak less than the baseline ZPG flow. This is an important finding. Choi & Moin [13] originally compared a drag-reducing riblet with a drag-increasing riblet and found that the drag-increasing riblet had a greater peak value than the drag-reducing riblet (and the baseline). That could lead one to assume that the peak streamwise RMS fluctuations scale on $DR\%$, but Figure 4.14 clarifies the issue. Further comparison between the baseline and riblet profiles makes it obvious that fluctuations within the riblet valley are much lower than the baseline case.

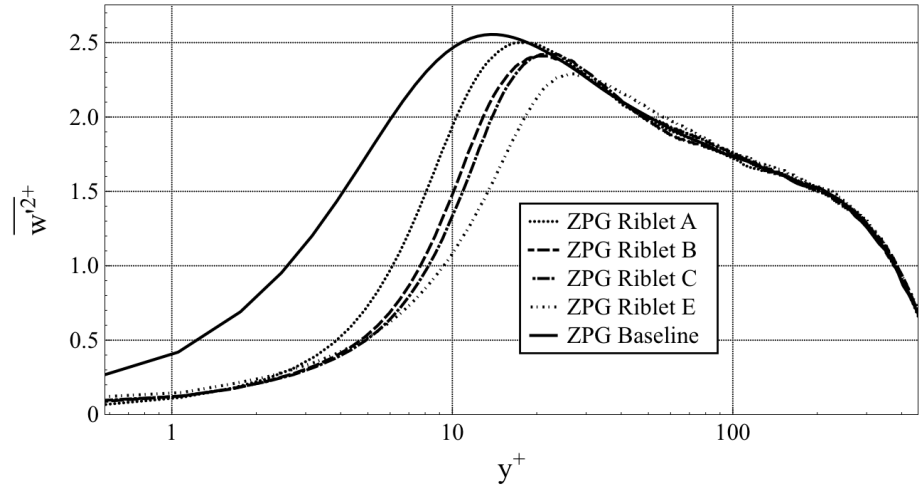

Figure 4.14: Mean conditionally-averaged streamwise fluctuations for the ZPG cases. In the spanwise location, the profiles are taken at the riblet peak.

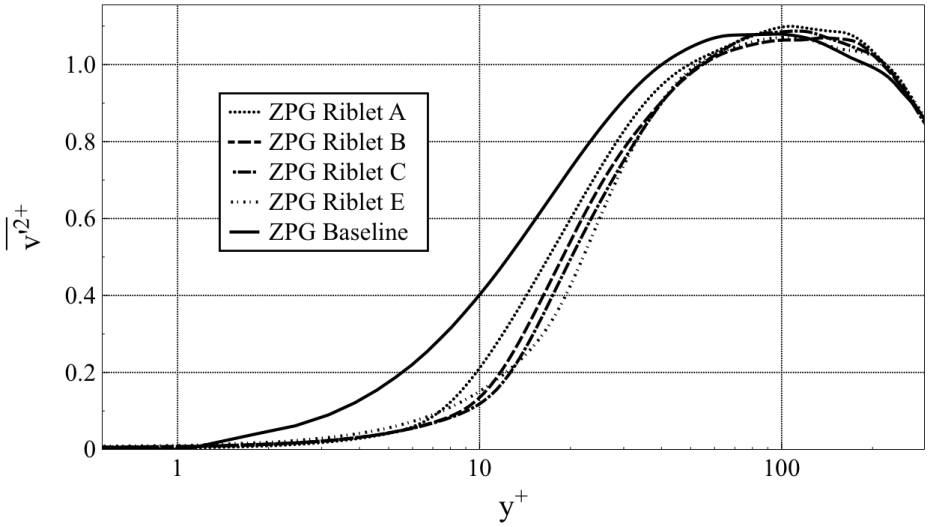

Figure 4.15: Mean conditionally-averaged wall-normal fluctuations for the ZPG cases. In the spanwise location, the profiles are taken at the riblet valley.

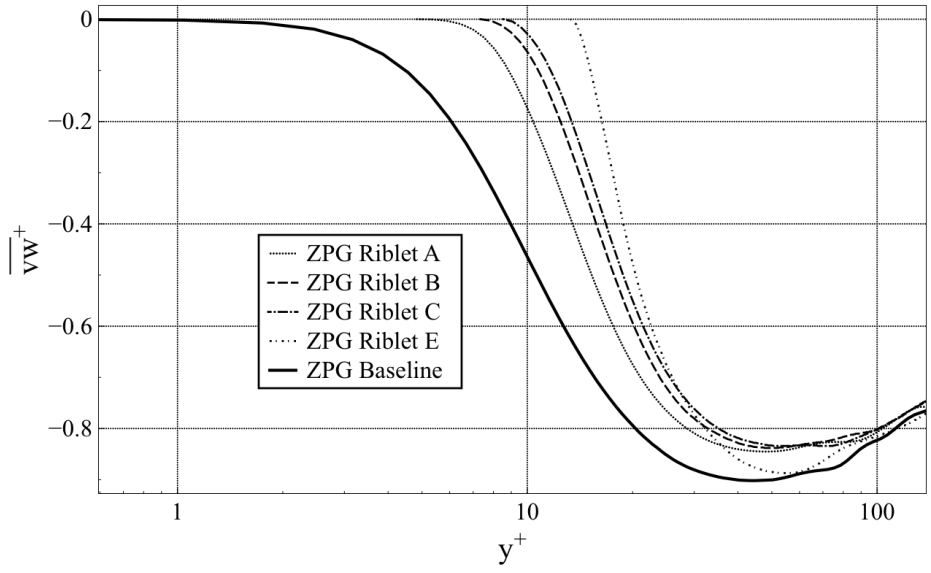

Figure 4.16: Mean spanwise-averaged primary Reynolds stresses for the ZPG cases.

Wall-normal fluctuations at the riblet valley are plotted in Figure 4.15. These fluctuations are insensitive to riblet width, and have their maximum near the baseline. Within the riblet valley, however, the fluctuations are significantly reduced. These results coincide with the findings of Choi & Moin [13]. Similarly, spanwise fluctuations (not shown) are insensitive to drag reduction and riblet width.

The primary Reynolds stresses for the riblets in ZPG are shown in Figure 4.16. The profiles plotted here are not conditionally averaged–they are spanwise averaged. Importantly, unlike the turbulence statistics previously mentioned, the maximum peak Reynolds stress is inversely proportional to drag reduction. The largest riblet, E, has the lowest drag reduction, and accordingly, it has the highest peak value. In any case each riblet does have a peak value less than or equal to the ZPG baseline case. In Choi & Moin [13], similar results were reported. There, the drag increasing riblet was accompanied by an increased (relative to the baseline) Reynolds stress and the drag reducing riblet with a decreased stress.

Turbulent Kinetic Energy (TKE) is shown in Figure 4.17. Profiles are plotted at the riblet valley. Each riblet significantly reduces the TKE when compared with the ZPG baseline flow. As with some other statistics, the TKE is insensitive to drag reduction and scales on riblet width. For normalization, these profiles use the shear velocity from the baseline case, $w_{\tau,0}$.

Figures 4.18 and 4.19 plot turbulence production at the valley and tip locations, respectively. In the valley, maximum production scales with riblet width, but near the riblet peak, production scales with drag reduction. Even though most turbulence fluctuations thus far are lower for larger riblets, increased wall-normal velocity gradients and higher primary Reynolds stresses for Riblet E cause a jump in turbulence production near the riblet tip.

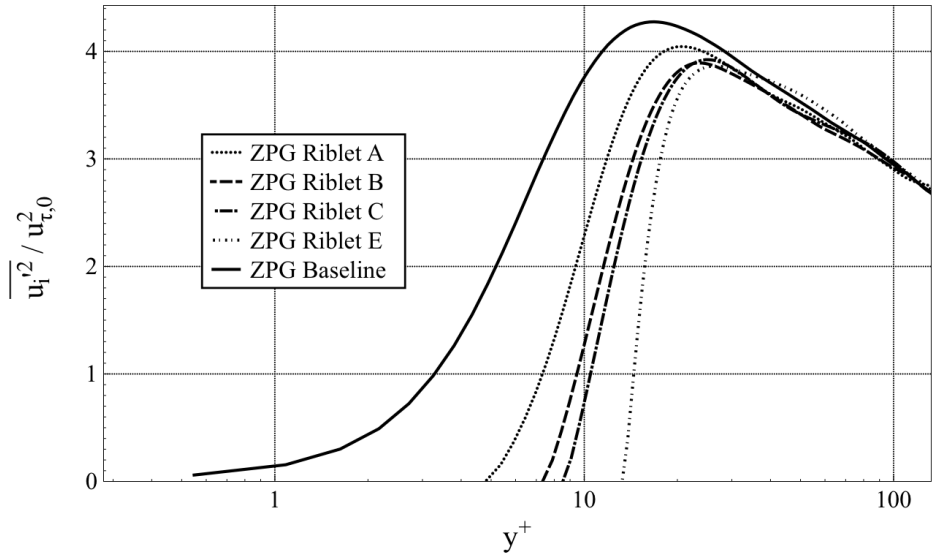

Figure 4.17: Spanwise-averaged normalized production of turbulence for the ZPG cases. In the spanwise location, the profiles are taken at the riblet tip.

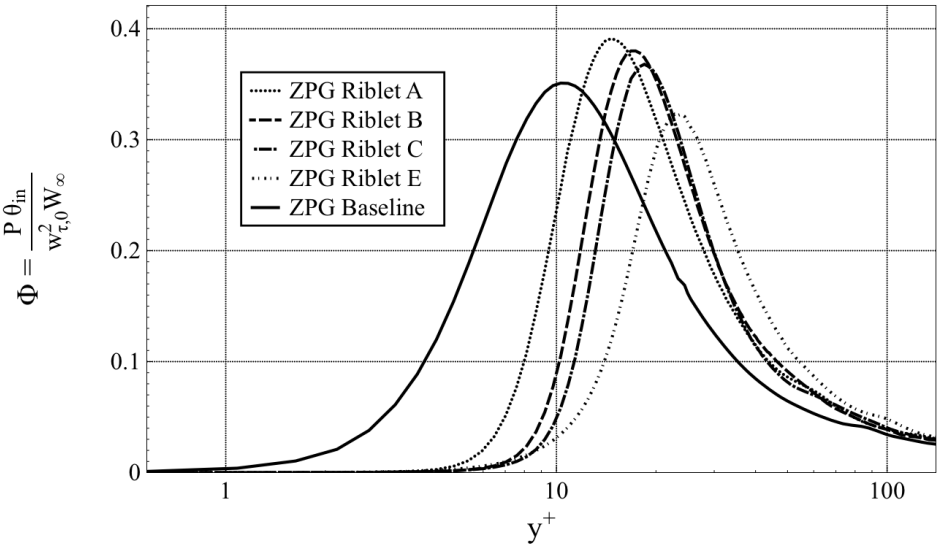

Figure 4.18: Spanwise-averaged normalized production of turbulence for the ZPG cases. In the spanwise location, the profiles are taken at the riblet valley.

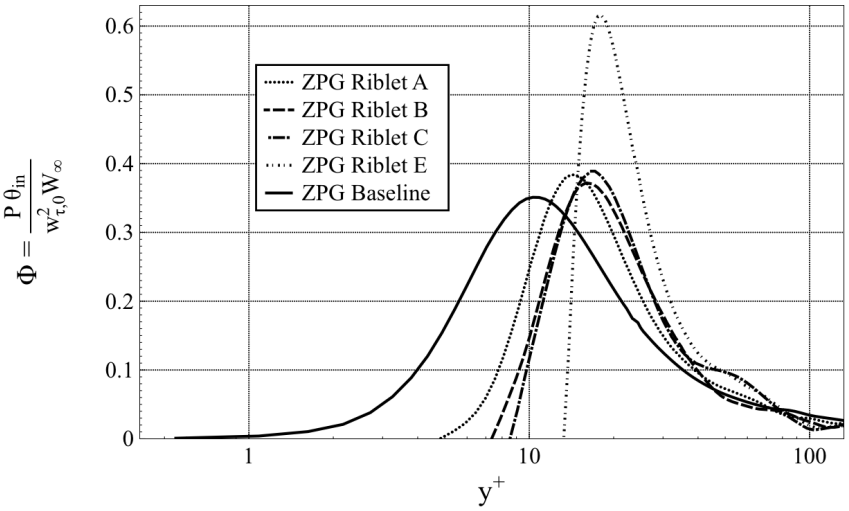

Figure 4.19: Spanwise-averaged normalized production of turbulence for the ZPG cases. In the spanwise location, the profiles are taken at the riblet valley.

4.3.3 APG Riblets

Figure 4.20 shows the drag reduction by riblets in APG and ZPG turbulent boundary layers. There is only a slight improvement in drag reduction for riblets in mild APG's.

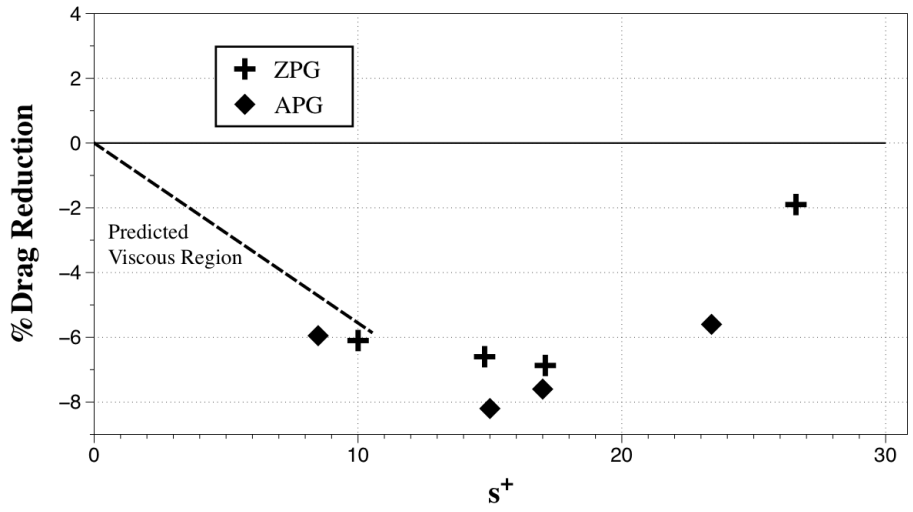

Figure 4.20: Drag reduction by riblets in APG flows compared with riblets in ZPG turbulent flow.

This result supports the experimental findings by Nieuwstadt & Debisschop [6] and disagrees with the computational results from Klumpp et al. [48]. To better visualize the comparison, Figure 4.21 shows the difference in drag reduction between riblets in APG and ZPG flows at various Clauser parameters. The present simulations agree within the uncertainty bars of the experimental data. Although Klumpp et al. [48] claim that their pronounced improvements in drag reduction follow the trend set by the experimental data, it is clear that they do not.

The present simulations show that riblets in an APG are still able to reduce skin-friction, which goes against the early experimental findings of Truong & Pulvin [46] and Squires & Savill [47]. As previously mentioned by Nieuwstadt et al. [5], the cause is likely due to the indirect method (momentum integral balance) of measuring drag reduction by these two researchers. In fact, the turbulent statistics shown in the coming figures prove that the methods of drag reduction are largely unchanged between riblets in ZPG and APG flows. Streamwise and wall-normal RMS fluctuations for the riblets in a mild APG

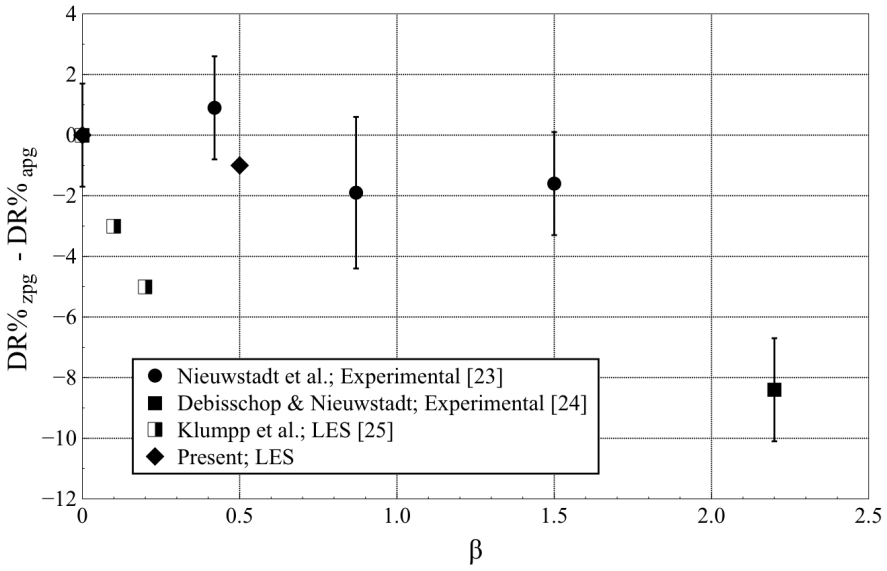

Figure 4.21: Difference in drag reduction between riblets in ZPG and APG flows are various Clauser paramenters. Uncertainty bars are those reported in their respective sources.

(not shown) are very similar to the riblets in ZPG, with maximum fluctuations scaling on riblet width.

Similar to riblets in ZPG flow, the primary Reynolds stresses shown in Figure 4.22, show that maximum values scale with drag reduction. There is however, one difference between the riblets in APG and ZPG. For riblets in APG, the locations of the maximum stresses are shifted *towards* the riblet surface. For riblets, this is the only turbulence statistic peak value that is not displaced away from the wall. The riblets here actually create a Reynolds stress profile similar to the riblets in ZPG (see Figure 4.16).

Lastly, Figure 4.23 plots normalized turbulence production at the riblet tips. This figure has been included to further show the correlation between riblet drag reduction and maximum production value. Riblet C for the ZPG case decreased drag by about 2% and had a production peak value about 50% greater than the ZPG baseline. The same geometry for the APG case decreased drag by 6% (this is due to differences in s^+, not to be confused with some other effect) and correspondingly, has a production peak value that is only 30% greater than the APG baseline.

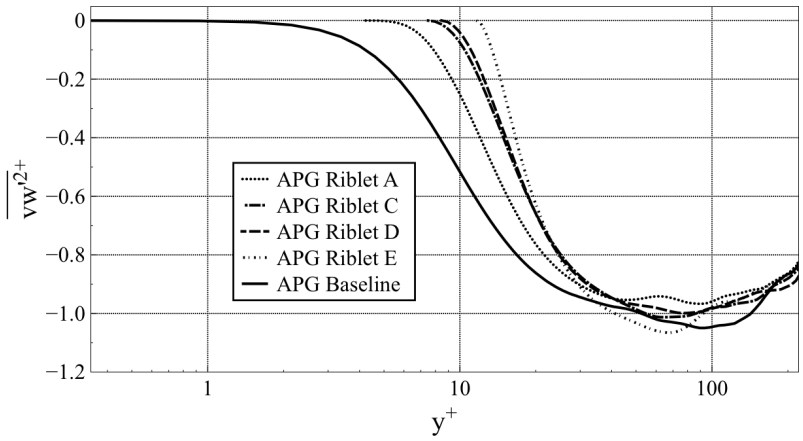

Figure 4.22: Spanwise-averaged Reynolds stresses for the APG cases compared with the baseline.

4.3.4 Riblet Induced Vorticity

It has been well established, both experimentally and computationally, that riblet films induce vorticity very near their surfaces. Near riblets, counter-rotating streamwise vortices are present in mean flow-fields. Figure 4.24 shows conditionally averaged contours of streamwise vorticity near Riblet B in a ZPG flow. Larger counter rotating vortex tubes can be seen that have characteristic diameters that are nearly half the riblet width. The contours also show regions of high vorticity very near the riblet surface. Note that the regions of vorticity on either side of the riblet tip have alternating directions.

Choi & Moin [13] reported that the circulation strength was greater for a drag increasing riblet than for one that reduced drag. This, like other turbulent statistics, could be interpreted as a correlation between drag reduction and vorticity magnitude. Fortunately, with a range of s^+, we are able to clarify this issue as well. Figure 4.25 is a plot showing the maximum value of streamwise vorticity for each riblet case as a function of normalized riblet width. This figure makes it clear that the strength of these vortex tubes is a function of riblet geometry, not drag reduction capability.

In Figure 4.26, we have plotted the coordinates of the locations where the maximum streamwise vorticity occurred for each riblet case. The horizontal and vertical axes' independent variables are defined as:

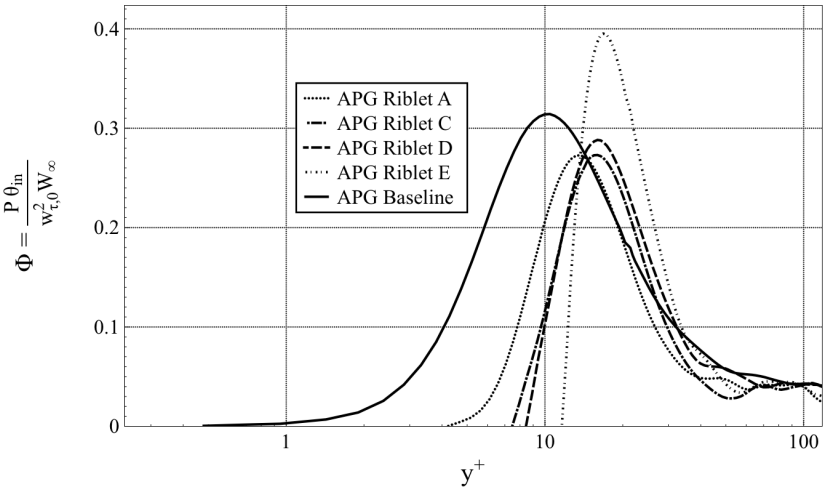

Figure 4.23: Conditionally averaged production for the APG cases. In the spanwise location, the profiles are taken at the riblet tip.

$$Y_\omega = \frac{y\Big|_{\omega_{max}} - h}{h}$$

$$X_\omega = \frac{x\Big|_{\omega_{max}} - s}{s}$$

Y_ω is the distance from the riblet tip, in the wall-normal direction, as a percentage of the total riblet height. X_ω is the distance from the riblet tip, in the spanwise direction, as a percentage of total riblet width. Therefore, in Figure 4.26, the location of maximum streamwise vorticity magnitude for Riblet A in the ZPG flow is about 14% of the riblet width away from the riblet tip and about 15% of the riblet height above the riblet tip. It's apparent that as the riblets increase in size, the centers of rotation for the induced vortex tubes tend to move away from the riblet surface.

4.3.5 Local Shear Comparisons

In this final section, we examine the local shear along a riblet surface, traversing from the riblet tip down towards the riblet valley. As with other profiles, the local shear values have been conditionally averaged in space and averaged in time. The streamwise location at

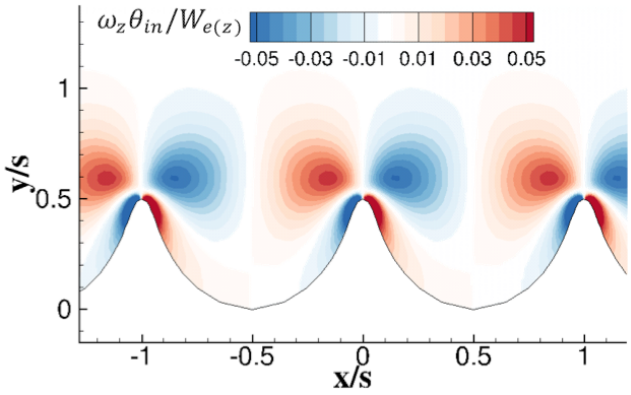

Figure 4.24: Mean conditionally-averaged streamwise vorticity for the ZPG cases. In the spanwise location, the profiles are taken at the riblet valley.

which the following data were sampled is $z/\theta_{in} = 275$. Figure 4.27 plots the local shear along the riblet in the spanwise direction for riblets in ZPG, where $x/s = 0$ corresponds to the riblet tip and $x/s = 0.5$ the riblet valley, as shown in the inset. Similar to riblets seen elsewhere in Choi & Moin [13], high shear stresses are limited to near the riblet tips. Although shear stresses are high in this region, the corresponding wetted surface area at the tips is low and a net reduction in skin-friction drag occurs. Among the different riblet cases, it is seen that as the riblet increases in size, the local shear becomes less smooth very near the riblet tip. This is due to the scalloped geometry and the resolution of the mesh. Although each riblet case had approximately the same number of grid points per riblet (33-39 points), the wider riblets had a higher concentration of points near the riblet tip. This is simply a consequence of larger riblets being easier to mesh. For example, Riblet E is nearly three times wider than Riblet A. More grid points near the tip more clearly resolve this plot of local shear. Figure 4.28 plots the local shear along the riblet in the spanwise direction for riblets in APG. Local shear values show similar trends to the riblets in ZPG.

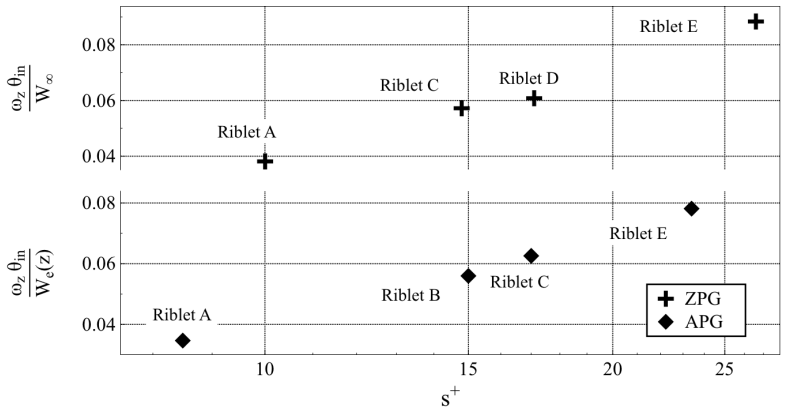

Figure 4.25: Maximum values of streamwise vorticity as a function of normalized riblet width.

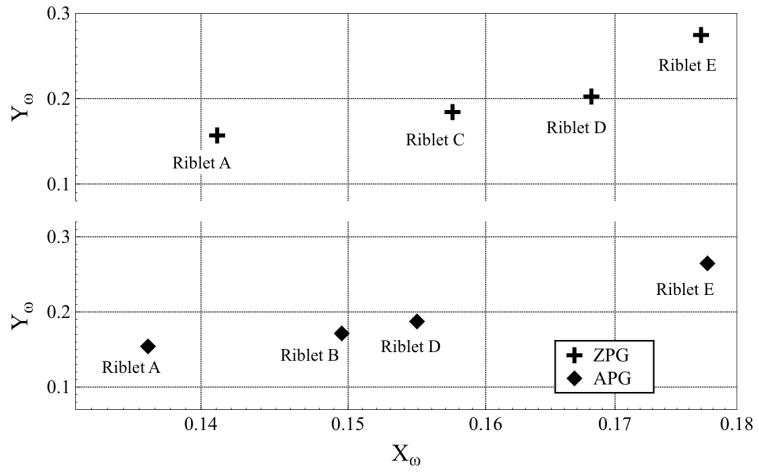

Figure 4.26: Locations of maximum streamwise vorticity as a function of riblet width and height as displaced from the riblet tip.

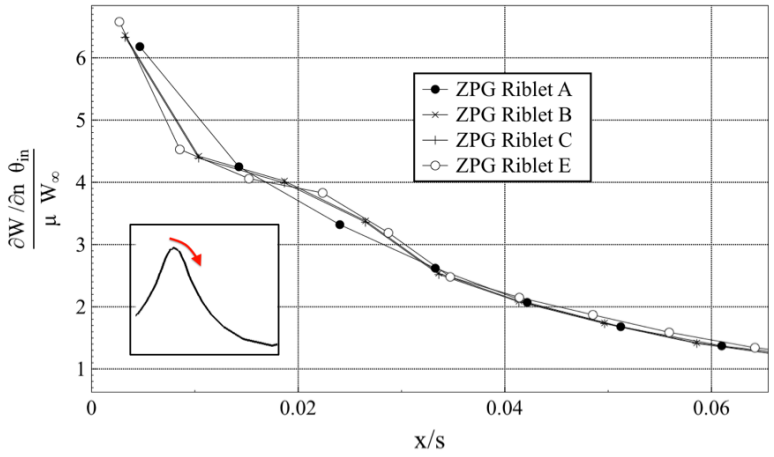

Figure 4.27: Local streamwise velocity gradients at the riblet surface for those in an ZPG flow, proceeding from the riblet tip ($x/s = 0$) to the riblet valley ($x/s = 0.5$).

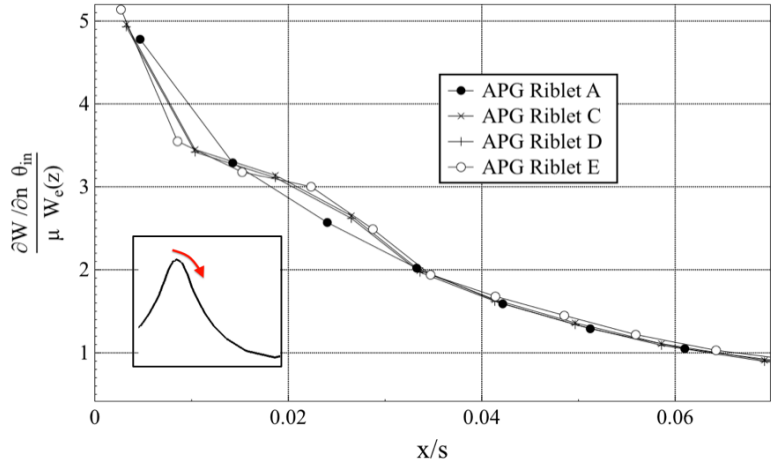

Figure 4.28: Local streamwise velocity gradients at the riblet surface for those in an APG flow, proceeding from the riblet tip ($x/s = 0$) to the riblet valley ($x/s = 0.5$).

Chapter 5

Static Sharkskin Denticles

This chapter presents results from sharkskin denticles modeled in a fully developed, turbulent open channel flow simulated with CURVIB. Mean flow fields and turbulence statistics are analyzed.

5.1 Domain Setup

Working in collaboration with George Lauder and Li Wen of Harvard, we were provided with the denticles seen in Figure 5.1. A representative denticle from *Isurus oxyrinchus* (shortfin Mako) was scanned using micro-CT to produce a detailed three-dimensional denticle shown in Figure 5.1a. The 3D model in Figure 5.1b is a symmetric (about the primary keel) version of the actual denticle produced by Wen & Lauder. The denticle was made symmetric about the spanwise direction so that it could be 3D printed, as detailed in their publication [10]. Since sharkskin is so geometrically complex, cavities among denticles are present, as is a membrane (the epidermis) to which they are affixed. As such, a structured body-fitted grid would be unable to capture these details, so the CURVIB method of Ge and Sotiropoulos [60] is employed in this work. To immerse the denticles into a background mesh, each denticle surface is discretized with a triangular unstructured mesh, as shown in Figure 5.2. The size of the unstructured mesh cells are similar in size to the background mesh cells in the computational domain.

We have conducted simulations for two different denticle arrangements shown in Figure

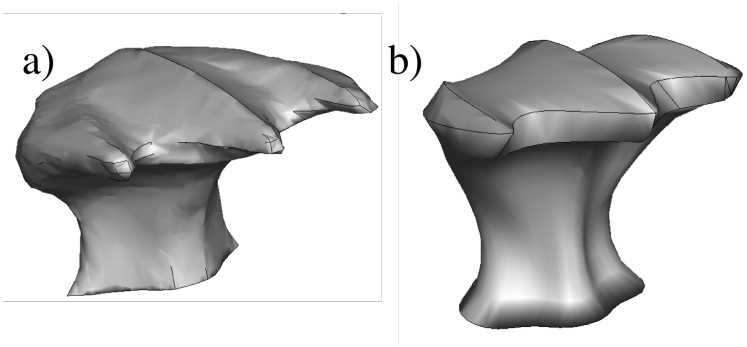

Figure 5.1: a) 3D model of an actual sharkskin denticle from a Mako shark. b) Modified denticle made symmetric about the primary keel.

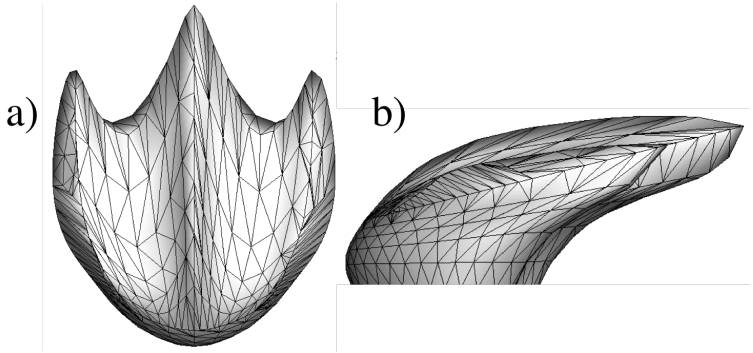

Figure 5.2: Representative denticle with triangular unstructured mesh surface. a) top view, b) side view.

5.4. Depending upon the location of the denticles on the shark body, denticles can be very tightly or loosely packed, as shown by Wen & Lauder [10]. The spacings chosen for this work mimic the arrangement seen in Figure 1.14 and is the same arrangement that was 3D printed by Wen & Lauder [10] (for the aligned case). This arrangement is also useful in identifying the effects of the denticle crown; as previously mentioned, Bechert et al. [51] was able to achieve drag reduction when denticles are interlocked and essentially two-dimensional. For both cases, a total of 324 individual denticles were used.

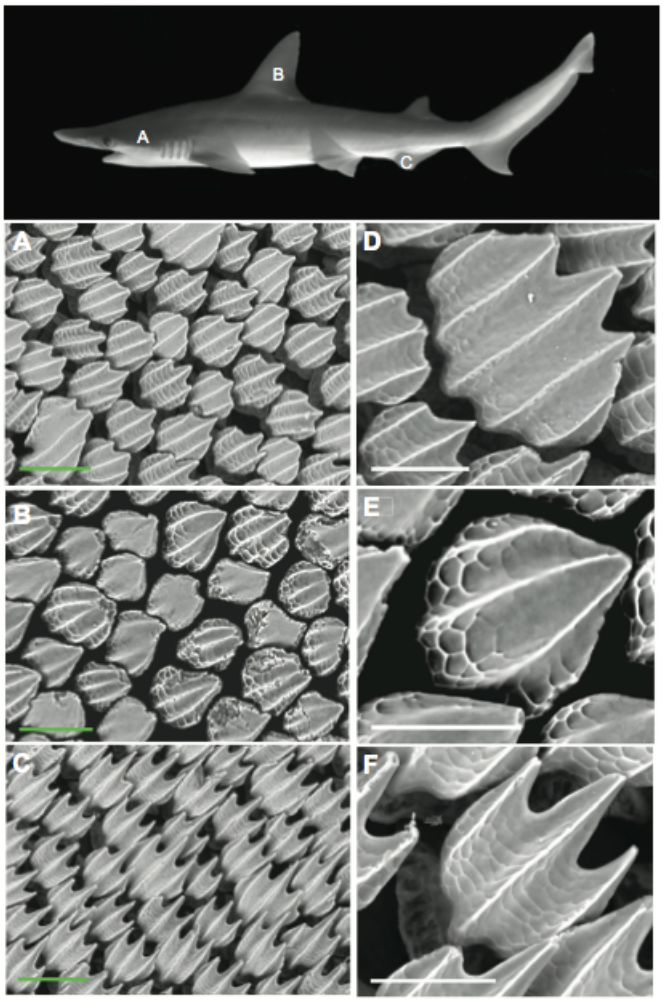

Figure 5.3: A Mako shark shown with varying denticle arrangements and sizes on various body locations. Figure from Wen & Lauder [10]. Letters A-C show corresponding body location and denticle arrangement. Letters D-F are enlarged views of images A-C.

Most research concerning riblets has been performed in turbulent channel flow, so to make a direct comparison, we have chosen to simulate the denticles in a similar fashion. Following the works of Choi et al. [13], Chu [36], and Garcia-Mayoral & Jimenez [28] we have created a rectangular domain with a structured grid and filled the bottom of the domain with denticles as shown in Figure 5.4.

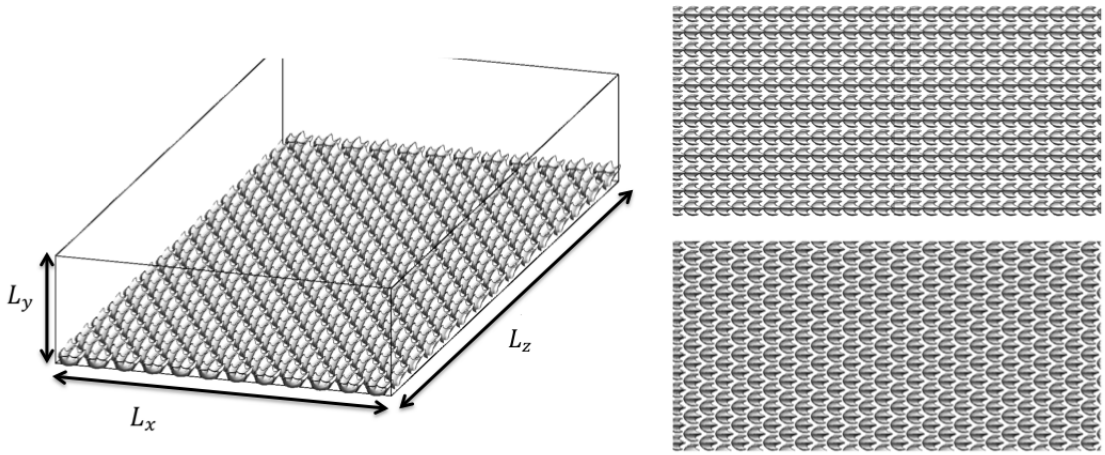

Figure 5.4: Compuational domain with staggered denticles.

Periodic boundary conditions are employed in the spanwise (x) and streamwise (z) directions (velocity components u, v, w correspond to directions x, y, z). The denticles are attached to a static, no-slip surface. A stress-free boundary condition is applied on the top of the domain. In the baseline and sharkskin cases, a constant mass-flux is maintained in the streamwise direction equal to $L_y \cdot L_x$. The baseline for this experiment is a similar domain without denticles. The Reynolds number is defined as $Re = \delta W_{bulk}/\nu$, where δ is the length of L_y, W_{bulk} is the integrated primary velocity, and ν is the kinematic viscosity. In the baseline simulation, $Re = 2,800$, which correlates to $Re_\tau \approx 180$. When denticles are included in the domain, the viscosity remains unchanged. Domain sizes and cell counts are detailed in Table 5.1–note that for every case, $L_y = 2$. For the baseline and sharkskin cases, the background grid is uniform in the spanwise and streamwise directions. A stretched grid is employed in the wall-normal direction. The resolutions for the various grids we employ are also reported in Table 5.1.

Figure 5.5 illustrates the *Isurus oxyrinchus* (shortfin Mako) denticle. The exact same

Table 5.1: Computational domain details for each sharkskin simulation. N_x, N_y, and N_z represent the number of grid nodes in each respective direction.

Case	L_x	L_z	$\Delta x^+_{min}, \Delta x^+_{max}$	$\Delta y^+_{min}, \Delta y^+_{max}$	Δz^+	$N_x \times N_y \times N_z$
baseline	$3.20L_y$	$6.40L_y$	3.0	0.27, 3.9	7.0	$190 \times 150 \times 166$
aligned	$2.96L_y$	$6.03L_y$	0.75	0.75, 3.3	0.75	$723 \times 123 \times 1466$
staggered	$2.96L_y$	$6.25L_y$	0.75	0.75, 3.3	0.75	$720 \times 123 \times 1521$
riblet	$3.04L_y$	$6.30L_y$	0.18, 1.5	0.24, 6.9	7.0	$1157 \times 104 \times 161$

denticle is used in the experimental work of Wen & Lauder [10]. The denticle width, $D_w = 2.4s$ and the height, $D_h = 1.37s$. The streamwise distance between denticles is $1.032D_w$ and the spanwise spacing is $1.142D_w$. For the staggered case, every other row is shifted half a denticle. In each case, the denticles have been scaled such that $s^+ \approx 16$–near optimal condition for scalloped riblets. This scaling was chosen to provide the denticles with the best chance of reducing viscous drag. Lastly, the angle of incidence is 13°.

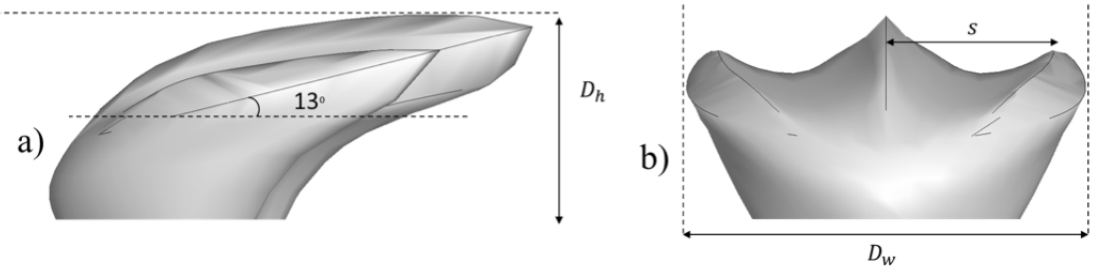

Figure 5.5: Representative denticle from Isurus oxyrinchus. a) YZ plane-view b) XY plane-view.

To make a direct comparison between riblets and sharkskin, we have also simulated scalloped riblets. The domain for the riblet simulation uses a body-fitted curvilinear grid and is shown in Figure 5.6 on the right. Again, L_y is the characteristic height (from the tips of the riblets to the top of the domain). The riblet case has the same Reynolds number as the sharkskin cases and uses the same baseline case to measure the drag reduction. The riblets have an $s^+ = 16$, an $h/s = 0.5$, and a thickness to width ratio, $t_{95}/s = 0.06$, where t_{95} is defined as the riblet thickness at 95% of the height, h. The riblet computational domain had the same boundary conditions as the denticle simulations.

In order to resolve each denticle with the CURVIB method, a very fine grid is required.

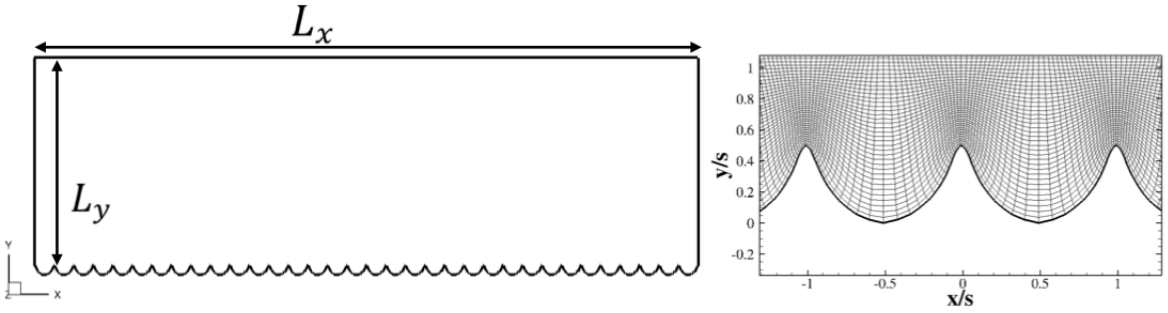

Figure 5.6: Right: computational domain with scalloped riblets. Left: the body-fitted mesh for the scalloped riblet.

Therefore, the background grid is sufficiently fine to ensure that each denticle is locally immersed within a grid resolution with 50 grid points along each spatial direction. To make certain that the background mesh was fine enough to accurately calculate the force on each denticle (as described in Section 2.3), a grid independence study was conducted by doubling the number of grid points in all three directions simultaneously. Due to the large cell counts of the domains, we considered three resolutions (25^3, 50^3, and 100^3 grid cells) around a single denticle surrounded by a bed of coarser resolved denticles in a turbulent channel flow at $Re_\tau = 180$. We found that the resultant force on the highly resolved denticle at 50^3 and 100^3 resolutions varied by just 2%. Based on this study we determined that the 50^3 resolution per denticle is adequate to obtain grid independent solutions. Figure 5.7 shows instantaneous and average values of the coefficient of friction, C_f as measure on the test denticle. The faint lines are instantaneous and the bolder lines are time averaged.

Another set of numerical sensitivity studies was carried out to determine the overall size of the computational domain. Following the approach of Kim et al. [12], we sampled velocities from the baseline case and calculated the two-point correlations, R_{ii}, defined in Equation 5.1, where u_i' denotes the fluctuating velocity in the i^{th} direction ($i...1, 2, 3$).

$$R_{ii} = \frac{\overline{u_i'(\mathbf{x}, t) u_i'(\mathbf{x} + r, t)}}{\overline{u_i'^2}} \tag{5.1}$$

Figures 5.8 and 5.9 show that the fluctuating velocities are uncorrelated (i.e., $R_{ii} = 0$) at the boundaries of the computational domain. Figure 5.8 plots R_{ii} in the spanwise direction, both near the wall ($y^+ = 9$) and in the logarithmic region of the boundary layer

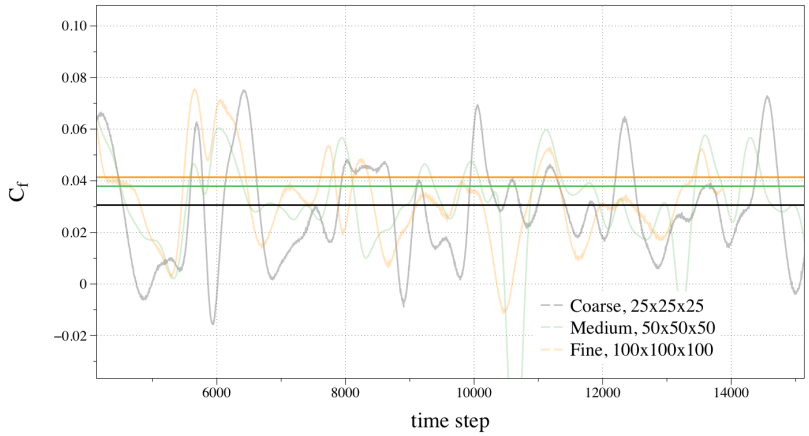

Figure 5.7: Time-variation of coefficient of friction on a bed of denticles for the grid independence study. Faint lines are instantaneous, whereas the bolder lines are time-averaged.

($y^+ = 115$). Figure 5.9 shows two-point correlations in the streamwise directions.

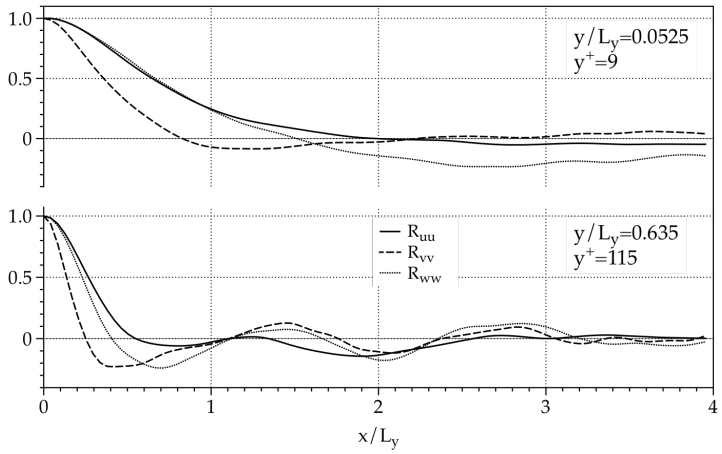

Figure 5.8: Two-point correlation in spanwise direction at two separate vertical locations.

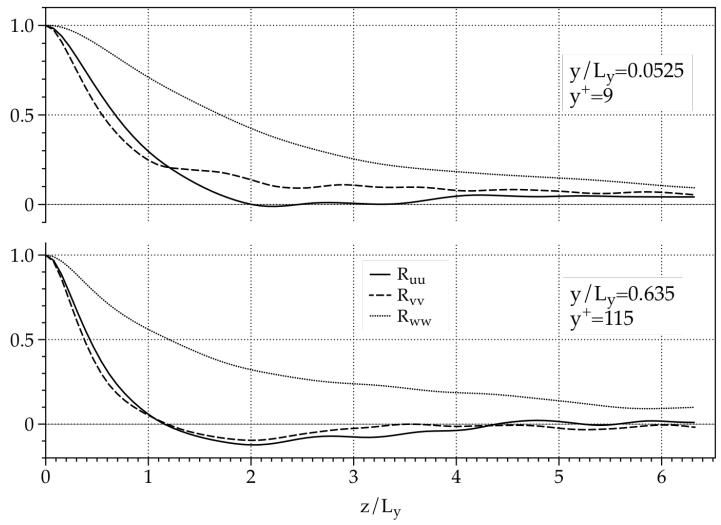

Figure 5.9: Two-point correlation in streamwise direction at two separate verticle locations.

5.2 Results & Discussion

5.2.1 Global drag measurements.

There are two types of drag created by the denticles: viscous drag and form drag. The form drag is due to pressure differences upstream and downstream of the denticle. The viscous drag is due to the velocity gradient very near the denticle. There is an additional viscous drag due to the membrane to which the denticles are affixed. Therefore, the total drag in the staggered and aligned cases, F_{total}, is

$$F_{total} = F_m + F_p + F_v$$

where F_p is the pressure drag, F_v is the viscous drag, and F_m is the membrane drag. The baseline and riblet cases incur only viscous drag. Figure 5.10 is a plot that shows the ratio between total drag with and without sharkskin (and with/without riblets). For comparison, we have included experimental data from Bechert et al. [16]. In Figure 5.10, the open symbols (and their curve fits) correspond to the experimental sharkskin data at two different values of AOI, 5° and 10°. First, notice that the sharkskin denticles for both staggered and aligned arrangements increase total drag by 45-50%. These results match

very well with the experimental data at $s^+ = 16$, especially considering that the present denticles have an AOI of 13°. Our simulations support the trend that as the AOI increases, so does drag augmentation by sharkskin. In sharp contrast, the scalloped riblets reduce drag in comparison with the baseline. Here too, excellent agreement with the experimental data is achieved, with a drag reduction of 5.2%. It is clear that in both arrangements, sharkskin does not reduce skin friction like riblets, even if the keels are sized at a near optimal value of s^+. Also, note that the staggered case increases drag more than the aligned case, which will be discussed in more detail in the upcoming results.

Table 5.2 shows the calculated contributions of the various components of drag to the total drag for the two denticle cases. For both cases, the contribution of the membrane drag is negligible and can be ignored. Viscous drag is the primary contributor to total drag accounting for approximately 75% of the drag force. A significant contribution to the drag also arises from pressure, which suggests the presence of separated flow among the denticles. The physical reasons for these relative contributions of pressure and form drag will be discussed later in this paper when we will present the three-dimensional structure of the flow in the vicinity of the denticles.

Table 5.2: Calculated percentage of total drag for the two simulated denticle cases.

Case	F_p	F_v	F_m	F_{total}
aligned	23.5%	76.2%	0.3%	100%
staggered	26.35%	73.5%	0.15%	100%

5.2.2 Mean streamwise velocities & turbulence statistics.

In this section, we present figures of mean streamwise velocities and turbulence statistics for sharkskin and riblet cases. For the sharkskin profiles, we have not preserved spanwise or streamwise variations in these profiles because we have spatially averaged over the lengths, L_z and L_x. For the riblet case however, we have conditionally averaged the flow in the spanwise direction (i.e., the flow is averaged on a per-riblet basis) and also averaged over L_z. In the spanwise direction, riblet profiles are taken at the riblet tip. The mean streamwise velocities have been normalized with a case-specific shear velocity, w^*_τ, which is defined as

$$w^*_\tau = F_D/A_{fp}$$

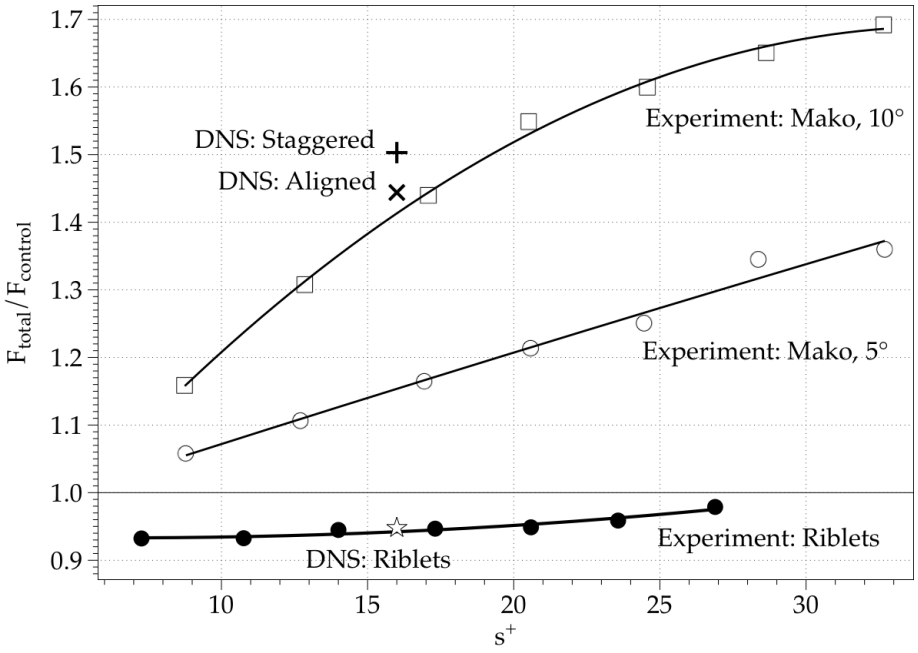

Figure 5.10: Ratio between total drag with and without sharkskin (and with/without riblets) from the present DNS. Fitted curves, open squares/circles, and filled circles are experimental data from Bechert et al. [16]. The + and × mark our DNS data for the staggered and aligned denticle cases, respectively. The open star is the present DNS result for the riblets.

where F_D is the total drag force for each case and A_{fp} is a flat-plate area for each case (i.e., surface area without denticles or riblets). This choice of shear velocity shows the effect of roughness in the logarithmic region. For the turbulence statistics, we have normalized fluctuating velocities with $w_{\tau,0}$, the baseline shear velocity to make direct comparisons among the cases. The subsequently presented figures are wall-normal plots, thus for the riblet case, profiles originate at the riblet tip ($y^+ = 8$). Denticle profiles originate at the epidermis ($y^+ = 0$).

Figure 5.11 shows mean streamwise velocity profiles plotted in wall-coordinates. Obviously, both denticles and riblets greatly alter the turbulent boundary layer and near their surfaces, act as a momentum-sink by slowing the flow. The denticles create two different slopes, or a double logarithmic region. The riblet seems to show a similar feature, however

if the profile is sampled at the valley spanwise location, two separate slopes are not seen.

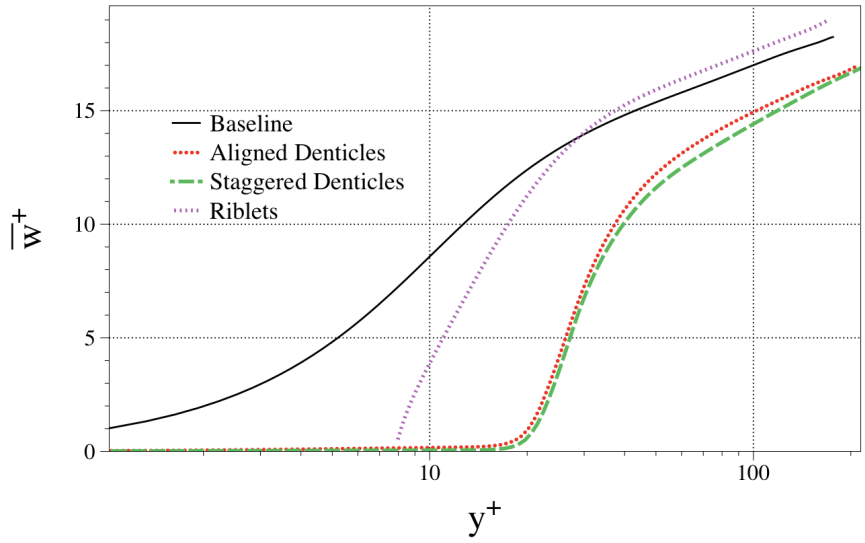

Figure 5.11: Mean streamwise velocity normalized with w_τ^*.

Normalized streamwise fluctuations have been plotted in Figure 5.12. This figure illustrates that each sharkskin case creates a drastic increase in streamwise fluctuations. Such behavior is the exact opposite of what is seen for the scalloped riblets, which cause a considerable reduction in the streamwise turbulence intensity as compared to the baseline case. Physically, increased statistics imply increased turbulent mixing and more efficient transport of high-speed outer fluid toward the wall, which, as shown in Figure 5.10, coincides with increased skin-friction. Similar trends are also observed in Figure 5.12, which shows the primary Reynolds shear stress profiles for the various cases. Riblets lead to a reduction in Reynolds shear stresses, but for arrangements of denticles, the maximum stress is greatly increased implying increased turbulent mixing consistent with the drag increasing action of denticles.

5.2.3 Three dimensional mean flow fields.

In order to determine why the two sharkskin arrangements increase drag, time-averaged velocity fields are conditionally averaged in the streamwise and spanwise directions. Conditional averaging is implemented herein by averaging over a patch of denticles, which

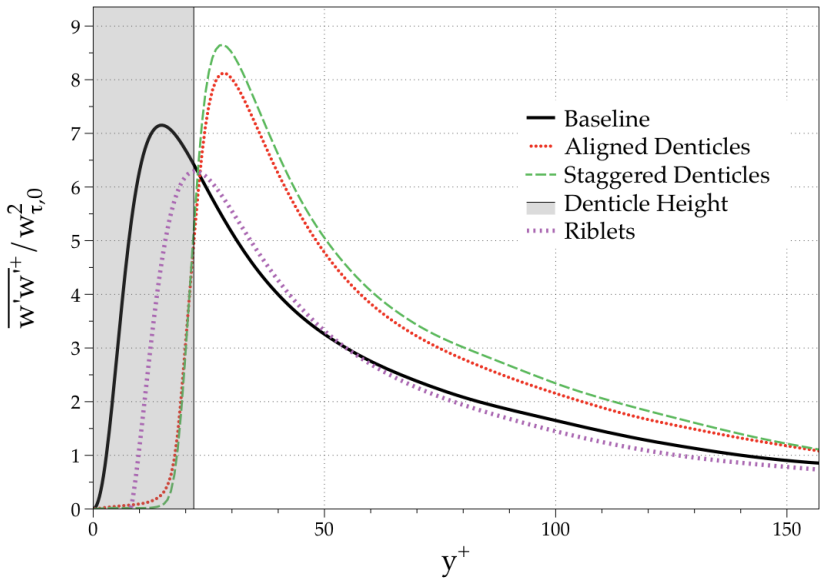

Figure 5.12: Streamwise Reynolds stress. Riblet profile taken at the tip. The greyed portion signifies the height of the denticles.

is specific to each arrangement. The patch we employ for each case is shown in Figure 5.14. This figure shows mean shear velocity on the membrane with corresponding limiting streamlines. For the aligned denticles, a line of convergence forms at the crown of each denticle suggesting three-dimensional separation and vortex formation. For the staggered case, on the other hand, a saddle node forms upstream of each denticle and the associated pattern of limiting streamlines resembles that of a horseshoe vortex (see Paik et al. [72]). Two stagnation points exist for the aligned case though, one on either side of each denticle. For this case, the overall patterns of the limiting streamlines further suggest that much of the flow is channeled between columns of denticles giving rise to streaks of high shear velocities. In the staggered case, this channeling cannot occur because flow stagnates at the crown of the next denticle. In contrast, for the aligned case each denticle is in the wake of another, which causes separation at the crowns. Lastly, the aligned case shows a small region of reverse-flow, which, however, is apparently not enough to cause any type of drag reduction. Staggered denticles incur no mean recirculation anywhere on the membrane.

Figure 5.15 plots contours of mean streamwise velocity at the transverse plane that

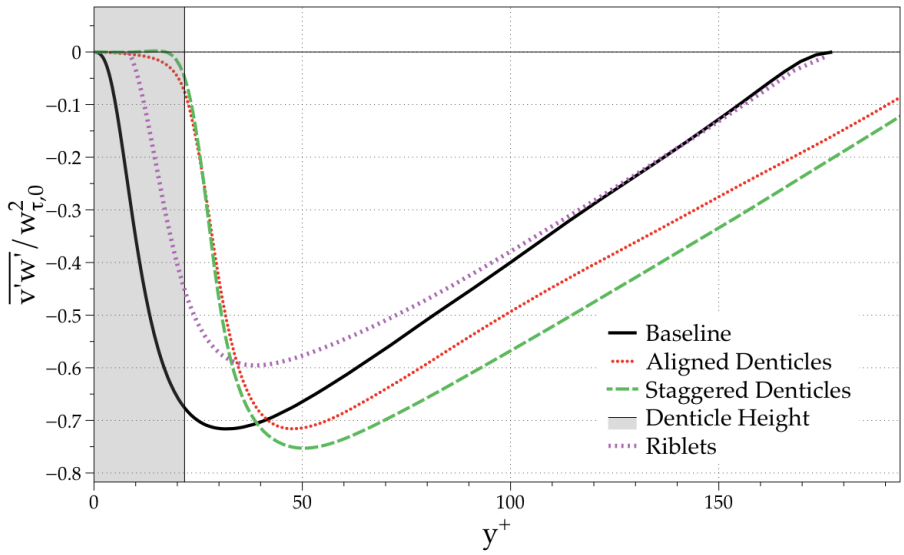

Figure 5.13: Primary Reynolds stress. Riblet profile taken at the tip.

bisects a denticle for the aligned and staggered cases. The primary difference between the two cases is the increased velocities at the outer keels for the aligned (left side) arrangement. This too is evidence of flow channeling between denticle columns. Later in this section we will show that flow channeling increases skin-friction on the outer keels of the denticles. In contrast, the staggered case shows no signs of channeling.

The limiting streamline plots suggest three-dimensional separation and vortex formation around the denticle. To further elucidate the structure of the so-induced secondary flow, we plot in Figure 5.16 averaged non-dimensional vertical velocity contours for the aligned denticle case. This figure reveals a number of interesting trends and highlights the three-dimensional structure of the flow. We note in this figure the strong positive vertical velocity near the crowns, a region of equally strong negative vertical velocity near the outer keels, and a pocket of positive vertical velocity at the ridge of the primary keel. These patterns in the vertical velocity field are suggestive of the presence of counter-rotating streamwise vortices in the mean flow. This feature of the flow is confirmed in Figure 5.17 where we show iso-surfaces of normalized mean streamwise vorticity.

The presence of coherent, counter-rotating vortices is clearly evident in this figure. Furthermore, the figure also reveals that the formation of the vortex tubes is the result of

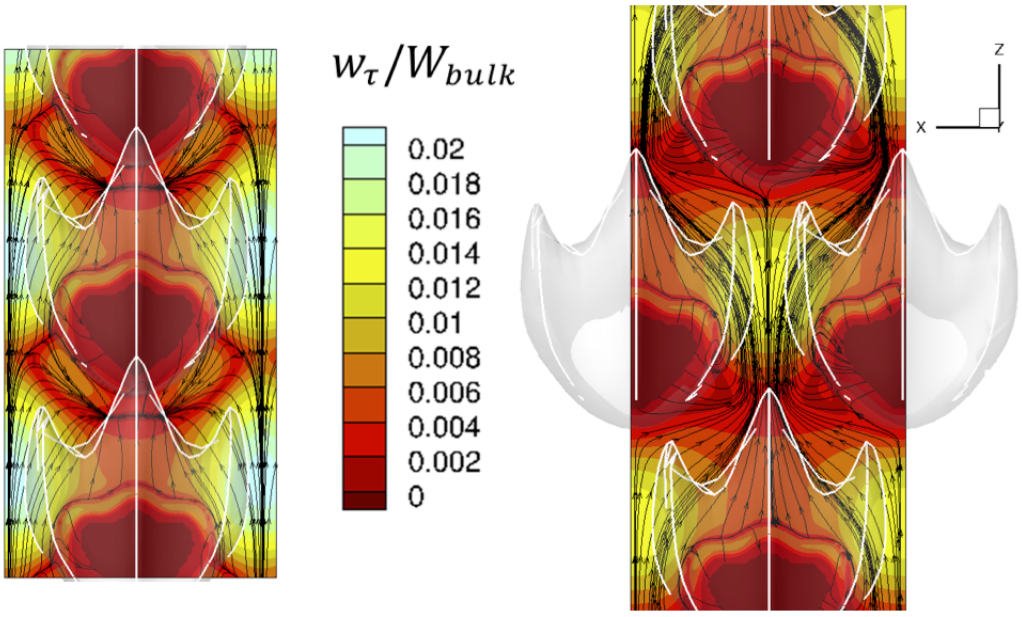

Figure 5.14: Limiting streamlines and contours of conditionally averaged shear velocities on the membrane for the aligned case (left) and the staggered case (right).

three-dimensional flow separation at the tip of each keel. The interaction of the primary counter-rotating vortices with the surface of the denticles causing the extraction of wall vorticity of opposite sign is also evident from this figure. Finally, we also note the large region of vorticity on the undersides of the denticles. The so resulting complex three-dimensional flow appears to be the main culprit for increasing the mean shear on the denticles.

It is important to note, however, that riblets also induce coherent counter-rotating streamwise vortices but in stark contrast with denticles, reduce drag. To quantify the differences between the two cases, we plot streamwise vorticity contours at a transverse plane in Figure 5.18 for the riblet and aligned sharkskin cases. As seen in this figure, for both the riblet and denticle cases the magnitude and direction of the counter-rotating vortices are similar, but there is one major difference. Namely, for the drag-reducing riblets the valley between riblets exhibits very low velocity gradients and consequently low shear stress. This is important because Lee & Lee [4] showed that as s^+ increases, the center

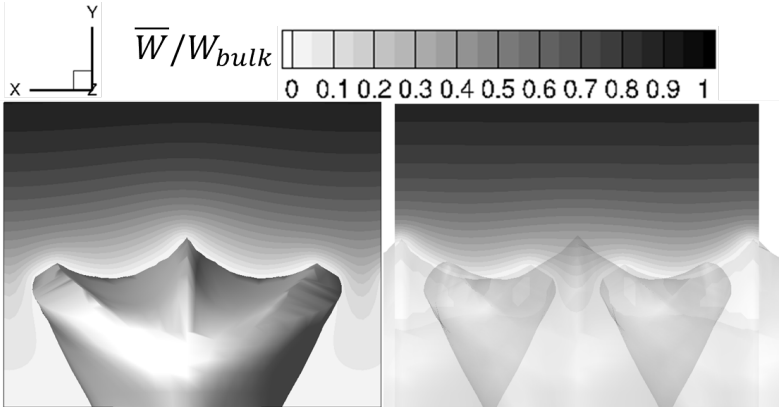

Figure 5.15: Mean streamwise velocity at a transverse plane that bisects the denticle for the aligned case (left) and the staggered case (right).

points of the streamwise vortices migrate laterally downward into the valley of the riblet, eventually destroying any drag-reducing property. Essentially, this also appears to be the case for the aligned denticles. That is, the valley between the keels of the denticles is not free from vorticity, causing a drag increase rather than reduction. This trend should be attributed to the geometry of the outer keels of the denticles, which are rounded and much shorter than the primary ridge.

Streamwise vorticity contours are also plotted for the staggered denticle arrangement in Figure 5.19. As seen in this figure, the vorticity field is quite complicated for the staggered case as the vorticity field alternates in a periodic manner in the streamwise direction between positive and negative. To help visualize this complex structure, we also include in Figure 5.19 vorticity contours on a wall-normal, streamwise plane. It is evident from this figure that a region of negative vorticity originates at the furthest upstream denticle at the crown and continues at the angle of incidence atop a region of positive vorticity created by the crown of the next downstream denticle. It is clear, therefore, that the staggered denticle arrangement creates alternating vorticity that two-dimensional riblets can never induce.

The three-dimensional and alternating structure of the resulting streamwise vorticity field for the staggered case, is shown in Figure 5.20 where we plot positive and negative

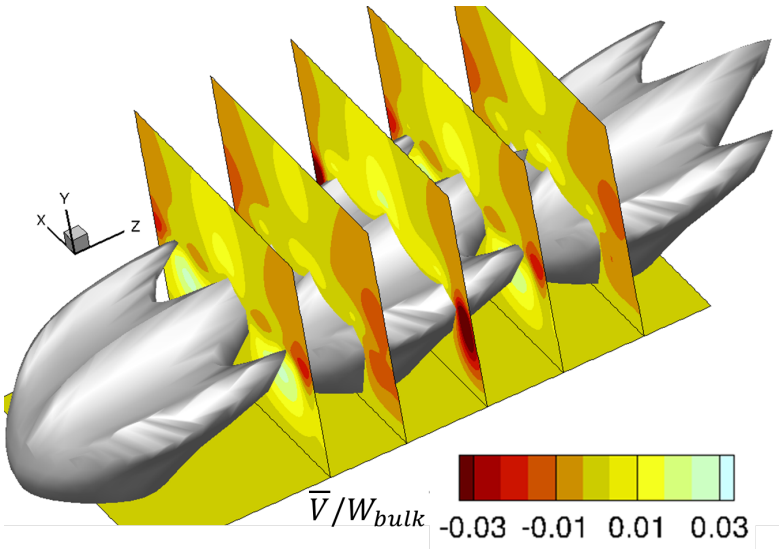

Figure 5.16: Mean vertical velocity at several streamwise planes for the aligned denticle arrangement.

iso-surfaces of mean vorticity. The resulting structure of the vortices is drastically different than that of the aligned denticles. Individual vortex tubes are not sustained in the streamwise direction, but instead extend for about the size of a denticle. Also, notice that the vortex tubes in this case trend away from the primary keel.

The alternating pattern seen in Figure 5.20 can be further explained by examining the force components on the denticles. Figure 5.21 shows contours of the transverse force, F_x, projected onto the denticles for each arrangement, calculated as was described in Section 2.3. The resulting stresses from each denticle were then averaged over all denticles to result in one representative denticle for each case.

In Figure 5.21, we observe that for the staggered denticle arrangement, the flow is forced away from the primary (center) keel, but for the aligned arrangement, just the opposite occurs–the flow tends toward the primary keel. Thus, while in the aligned case, mean counter-rotating vortices are sustained by the denticles, the staggered arrangement locally changes the direction of the flow at every row of denticles, which prevents sustained counter-rotation. Limiting streamlines plotted on the aligned denticles in Figure 5.22 highlight a node of reattachment near the outer keels, forcing fluid toward the primary keel. For the

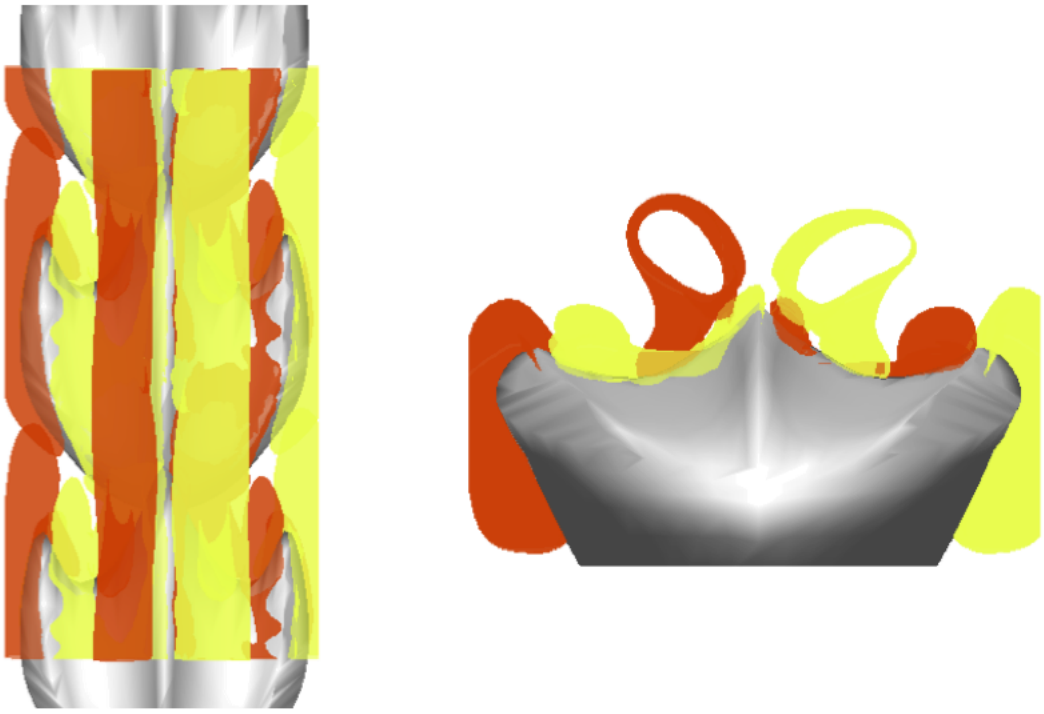

Figure 5.17: Iso-surfaces of positive (yellow) and negative (orange) mean streamwise vorticity for the aligned arrangement.

staggered case, the stagnation point at the primary keel forces fluid toward the outer keels. Another critical physical insight from the limiting streamlines is that there is secondary flow on the outer keels. The three-dimensionality of the sharkskin seems to be an inherent disadvantage from a drag-reducing point of view. Drag reduction by riblets is achieved by creating a laminar-like flow velocity gradient on as much wetted area as possible. In both denticle arrangements, however, three-dimensional separation, vortex formation and strong secondary flow are generated on much of the wetted surface, even in the valleys (between keels), causing a significant augmentation of skin friction drag.

The consequence of such secondary flow is evident from plots of mean shear stress magnitude contours shown in Figure 5.23 for denticles and riblets. Note that Choi [13] used DNS to show differences in flow fields between drag-reducing and drag-augmenting riblets. One fundamental difference between those two riblets was that the drag-reducing

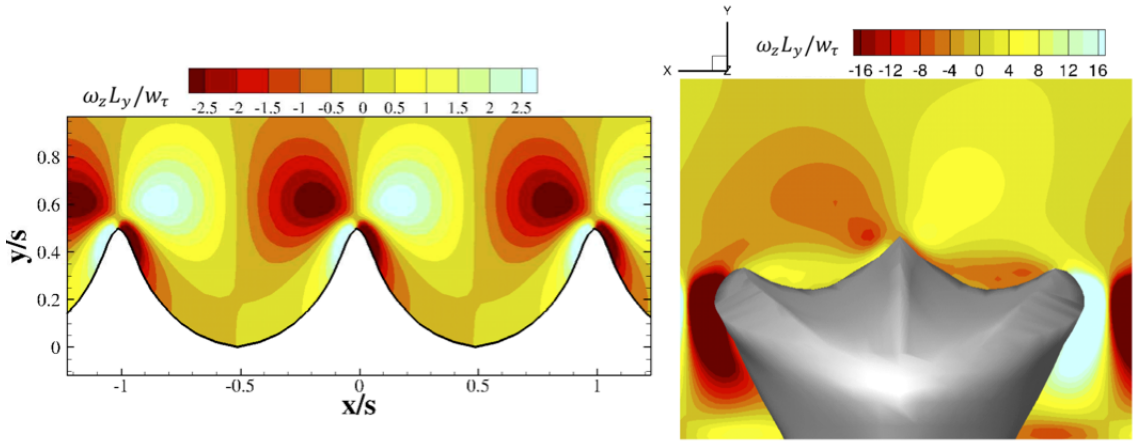

Figure 5.18: Front view of mean streamwise vorticity for the scalloped riblets (left) and aligned denticle arrangement (right).

riblet was able to consolidate high shear stress near the riblet peaks. Indeed, our riblet simulation shows a similar result. The riblet tips experience a local shear stress about four times that of the baseline, but the riblet valleys have a much lower value of about half as much as the baseline. It is obvious from the shear stress contours on the denticles that both sharkskin arrangements are unable to consolidate high shear in narrow bands, as between keels, the stress is about equal to the baseline. Lastly, it is evident from Figure 5.24 that for both denticle cases, regions of high shear stress are also seen on the sides and undersides of the outer keels. The three-dimensionality of the denticle adds a surface area that is exposed to high shear in ways two-dimensional riblets would not.

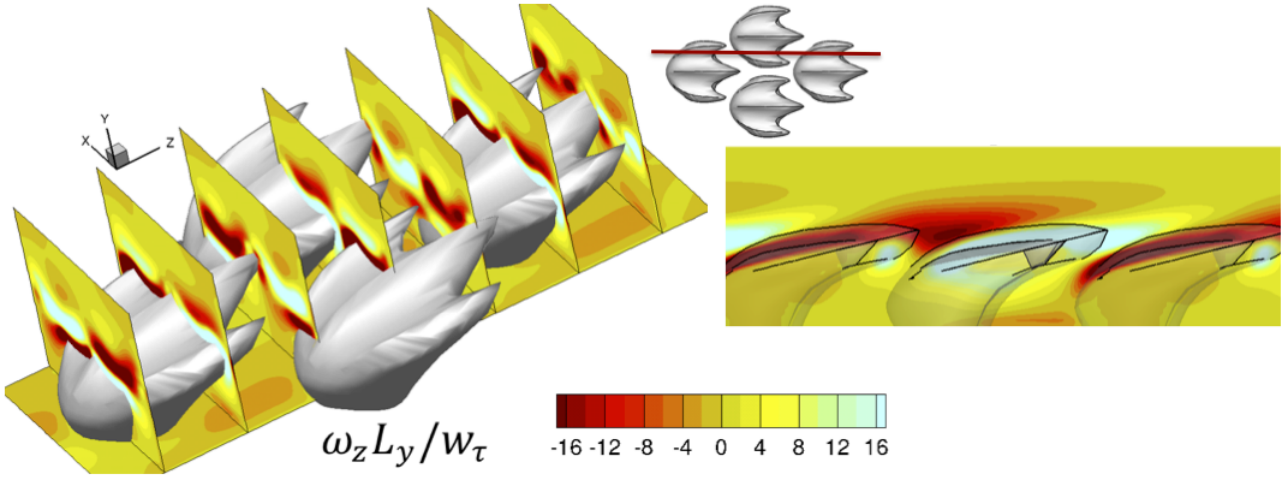

Figure 5.19: Isometric (left) and side (right) views of mean streamwise vorticity for the staggered arrangement. Inset shows the spanwise location of side view.

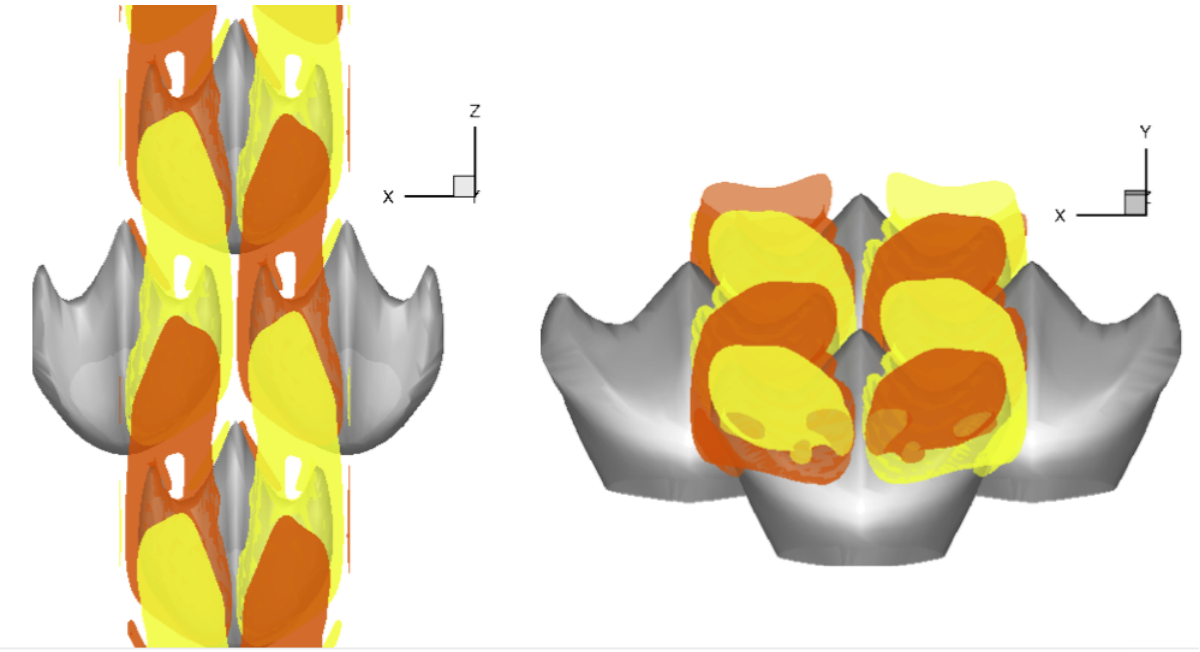

Figure 5.20: Iso-surfaces of positive (yellow) and negative (orange) mean streamwise vorticity for the staggered arrangement.

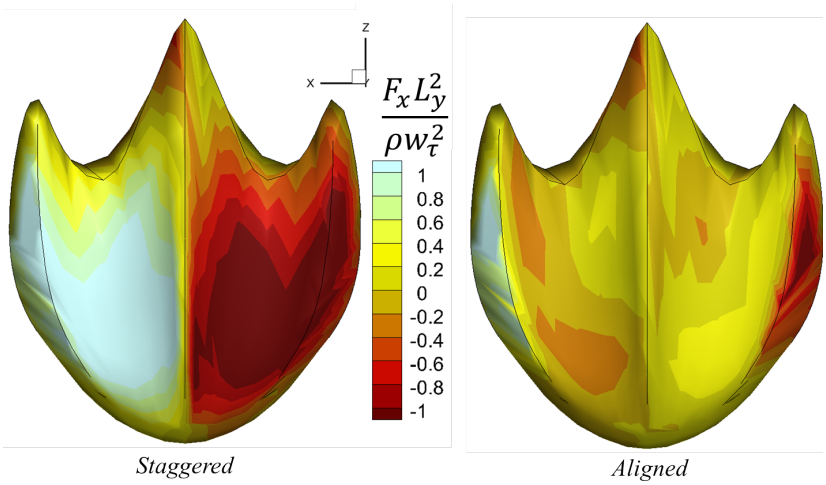

Figure 5.21: Normalized spanwise force on a representative denticle (results averaged over all denticles) from the staggered (left) and aligned (right) cases.

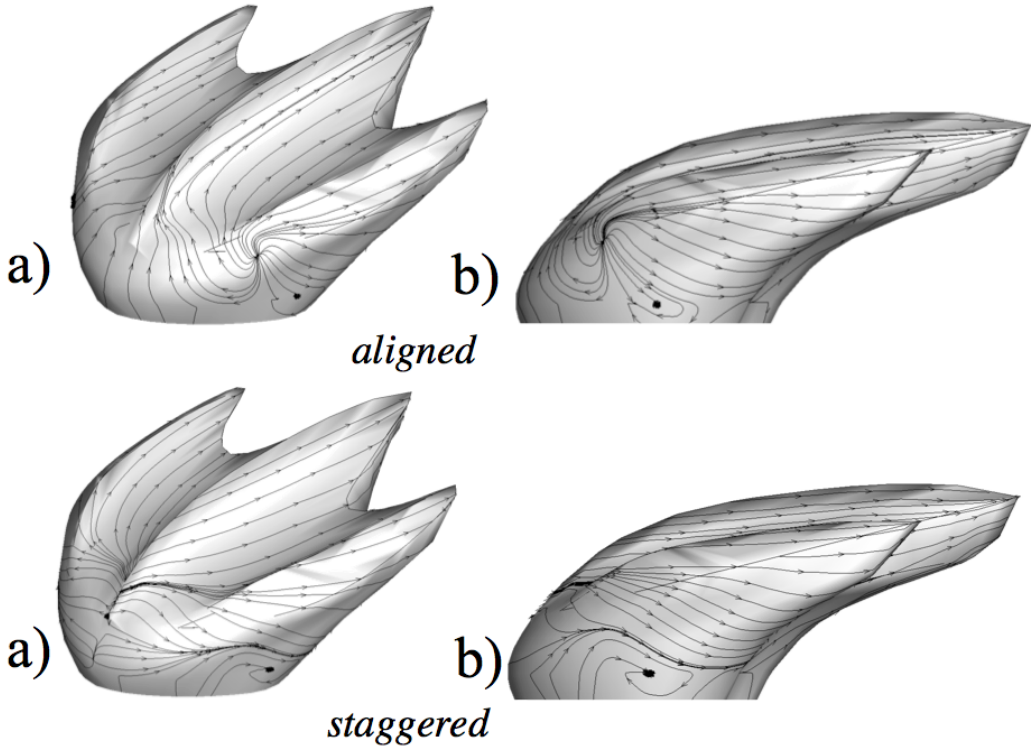

Figure 5.22: Mean limiting streamlines on a single denticle from the aligned (left) and staggered (right) cases. a) Isometric view. b) side view.

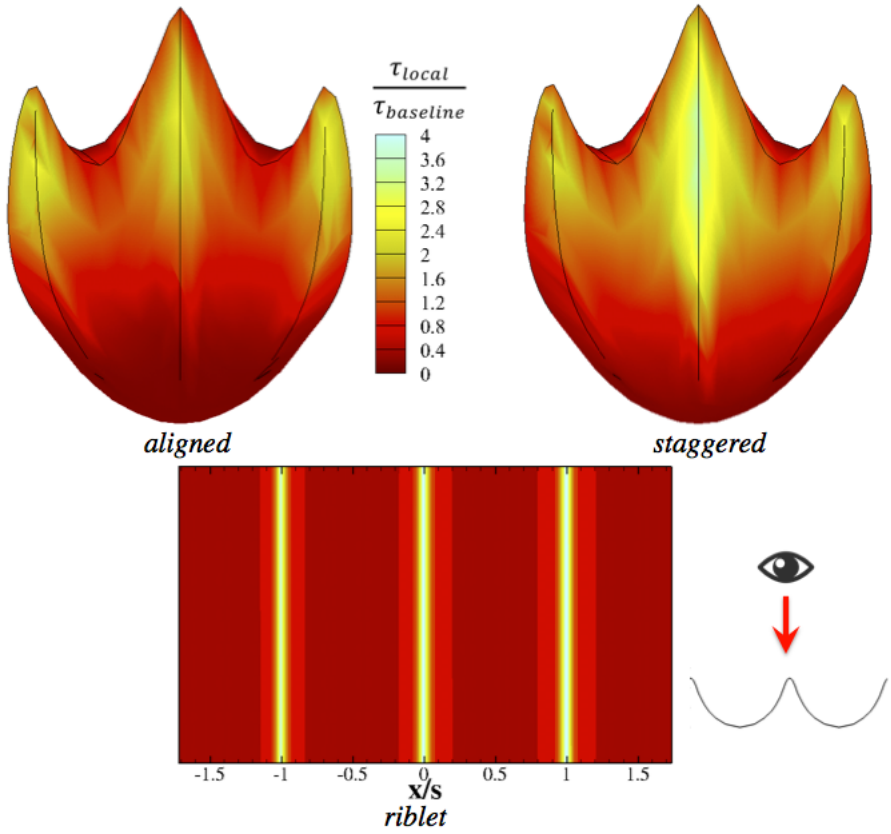

Figure 5.23: Contours of time and space averaged shear stress for the aligned (top left) and staggered (top right) denticle arrangements. Similar contours are plotted for the scalloped riblets (bottom).

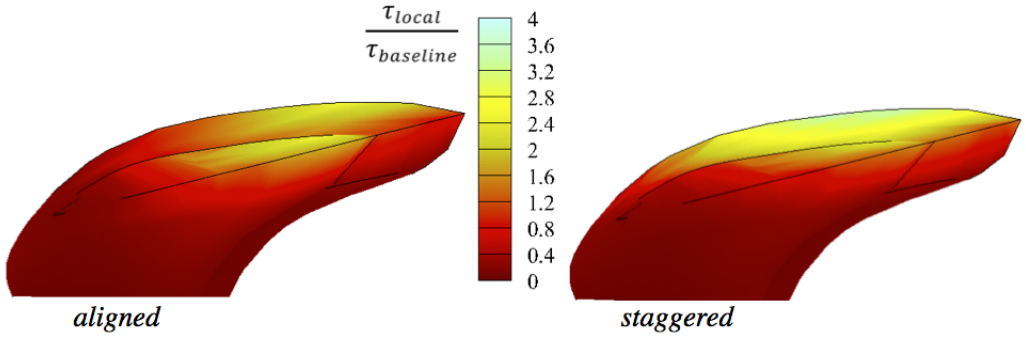

Figure 5.24: Contours of time and space averaged shear stress for the aligned (left) and staggered (right) cases.

5.2.4 Comparison with experimental observations.

The present results do not support the experimental findings of Wen & Lauder [10]. Their experimental results (from the static tests) indicated that the aligned arrangement reduced skin friction, similarly to riblets, up to a maximum of 9%. We argue that these differences should be attributed to different flow conditions between the simulated and experimental flow fields to which denticles were exposed. In the present work, the denticles are immersed in a canonical fully-developed turbulent channel flow. The sharkskin in the experimental work, however, was not. This is important because the skin friction relations used by Wen & Lauder [10] to determine s^+ of the sharkskin are only valid for flat plate, fully developed, zero-pressure gradient turbulent boundary layers.

As detailed by Wen & Lauder [10], the chord Reynolds number of the static test apparatus was only 44,000 at maximum. However, for a flat plate geometry, transition to turbulence occurs at a critical value of about $5\text{x}10^5$. The authors argue that transition has likely occurred due to a blunt leading edge (with some thickness, t_{blunt}), citing evidence from Lane & Loehrke [73]. Unfortunately, no velocity profiles were available near the test section to firmly establish that transition to turbulence had indeed occurred. We do note, however, that while transition to turbulence can indeed be triggered by a blunt edge, according to Lane & Loehrke [73], a separation bubble will also form. Using the experimental findings of Lane & Loehrke [73], the length of the separation bubble in Wen & Lauder [10] study could be approximately 9% of the test apparatus total test section. As a consequence, the unsteady flow created by the blunt edge in the experiment of Wen & Lauder [10] may not correspond to a canonical turbulent boundary layer. According to Ota & Itasaka [74], a Reynolds number (based on the blunt-edge thickness) similar to Wen & Lauder [10], would require $20t_{blunt}$ before a typical (log-law) turbulent boundary layer had developed. That would mean that about 40% of the experimental test section in Wen & Lauder [10] was exposed to a turbulent boundary layer with an unknown velocity profile.

The ramifications for a blunt-edge transition to turbulence are twofold: 1) the flow in the experiment of Wen & Lauder [10] does not resemble the flow in the present study; and 2) there is significant uncertainty concerning the values of s^+ reported by Wen & Lauder [10]. There is some other evidence for this uncertainty. At a value of $s^+ \approx 5.5$,

the sharkskin achieve maximum drag reduction. However, as $s^+ \to 0$, drag reduction must also approach zero (i.e., as the denticles become very small, the test section resembles a flat plate). This is well known as a viscous region for riblets, first detailed by Luchini et al. [3]. The sharkskin in the experimental work of Wen & Lauder [10], however, show no sign of a viscous region.

Regardless of the state of the turbulent boundary layer, Wen & Lauder's [10] sharkskin did reduce drag. The physical reason for that is unknown as our computations could not match the experimental flow conditions. The findings of Wen & Lauder [10], however, considered in conjunction with our results suggest that the hydrodynamic function of sharkskin denticles could depend strongly on the flow conditions to which denticles are exposed.

Chapter 6

Sharkskin Separation Control

In this chapter we conduct a numerical experiment to investigate whether or not sharkskin has the potential to delay separation, which could in turn decrease the total shark form drag. Mean profiles of velocity along with streamlines and turbulence statistics are examined.

6.1 Conceptual Framework.

Bechert et al. [16] was the first to introduce the concept that instead of behaving like riblets, sharkskin might act as vortex generators that prohibit separation. As mentioned in Section 1.2.3, Vortex Generators (VG) may vary in shape and size but all create turbulent mixing that increases momentum in areas prone to flow reversal. In Section 5.2.2, it was shown that staggered denticles in channel flow induce a complex flow field of counter-rotating vortices. The question is then, "Can the vorticity created by denticles delay separation?" Our initial approach was to simulate dynamic sharkskin on a wavy surface to approximate shark swimming. The details of the framework for this approach are provided in Appendix C. We chose however not to simulate dynamic sharkskin because shark swimming kinematics are unknown to us and because the grid needed for such a simulation would require computational resources that were unavailable. Therefore, our chosen approach to investigate this question uses the computational domain seen in Figure 6.1. Note that x, y, z directions correspond to Cartesian velocities u, v, w and where x is the

spanwise, y is the wall-normal, and z is the streamwise direction. A turbulent boundary layer is fed into the domain and a patch of sharkskin is immersed into a background mesh using CURVIB near a separation bubble. For a baseline case, we have performed the same simulation without any sharkskin. Our goal is to compare and contrast the two resulting separation bubbles and conclude if sharkskin has the ability to control separation.

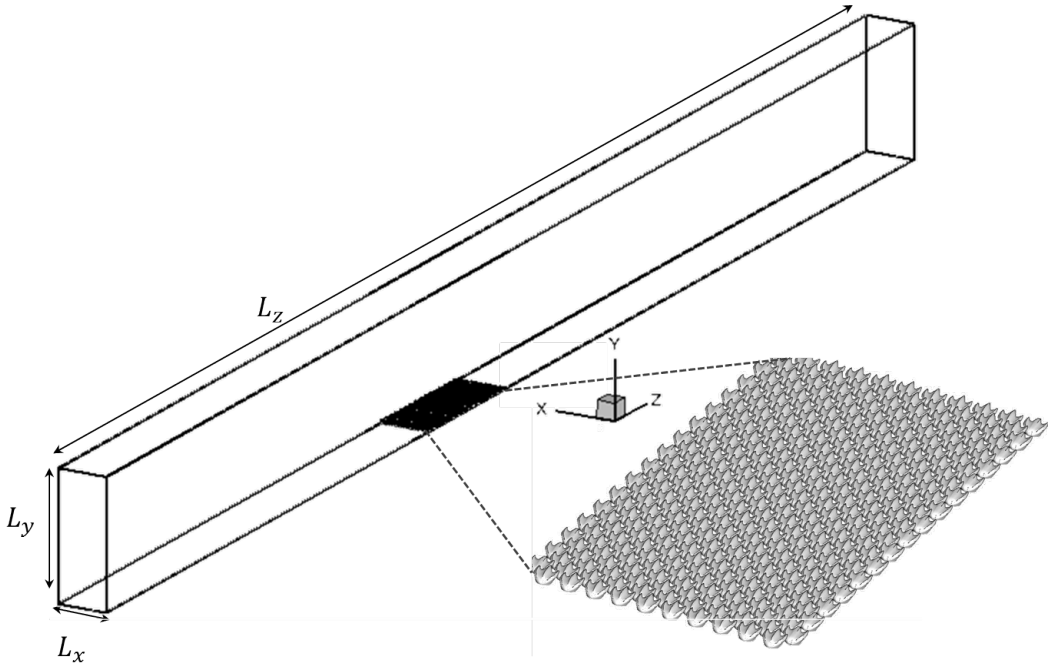

Figure 6.1: The main simulation domain with lengths L_x, L_y, and L_z. A patch of staggered denticles is immersed in the domain.

To determine the ability of sharkskin to control separation, a few critical parameters must first be examined. The first parameter to discuss is the strength of the Adverse Pressure Gradient (APG). Depending upon the APG, the resulting separation region can have varying amounts of flow reversal. That is, a strong APG will induce massive separation (more negative streamwise velocities), whereas a weak APG will induce a light separation (near-zero streamwise velocities). Accordingly, more turbulent mixing by the VG is required for a strong APG than for a weaker APG. With this in mind, we have simulated a lightly separated bubble to give sharkskin the best chance at delaying separation. The separation bubble from the baseline case is shown Figure 6.2 and it plots contours of

spanwise-averaged mean streamwise velocity. The separation bubble is present from about $190 \leq z/\theta_{inlt} \leq 275$.

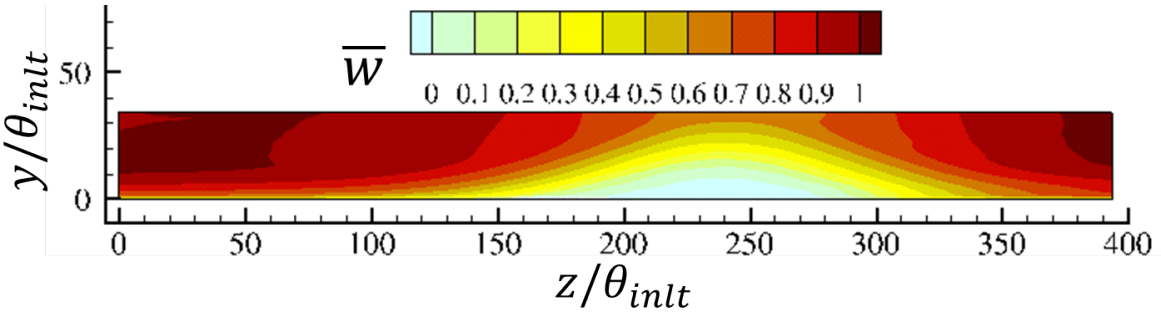

Figure 6.2: Side view of the main simulation domain. Contours plot mean streamwise velocity. A separation bubble exists from about $190 \leq z/\theta_{inlt} \leq 275$.

The next parameter to discuss is the VG (in this case, each denticle) height to boundary layer height ratio, h/δ, which is a function of Reynolds number and denticle size. Choosing a realistic value of h/δ is difficult because the boundary layer height over a shark is unknown and will vary with downstream location. However, this parameter has, in part, already been addressed when choosing a value of s^+ for the denticle simulations in Chapter 5. Raschi & Musick [8] calculated that at burst shark swimming speeds, $s^+ \approx 13 - 15$. Although this calculation is based on skin-friction coefficients meant for a flat plate zero pressure gradient, it is currently the best estimate for denticle size relative to the turbulent flow. Therefore, for this separation control investigation, we have chosen to simulate the denticles with an $s^+ = 16$ as was done in Chapter 5. The Reynolds number, $Re_\theta inlt = W_0\theta_{inlt}/\nu$ (where W_0 and θ_{inlt} correspond to the freestream velocity and momentum thickness at the inlet, respectively) used in this investigation is $Re_\theta inlt = 660$. This Reynolds number nears the limit of our ability to simulate sharkskin in a turbulent boundary layer, due to large grid cell counts.

The last parameters to examine are the placement of the sharkskin and the number of denticles. Denticles are geometrically complex, and as shown by the grid independence study in Section 5.1 at an $s^+ = 16$, each requires 50 grid points in every direction to accurately resolve their shape and compute local shear forces. This restraint results in large cell counts, so unfortunately, simulating large patches of denticles isn't feasible with

our available computing resources. A staggered arrangement of denticles is placed some distance, L_d, from the inlet. L_d was chosen such that the last row of denticles ended near the leading edge of the separation bubble calculated from the baseline case, which is shown in Figure 6.2. This figure plots contours of spanwise-averaged mean streamwise velocity. The streamwise length of the sharkskin patch, L_p is approximately 1/2 the length of the separation bubble. L_p is is the largest feasible length of sharkskin that we were able to simulate.

6.2 Computational Grid & Boundary Conditions.

In order to simulate a separation bubble, the turbulent boundary layer must have a height less than the height of the domain. This requires a realistic turbulent boundary layer inflow at each timestep. To accomplish this, we have employed the Spatially Developing Turbulent Boundary Layer (SDTBL) inflow generation technique of Lund et al. [67], which is described in depth in Section 2.4. A rescaling domain with an identical cross-section to the main simulation domain in Figure 6.1 is used to develop a SDTBL. At the recycling plane, Cartesian velocities are stored at each timestep as inlet boundary conditions to the main simulation domain. Figure 6.3 plots spanwise averaged mean streamwise velocity at the recycling plane of the rescaling domain. Figure 6.4 shows root-mean square values of streamwise fluctuations, also at this plane. In general good agreement is obtained, though there is some over prediction in the outer layer ($0.6 \leq y/\delta \leq 1.2$) for $Re_\theta = 660$. We have thoroughly investigated the cause of this over-prediction and have concluded that it is a consequence of the rescaling method at this low Reynolds number. Such over-predictions have also been discussed by Liu & Pletcher [69].

To create an APG strong enough to induce separation, we have followed the approach of Na & Moin [75], who created a two-dimensional separation bubble by modifying the flux at the top of the domain. This flux was fixed throughout their simulation and was chosen *a priori*. Figure 6.5 shows the flux imposed at the top of the domain as it varies with streamwise location. Note that at $z/\theta_{inlt} \approx 200$, a blowing occurs, forcing the flow to reattach and creating a bubble. Also plotted is the resulting spanwise averaged mean skin friction coefficient on the bottom surface. Maximum values of C_f are apparent at the inlet and outlet, with a near zero value in the separation region. No-slip conditions are used

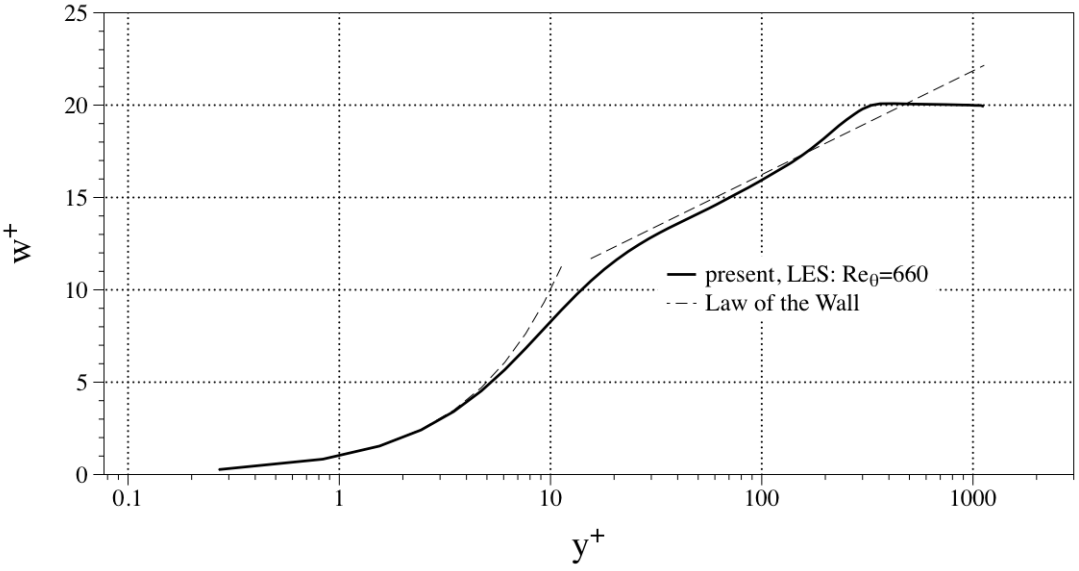

Figure 6.3: Mean streamwise velocity at the recycling plane of the rescaling domain. The logarithmic region of the law of the wall is the function $w^+ = 2.44ln(y^+) + 5$.

for the sharkskin and the surface to which they are affixed (i.e., the epidermis). Periodic boundary conditions are used for the spanwise direction and at the outlet, we employ a convection boundary condition.

Figure 6.6 is a side view of the computational domain with corresponding grid cell counts and spacings for different streamwise regions. Near the sharkskin, 50 grid cells are used to resolve each denticle in every direction, following the grid independence study in Section 5.1. In the wall-normal direction, a stretched grid is used to resolve the no-slip boundaries. For the spanwise direction, a uniform mesh is employed. Table 6.1 details the computational grids used for both the sharkskin and baseline cases. Note that the grid spacings, Δx^+ and Δy^+ use the shear velocity at the inlet for normalization. The timestep for each case is the same and resulted in a $CFL_{max} \approx 0.5$. During the initial timesteps, mean kinetic energy was monitored until it reached a statistically stationary state. Time-averaging then occurred for $2,950\theta_{inlt}/W_0$ non-dimensional time units.

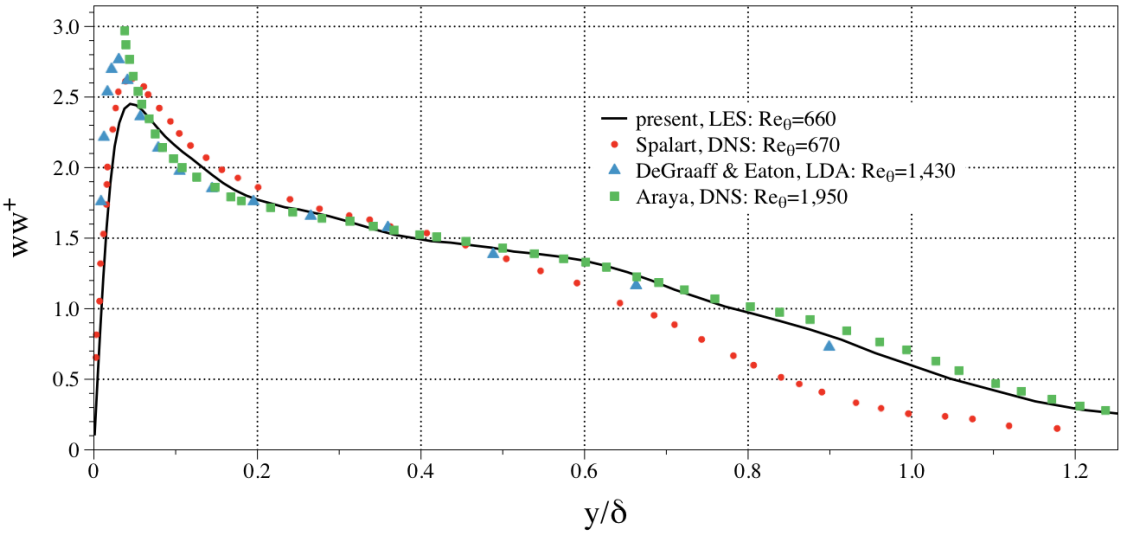

Figure 6.4: Streamwise turbulence intensity at the recycling plane of the rescaling domain. Red circles are computational data from Spalart [17]. Blue triangles experimental measurements from DeGraaff & Eaton [14]. Green squares from Araya et al. [15].

Table 6.1: Computational domain details for each sharkskin separation control simulation. N_x, N_y, and N_z represent the number of grid nodes in each respective direction.

Case	L_x	L_y	L_z	N_x	N_y	N_z	Δx^+	Δy^+_{min}	Δy^+_{max}
baseline	$13.3\theta_{inlt}$	$35\theta_{inlt}$	$394\theta_{inlt}$	583	119	2639	0.75	0.8	55
sharkskin	$13.3\theta_{inlt}$	$35\theta_{inlt}$	$394\theta_{inlt}$	583	119	2639	0.75	0.8	55

6.3 Results & Discussion.

Figure 6.7 shows the mean separation bubble boundary for the baseline and sharkskin cases. The figure was created by spanwise averaging the mean streamwise velocity and then plotting an isosurface where its value was equal to zero. The denticles in the bottom left corner are scaled appropriately and mark the last row of staggered denticles. It is observed that instead of preventing separation, the patch of sharkskin actually enlarges the separation bubble.

In order to determine why the separation bubble grows with sharkskin, for Figures 6.8 - 6.10, we have spanwise-averaged the mean flow field. First, Figure 6.8 plots mean streamwise velocities at multiple streamwise locations, z/θ_{inlt}, over the sharkskin. The

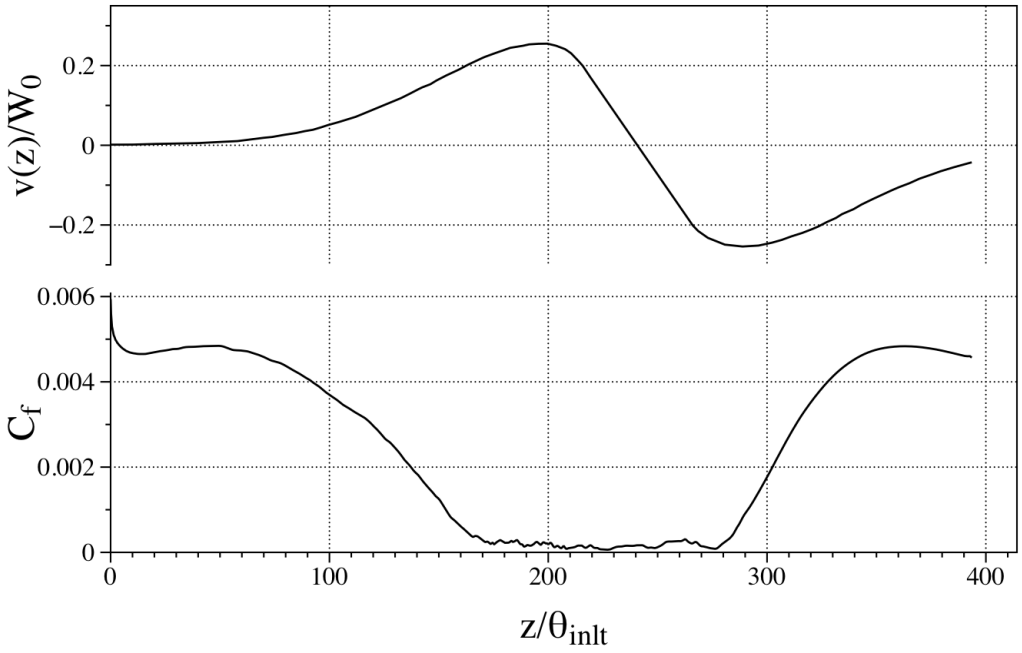

Figure 6.5: Top: Prescribed flux at the top of the main simulation domain used to induce a separation bubble. Bottom: Corresponding skin-friction coefficient at the bottom wall of the main simulation domain as a function of streamwise direction.

denticle in the lower left is to scale. The reason for an enlarged region of separation is clearly due to decreased momentum near the sharkskin. Near the first row of denticles ($z/\theta_{inlt} = 156$), the sharkskin causes an initial drop in streamwise velocity and the flow never recovers, as one progresses downstream over the sharkskin to $z/\theta_{inlt} = 191$. Obviously, a decrease in momentum near the denticle surface is opposite of what is needed to delay separation. In Figure 6.9 we plot streamwise velocity at four streamwise locations within the separation bubble. We see from this figure that throughout the height and length of the separation bubble, the sharkskin leads to decreased streamwise momentum. Though the denticles are approximately just 10% of the inlet boundary layer height (as depicted by the grey region) their affects are felt throughout the bubble. At $z/\theta_{inlt} = 226$ and 250, not only is there a just a reduction in velocity, but a mean negative streamwise velocity at $z/\theta_{inlt} = 250$.

As was seen in Section 5.2.2, the staggered denticles in turbulent channel flow induced a alternating pattern of negative and positive streamwise vorticity. Along with this came

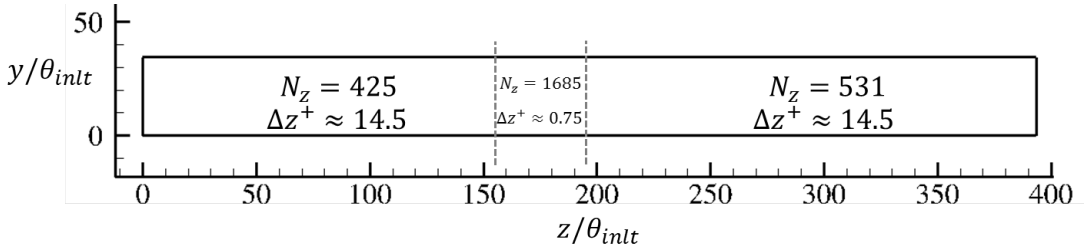

Figure 6.6: Grid cell streamwise counts (N_z) in different regions of the main simulation domain. Denticles reside in the center of the domain where the highest resolution is present.

a drastic increase in streamwise turbulent fluctuations. For comparison, Figure 6.9 plots spanwise averaged streamwise turbulence intensity. Three streamwise locations have been plotted, one at the first row of denticle, one in the middle of the patch, and another just downstream of the sharkskin. In this figure, we see that Instead of increasing turbulence, the sharkskin is shown to reduce turbulence intensities. This result, along with the velocity profiles in Figure 6.8 indicate that the turbulent flow separates near the first row of denticles.

Further evidence for separation near the first or second rows of denticles is shown in Figure 6.11. Here, we plot limiting streamlines on the epidermis. Contours of shear velocity are also plotted. We can see that the streamlines show *reversed* flow starting at the second row of denticles. This flow reversal continues throughout the downstream denticles, indicating sustained separation. Reversed flow was not observed in either the staggered or aligned sharkskin cases when placed in turbulent channel flow.

Lang et al. [49] just recently reported experimental results with sharkskin mounted on an airfoil with variable Angle of Attack (AOA). The authors used PIV to quantify flow separation at $AOA = 8°, 10°, 12°, 14°, 16°, 18°$. Lang et al. [49] present data that show that sharkskin can actually prevent separation, but not until $AOA > 16°$. In fact, the data show that at lower AOA, flow separation was worse than without sharkskin. These experimental results agree with the present simulations, that is, weak regions of separation are made worse by sharkskin. In their paper, Lang et al. [49] theorize that sharkskin doesn't help to control separation until higher AOA because higher AOA could correlate with stronger reversed flow. This reversed flow would in turn, actuate individual denticles to flip upwards, or bristle (see Section 1.2.3 for more detail concerning Bechert et al. [16]

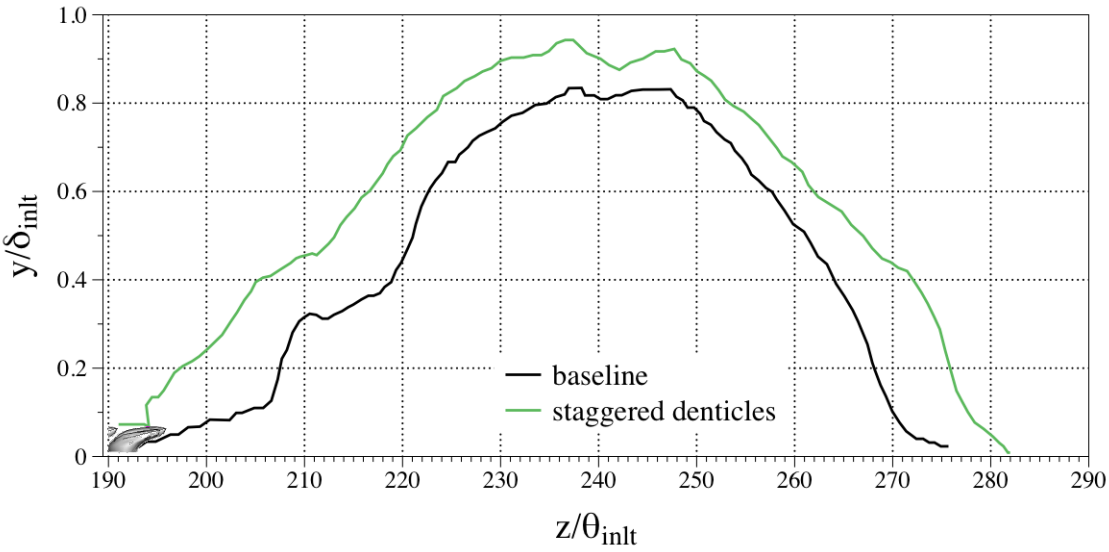

Figure 6.7: Boundary of the separation bubble for the baseline and sharkskin cases. The denticles in the lower left are to scale and are at the very final row of the sharkskin patch.

and bristling). The present simulations are unable to provide evidence for the proposed beneficial effects of bristling since we only simulated fixed denticles. However, provided that the turbulent flow in the present case separated at just the second row of denticles, it would seem doubtful that in our case, bristling would have helped reduce separation.

The most important question to consider now is what causes sharkskin in turbulent channel flow to increase Reynolds stresses near their surfaces and just the opposite in the present simulation. The answer lies in Figures 6.8 and 6.11. In the present case, the sharkskin performed more like blockages to the flow rather than VG, immediately reducing streamwise momentum, at the leading edge of the sharkskin patch, that was never recovered due to separation. This in turn caused reversed flow among the denticles, which was never observed for denticles in channel flow.

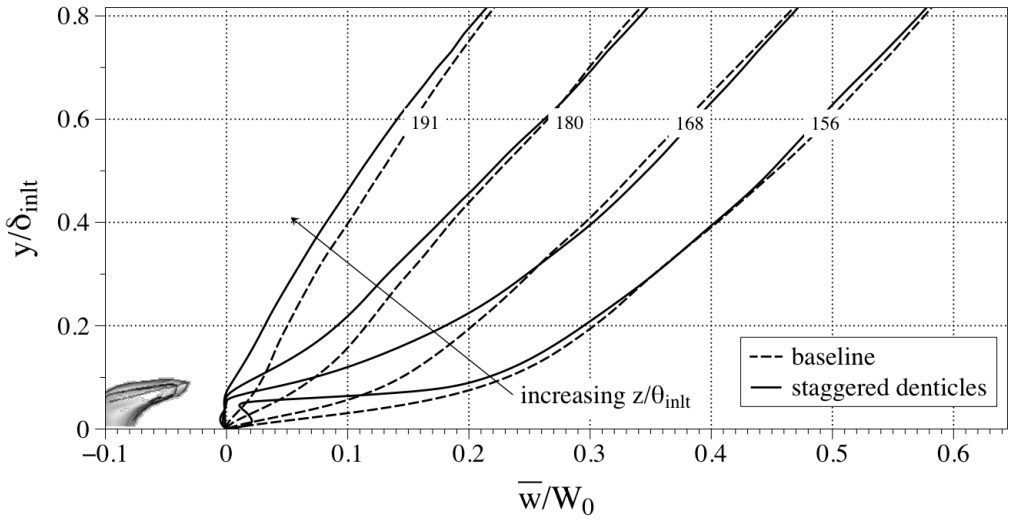

Figure 6.8: Mean streamwise velocity profiles at four streamwise locations at $z/\theta_{inlt} = 156, 168, 180, 191$. The arrow indicates increasing downstream location. The denticle is to scale and included to determine its affect on the flow.

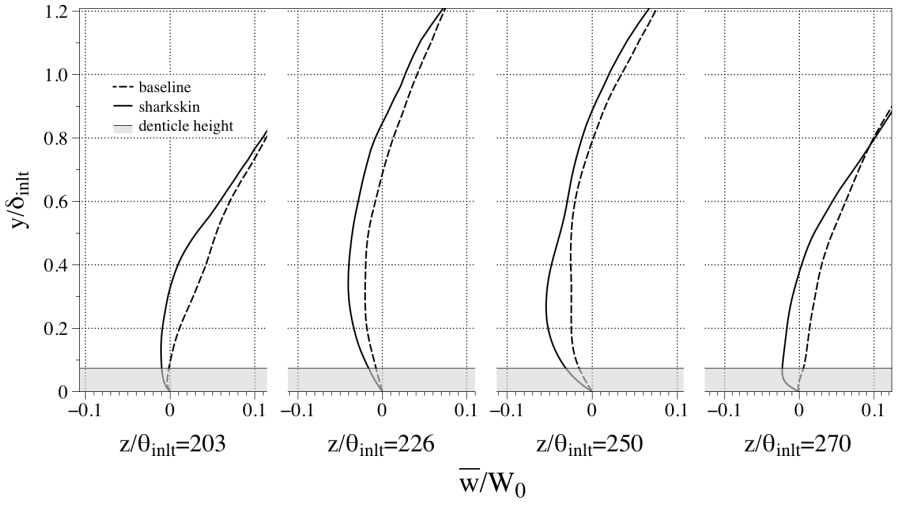

Figure 6.9: Mean streamwise velocity profiles at four streamwise locations. Each location is within the separation bubble. The grey portion in each graph represents the height of the sharkskin

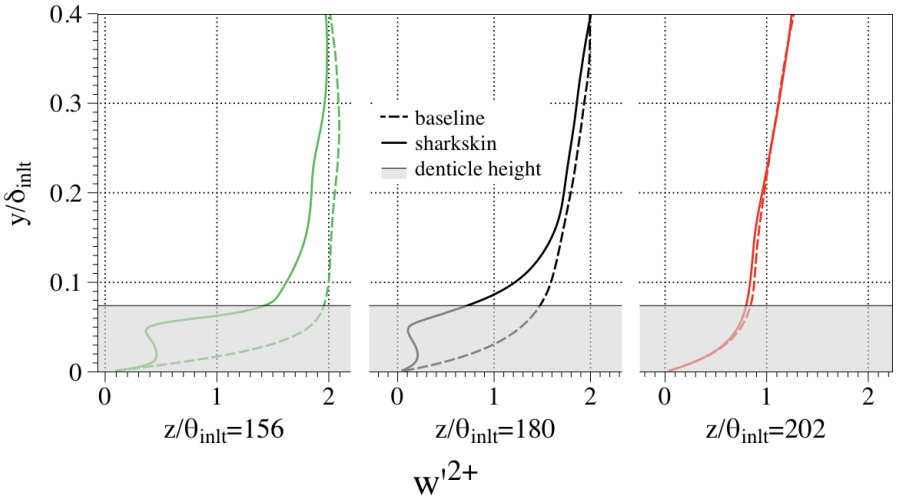

Figure 6.10: Streamwise turbulence intensity profiles at three streamwise locations, each at a location within the sharskin patch. The grey region demonstrates denticle height.

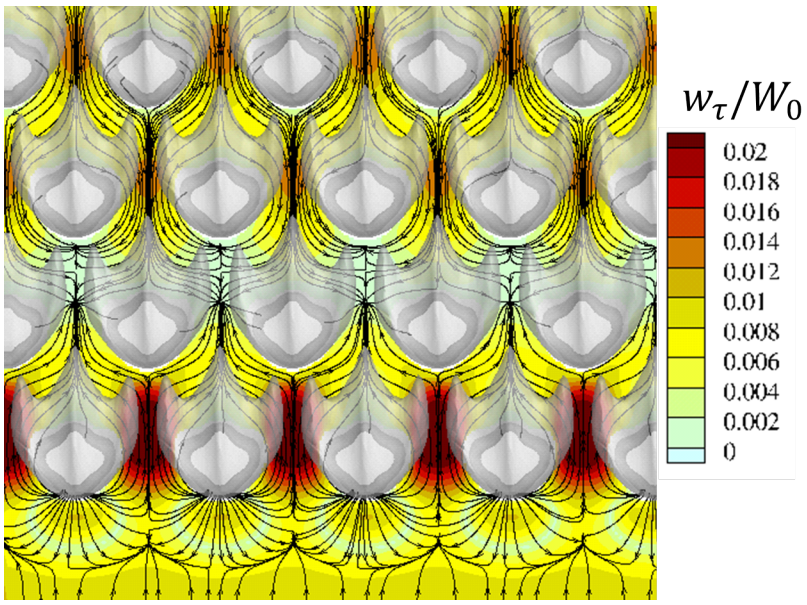

Figure 6.11: Limiting streamlines of mean streamwise velocity on the shark epidermis. Contour of mean shear velocity are also plotted. Flow reversal occurs at the second row of denticles.

Chapter 7

Conclusion and Outlook

A study concerning two different types of roughness elements in turbulent flows has been undertaken to determine their effects on the boundary layer, and in turn their effect on the wall shear stresses. Turbulent roughness can be classified into three categories: hydrodynamically smooth, transitional, and fully-rough. Although hydrodynamically smooth roughness have no affect on wall shear stress, it is usually the case that turbulent roughness create additional drag on the surfaces to which they are mounted. In this study though, we have simulated turbulent roughness that have been often thought to reduce drag.

Using computational fluid dynamics, we first simulated turbulent flow over riblets. These micro-grooves that are aligned with the primary direction of flow have been studied for over 30 years and have a proven record of reducing drag up to 10%. This rich research history however, has largely focused on riblets in channel flows and Zero Pressure Gradient (ZPG) boundary layers. The motivation for the current study stems from the fact that potential applications (e.g., wind or gas turbine blades, ship hulls), of riblets in real flows often have turbulent boundary layers under Adverse Pressure Gradients (APG). Unfortunately, the few fundamental studies concerning riblets in APG disagree on the extent of the hydrodynamic benefits of riblets. Recent studies by Klumpp et al. [48] (computational) and Debisschop & Nieuwstadt [6] (experimental) have both confirmed that not only is riblet drag reduction possible in APG, but that it is proportional to the strength of the APG. This is important because potential applications could see a larger than expected benefit from riblets. However, each study disagrees on the amount of increase in drag

reduction, specifically in regards to mild APG. In order to clarify this issue and to further fundamental research of riblets in APG, we have methodically simulated different sized scalloped riblets in both a mild APG and a ZPG and compared the riblet drag reduction in both types of flows.

In order to simulate riblets in ZPG and APG, we have implemented the rescaling method of Lund et al. [67]. The rescaling method was used to generate a spatially developing turbulent boundary layer for inlet boundary conditions. After implementation, the rescaling method was validated via comparisons with other computational data as well as experimental. Great care was taken to ensure that each riblet simulation (for respective ZPG and APG flows) was exposed to the same turbulent boundary layer, thus ensuring accurate drag reduction comparisons among riblet cases. The Navier-Stokes equations were solved with a finite-difference, fractional-step method that was second-order accurate in time and second-order accurate in space. Using Large Eddy Simulation (LES), turbulence closure occurred with a dynamic Smagorinsky model. Due to our method and high-resolution background mesh, detailed flow fields were obtained within individual riblets. The Clauser parameter for the equilibrium APG boundary layer was 0.5.

We have clearly shown that a mild APG has a modest but measurable effect on the drag reduction properties of scalloped riblets, and that our data supports the experimental findings of Nieuwstadt [5]. Our data disagrees with the computational results from Klumpp et al. [48]. One likely reason for the discrepancy could be that the present simulations have a much higher grid resolution near the riblet surface. In the study of Klumpp et al. [48], about 20 grid points were used to discretize a riblet. In our simulations, a similar riblet was resolved with 33 points. Furthermore, Klumpp et al. [48] did not report a grid refinement study. Another possible, but unlikely, cause could be that the $h/s = 0.3$ for the simulation of Klumpp et al. [48], but here it was 0.5. Such a possibility is unlikely because the h/s value for the experimental findings of Nieuwstadt & Debischopp [6] (which the present results support) tested riblets with $h/s = 1.0$.

Since the present simulations encompass a range of s^+ values, we have also shown that peak streamwise fluctuation levels scale with riblet width, not drag reduction. Similar scaling trends were seen for turbulent kinetic energy peak values and maximum values of streamwise vorticity. In contrast, the primary Reynolds shear stress did scale with riblet

drag reduction values. Overall, there was little difference in turbulence statistics between riblets in ZPG and APG flows, but this is not surprising since the improvement in drag reduction by riblets in APG was a modest increase. Overall, scalloped riblets in APG retain their drag reducing properties, but our simulations are evidence that only under moderate to strong APG are these properties enhanced.

The future outlook on riblet research could focus on simulating riblets in different strengths of APG. Over the span of Clauser parameter, β, Nieuwstadt & Debischopp [6] have reported an increase in drag reduction from 5% at low β to 13% with the same riblet. By testing different APG strengths with high resolution LES, researchers might elucidate the fundamental reasons for the increase in drag reduction.

The second type of turbulent roughness that we have simulated is biological: sharkskin. Sharkskin is comprised of thousands of small tooth-like structures called denticles. Working in collaboration with Li Wen and George Lauder of Harvard, we were given a three-dimensional model of a representative denticle from a Mako shark. Each denticles is geometrically complex and as such, a structured boundary-fitted grid with adequate resolution and quality would be very difficult to create. Therefore, we have employed the CURVIB method of Ge and Sotiropoulos [60]. CURVIB is a sharp-interface immersed boundary method. Using this method, each denticle was first discretized using a triangular unstructured mesh and then immersed in a curvilinear background mesh. To compute the shear on the sharkskin, the background mesh must be sufficiently fine that a first order approximation to the gradient at the boundary is accurate. To ensure such accuracy, a grid independence study was performed. We also performed two-point correlations within the computational domain to affirm that the size of the domain was adequately large enough to drive correlations to zero.

Two different arrangements (aligned and staggered) of sharkskin denticles were simulated in a periodic turbulent channel flow with Direct Numerical Simulation (DNS). In order to compare and contrast denticles and riblets, we also simulated similarly sized scalloped riblets in a fully developed channel flow. The Navier-Stokes equations were solved with a finite-difference, fractional-step method that was fourth-order accurate in time and second-order accurate in space. Due to our method and high-resolution background mesh, detailed flow fields were obtained around individual denticles. This is the first time that

such detailed simulations for actual denticle shapes have been reported.

Compared to a flat plate without sharkskin, an aligned denticle arrangement increased total drag by 44%, and a staggered increased total drag by 50%. Even though denticles resemble riblets, we have found that the three-dimensionality of the denticle geometry enhances turbulent mixing and increases skin-friction. More specifically, there are several key differences between denticles and drag-reducing riblets:

1. 25% of total denticle drag is attributable to form drag, due to separation around individual denticles. Riblets have no form drag.

2. Significant secondary flow is present along the outer keels and even under the keels of denticles.

3. The denticles significantly increase Reynolds stresses. Riblets decrease these statistics.

4. Riblets induce steady counter-rotating vortices on either side of the peaks, but only for the aligned case such vortices are seen for denticles.

5. Riblets isolate high mean shear stress to peaks, but denticles are unable to do so; denticle valleys are areas of high shear stress and in both cases, the entire primary keel is exposed to high velocity gradients.

Our results have conclusively shown that the three-dimensionality of the denticles causes secondary flow that is the cause of drag increase. Specifically, the staggered arrangement created a alternating pattern of negative and positive streamwise vorticity that was not observed with the scalloped riblets. Our results agree well with the experimental works of Bechert et al. [16] and suggest that sharkskin denticles will only function as riblets *if the denticles are at a low angle of incidence and interlock*. Most importantly, for sharkskin to reduce skin friction like riblets, they must be sized correctly, and this is very difficult to know without knowing the shear velocity distribution on a shark.

Notably, in the aligned case, our results do not agree with the experimental study by Wen & Lauder [10], even though the same denticle was used in both studies. The cause is likely due to the difference in flow conditions to which denticles were exposed in the

experiments and our simulations. The fact that denticles were able to reduce drag in the experiment of Wen & Lauder [10], however, does suggest that further studies are needed to systematically investigate the function of denticles in different flow environments.

Future research concerning sharkskin could focus on simulating different types of flow conditions, specifically, SDTBL. Indeed, the experimental work of Wen & Lauder [10] were able to reduce drag, though the reason for this is unknown, especially considering our conclusive results showing that sharkskin does not behave similarly to riblets. Future studies could also focus on different denticle arrangements. The arrangements seen in nature can vary widely, and more attention with regards to denticle spacing would be beneficial since we've shown that denticle three-dimensionality was detrimental to drag reduction.

In the third and final set of simulations for this dissertation, we simulated Mako sharkskin near a separation bubble. This experiment was undertaken to examine the ability of denticles to promote turbulent mixing, and in turn increase the momentum in the turbulent boundary layer, similarly to the behavior of vortex generators. Delaying or prohibiting separation would likely reduce the overall pressure drag for the shark, thereby decreasing the cost of transport for the animal. The separation bubble was created by applying a wall-normal mass flux to the top of the domain, which was a similar approach to that taken by Na & Moin [75]. Again, to simulate the sharkskin in turbulent flow, we utilized the CURVIB method in conjunction with the rescaling method to provide realistic inlet boundary conditions. We employed LES with a fractional step method that was second order accurate in space and time.

The results conclusively showed a worsening (i.e., growth) of the separation region. Not only did the separation bubble grow, but increased flow reversal within the bubble also occurred. From plots of mean velocities, we observed that the denticles did not increase momentum via turbulent mixing similar to vortex generators. Instead, the denticles acted as blockages that initially slowed the turbulent flow that never recovered. From time-averaged limiting streamlines on the shark's epidermis, it was shown that flow reversal within the sharkskin patch occurred just after the first row of denticles. Sustained reversed flow was never observed for denticles in channel flow. Lastly, we have shown that

streamwise turbulence intensities near the sharkskin were decreased in the separation control experiment. This too was caused by almost immediate separation near the second row of denticles. Our results did not conflict with the recent experimental results of Lang et al. [49] who although showed that sharkskin could prevent separation for strong regions of separation, showed that denticles worsened weaker separation regions. The authors postulated that only bristled denticles could control separation, though in our case, this would seem unlikely since separation occurred so quickly.

Future research concerning separation control by denticles could focus on increasing the amount of denticles upstream of separation bubbles. In the present study, we were restricted by computational resources to include a patch of denticles with a length equal to half the size of the separation bubble. In the future, studies might be able to increase the number of denticles so that separation might not occur so quickly and perhaps allow the sharkskin to promote turbulent mixing. Also, the size of the denticles might be increased to a point where separation was controlled since knowing denticle dimensions relative to boundary layer height and Reynolds number on a shark is difficult.

Finally, we have also completed performance testing of the CURVIB method. In conjunction with in-house testing, we were also provided sole use of the RedMesa supercomputer of Sandia National Laboratory. The 25,000 core machine has been the largest computational test bed for CURVIB to date. Our results have shown that CURVIB has a strong-scaling efficiency of approximately 30-40%. Strong scaling references the simulation turn-over rate. Our tests have shown that the low efficiency is in large part due to intra-node communication bottlenecks during the Poisson equation solves. When running only have the number of cores per node, strong-scaling efficiency increased to 50-60%. The other reason for low efficiency could be attributed to poor library performance. When using built-in PETSc algebraic multigrid preconditioning, efficiency again increased to approximately 50%. We also tested weak scaling. Weak scaling is a measure of the efficiency of the application to use its resources effectively. Here, the efficiency was much better, about 80%. However, it should be noted that efficient strong-scaling is typically more difficult to achieve.

Future scaling improvements to CURVIB might first focus on improvements to the Poisson equation preconditioner. Second, and much more difficult, would be to implement

a hybrid implementation of inter and intra node communication. The state-of-the-art is to utilize OpenMPI for communication among nodes and OpenMP for communication within nodes (among cores). Further out in the future, CURVIB could possibly be accelerated by using Graphical Processing Units (GPU). This though must be considered carefully, as efficient GPU acceleration requires minimal memory transfers. Unless a large amount of on-board memory is available on the GPU, acceleration would be difficult.

References

[1] J. Nikurads. Stromungsgesetze in rauhen rohren. *VDI Forschungsh*, 361, 1933.

[2] DW Bechert, M Bruse, W Hage, JG Th Van der Hoeven, and G Hoppe. Experiments on drag-reducing surfaces and their optimization with an adjustable geometry. *Journal of Fluid Mechanics*, 338(5):59–87, 1997.

[3] Paolo Luchini, Fernando Manzo, and Amilcare Pozzi. Resistance of a grooved surface to parallel flow and cross-flow. *Journal of Fluid Mechanics*, 228:87–109, 1991.

[4] S-J Lee and S-H Lee. Flow field analysis of a turbulent boundary layer over a riblet surface. *Experiments in fluids*, 30(2):153–166, 2001.

[5] FTM Nieuwstadt, W Wolthers, H Leijdens, K Krishna Prasad, and A Schwarz-van Manen. The reduction of skin friction by riblets under the influence of an adverse pressure gradient. *Experiments in fluids*, 15(1):17–26, 1993.

[6] JR Debisschop and FTM Nieuwstadt. Turbulent boundary layer in an adverse pressure gradient-effectiveness of riblets. *AIAA journal*, 34(5):932–937, 1996.

[7] PR Viswanath. Aircraft viscous drag reduction using riblets. *Progress in Aerospace Sciences*, 38(6):571–600, 2002.

[8] William Raschi and John A Musick. *Hydrodynamic aspects of shark scales*, volume 3963. National Aeronautics and Space Administration, Scientific and Technical Information Branch, 1986.

[9] DW Bechert, M Bruse, W Hage, and R Meyer. Fluid mechanics of biological surfaces and their technological application. *Naturwissenschaften*, 87(4):157–171, 2000.

[10] Li Wen, James C Weaver, and George V Lauder. Biomimetic shark skin: design, fabrication and hydrodynamic function. *The Journal of experimental biology*, 217(10):1656–1666, 2014.

[11] PR Ashill, JL Fulker, and KC Hackett. Research at dera on sub boundary layer vortex generators (sbvgs). *AIAA paper*, 887, 2001.

[12] John Kim, Parviz Moin, and Robert Moser. Turbulence statistics in fully developed channel flow at low reynolds number. *Journal of fluid mechanics*, 177:133–166, 1987.

[13] Haecheon Choi, Parviz Moin, and John Kim. Direct numerical simulation of turbulent flow over riblets. *Journal of fluid mechanics*, 255:503–539, 1993.

[14] David B De Graaff and John K Eaton. Reynolds-number scaling of the flat-plate turbulent boundary layer. *Journal of Fluid Mechanics*, 422:319–346, 2000.

[15] Guillermo Araya, Kenneth E Jansen, and Luciano Castillo. Inlet condition generation for spatially developing turbulent boundary layers via multiscale similarity. *Journal of Turbulence*, (10), 2009.

[16] W Reif and D Bechert. On the drag reduction of the shark skin. *AIAA Shear Flow Control Conference*, (AIAA-85-0546), 1985.

[17] Philippe R Spalart. Direct simulation of a turbulent boundary layer up to rθ= 1410. *Journal of Fluid Mechanics*, 187:61–98, 1988.

[18] Lian Shen, Xiang Zhang, Dick KP Yue, and Michael S Triantafyllou. Turbulent flow over a flexible wall undergoing a streamwise travelling wave motion. *Journal of Fluid Mechanics*, 484:197–221, 2003.

[19] Gotthlif Heinrich Ludwig Hagen. *Über den einfluss der temperatur auf die bewegung des wassers in röhren–*. Druckerei der Königl. akademie der wissenschaften, 1854.

[20] Henry Darcy. Recherches experimentales relatives au mouvement de l'eau dans les tuyaux. *Mallet-Bachelier, Paris*, 1857.

[21] Julius Ludwig Weisbach. *Lehrbuch der ingenieur-und maschinen-mechanik: Statik der bauwerke & mechanik der umtriebsmaschinen*. Vieweg, 1848.

[22] Cyril Frank Colebrook. Turbulent flow in pipes, with particular reference to the transition region between the smooth and rough pipe laws. *Journal of the ICE*, 11(4):133–156, 1939.

[23] Michael J Walsh. Riblets. *Viscous drag reduction in boundary layers*, 1:203–261, 1990.

[24] SJ Kline, WC Reynolds, FA Schraub, and PW Runstadler. The structure of turbulent boundary layers. *Journal of Fluid Mechanics*, 30(04):741–773, 1967.

[25] Garry L Brown and Anatol Roshko. On density effects and large structure in turbulent mixing layers. *Journal of Fluid Mechanics*, 64(04):775–816, 1974.

[26] M. Walsh. Turbulent boundary layer drag reduction using riblets. *AIAA Paper 82-0169*, 1982.

[27] Michael J Walsh. Riblets as a viscous drag reduction technique. *AIAA journal*, 21(4):485–486, 1983.

[28] Ricardo Garcia-Mayoral and Javier Jimenez. Hydrodynamic stability and breakdown of the viscous regime over riblets. *Journal of Fluid Mechanics*, 678:317–347, 2011.

[29] Laurel W Reidy and Greg W Anderson. *Drag reduction for external and internal boundary layers using riblets and polymers.* Defense Technical Information Center, 1988.

[30] E Coustols. Behaviour of internal manipulators-'riblet' models in subsonic and transonic flows. In *AIAA, Shear Flow Conference, 2nd, Tempe, AZ*, page 1989, 1989.

[31] MR Raupach, JJ Finnigan, and Y Brunet. Coherent eddies in vegetation canopies. 1989.

[32] Javier Jiménez. Turbulent flows over rough walls. *Annu. Rev. Fluid Mech.*, 36:173–196, 2004.

[33] P Vukoslavcevic, JM Wallace, and J-L Balint. Viscous drag reduction using streamwise-aligned riblets. *AIAA journal*, 30(4):1119–1122, 1992.

[34] Seong-Ryong Park and James M Wallace. Flow alteration and drag reduction by riblets in a turbulent boundary layer. *AIAA journal*, 32(1):31–38, 1994.

[35] Yuji Suzuki and Nobuhide Kasagi. Turbulent drag reduction mechanism above a riblet surface. *AIAA journal*, 32(9):1781–1790, 1994.

[36] Douglas C Chu and George Em Karniadakis. A direct numerical simulation of laminar and turbulent flow over riblet-mounted surfaces. *Journal of Fluid Mechanics*, 250:1–42, 1993.

[37] D Goldstein, R Handler, and L Sirovich. Direct numerical simulation of turbulent flow over a modeled riblet covered surface. *Journal of Fluid Mechanics*, 302:333–376, 1995.

[38] Stephen K Robinson. Coherent motions in the turbulent boundary layer. *Annual Review of Fluid Mechanics*, 23(1):601–639, 1991.

[39] CR Smith, JDA Walker, AH Haidari, and BK Taylor. Hairpin vortices in turbulent boundary layers: the implications for reducing surface drag. In *Structure of Turbulence and Drag Reduction*, pages 51–58. Springer, 1990.

[40] L Djenidi and RA Antonia. Laser doppler anemometer measurements of turbulent boundary layer over a riblet surface. *AIAA journal*, 34(5):1007–1012, 1996.

[41] Kwing-So Choi. Near-wall structure of a turbulent boundary layer with riblets. *Journal of fluid mechanics*, 208:417–458, 1989.

[42] J Szodruch. Viscous drag reduction on transport aircraft. *AIAA paper*, (0685), 1991.

[43] Leonardo P Chamorro, REA Arndt, and F Sotiropoulos. Drag reduction of large wind turbine blades through riblets: Evaluation of riblet geometry and application strategies. *Renewable Energy*, 50:1095–1105, 2013.

[44] Agrim Sareen, Robert W Deters, Steven P Henry, and Michael S Selig. Drag reduction using riblet film applied to airfoils for wind turbines. *Journal of Solar Energy Engineering*, 136(2):021007, 2014.

[45] Kwing-So Choi. Effects of longitudinal pressure gradients on turbulent drag reduction with riblets. In *Turbulence Control by Passive Means*, pages 109–121. Springer, 1990.

[46] TV Truong and Ph Pulvin. Influence of wall riblets on diffuser flow. *Applied Scientific Research*, 46(3):217–227, 1989.

[47] LC Squire and AM Savill. Drag measurements on planar riblet surfaces at high subsonic speeds. *Applied Scientific Research*, 46(3):229–243, 1989.

[48] Stephan Klumpp, Thomas Guldner, Matthias Meinke, and Wolfgang Schröder. Riblets in a turbulent adverse-pressure gradient boundary layer. *AIAA paper 2010-4706*, 2010.

[49] Amy W Lang, Michael T Bradshaw, Jonathon A Smith, Jennifer N Wheelus, Philip J Motta, Maria L Habegger, and Robert E Hueter. Movable shark scales act as a passive dynamic micro-roughness to control flow separation. *Bioinspiration & biomimetics*, 9(3):036017, 2014.

[50] Brian Dean and Bharat Bhushan. Shark-skin surfaces for fluid-drag reduction in turbulent flow: a review. *Philosophical Transactions of the Royal Society A: Mathematical, Physical and Engineering Sciences*, 368(1929):4775–4806, 2010.

[51] DW Bechert, M Bruse, and W Hage. Experiments with three-dimensional riblets as an idealized model of shark skin. *Experiments in fluids*, 28(5):403–412, 2000.

[52] Yong Chae Jung and Bharat Bhushan. Biomimetic structures for fluid drag reduction in laminar and turbulent flows. *Journal of Physics: Condensed Matter*, 22(3):035104, 2010.

[53] GV Lauder, PGA Madden, JL Tangorra, E Anderson, and TV Baker. Bioinspiration from fish for smart material design and function. *Smart Materials and Structures*, 20(9):094014, 2011.

[54] Amy Warncke Lang and Pablo Hidalgo. Cavity flow characterization of the bristled shark skin microgeometry. *AIAA Paper*, 1107, 2009.

[55] Leah Mendelson, Amy Lang, and Drew Smith. Turbulence augmentation to achieve separation control over a bristled shark skin model. In *APS Division of Fluid Dynamics Meeting Abstracts*, volume 1, 2009.

[56] Joseph Smagorinsky. General circulation experiments with the primitive equations: I. the basic experiment*. *Monthly weather review*, 91(3):99–164, 1963.

[57] Parviz Moin and John Kim. Numerical investigation of turbulent channel flow. *Journal of fluid mechanics*, 118:341–377, 1982.

[58] Massimo Germano, Ugo Piomelli, Parviz Moin, and William H Cabot. A dynamic subgrid-scale eddy viscosity model. *Physics of Fluids A: Fluid Dynamics (1989-1993)*, 3(7):1760–1765, 1991.

[59] Alexandre Joel Chorin. Numerical solution of the navier-stokes equations. *Mathematics of computation*, 22(104):745–762, 1968.

[60] Liang Ge and Fotis Sotiropoulos. A numerical method for solving the 3d unsteady incompressible navier–stokes equations in curvilinear domains with complex immersed boundaries. *Journal of computational physics*, 225(2):1782–1809, 2007.

[61] Anvar Gilmanov and Fotis Sotiropoulos. A hybrid cartesian/immersed boundary method for simulating flows with 3d, geometrically complex, moving bodies. *Journal of Computational Physics*, 207(2):457–492, 2005.

[62] Youcef Saad and Martin H Schultz. Gmres: A generalized minimal residual algorithm for solving nonsymmetric linear systems. *SIAM Journal on scientific and statistical computing*, 7(3):856–869, 1986.

[63] Seokkoo Kang, Anne Lightbody, Craig Hill, and Fotis Sotiropoulos. High-resolution numerical simulation of turbulence in natural waterways. *Advances in Water Resources*, 34(1):98–113, 2011.

[64] Satish Balay, Shrirang Abhyankar, Mark F. Adams, Jed Brown, Peter Brune, Kris Buschelman, Victor Eijkhout, William D. Gropp, Dinesh Kaushik, Matthew G. Knepley, Lois Curfman McInnes, Karl Rupp, Barry F. Smith, and Hong Zhang. Petsc web page. `http://www.mcs.anl.gov/petsc`, 2014.

[65] Ulrike Meier Yang et al. Boomeramg: a parallel algebraic multigrid solver and preconditioner. *Applied Numerical Mathematics*, 41(1):155–177, 2002.

[66] I Borazjani and F Sotiropoulos. On the role of form and kinematics on the hydrodynamics of self-propelled body/caudal fin swimming. *The Journal of experimental biology*, 213(1):89–107, 2010.

[67] Thomas S Lund, Xiaohua Wu, and Kyle D Squires. Generation of turbulent inflow data for spatially-developing boundary layer simulations. *Journal of computational physics*, 140(2):233–258, 1998.

[68] DB Spalding. A single formula for the "law of the wall". *Journal of Applied Mechanics*, 28(3):455–458, 1961.

[69] Kunlun Liu and Richard H Pletcher. Inflow conditions for the large eddy simulation of turbulent boundary layers: a dynamic recycling procedure. *Journal of Computational Physics*, 219(1):1–6, 2006.

[70] CF Lange, F Durst, and Momentum Breuer. Momentum and heat transfer from cylinders in laminar crossflow at 10- 4 re 200. *International Journal of Heat and Mass Transfer*, 41(22):3409–3430, 1998.

[71] Joung-Ho Lee and Hyung Jin Sung. Effects of an adverse pressure gradient on a turbulent boundary layer. *International Journal of Heat and Fluid Flow*, 29(3):568–578, 2008.

[72] Joongcheol Paik, Cristian Escauriaza, and Fotis Sotiropoulos. On the bimodal dynamics of the turbulent horseshoe vortex system in a wing-body junction. *Physics of Fluids (1994-present)*, 19(4):045107, 2007.

[73] JC Lane and RI Loehrke. Leading edge separation from a blunt plate at low reynolds number. *Journal of Fluids Engineering*, 102(4):494–496, 1980.

[74] Terukazu Ota and Masaaki Itasaka. A separated and reattached flow on a blunt flat plate. *Journal of Fluids Engineering*, 98(1):79–84, 1976.

[75] Y Na and P Moin. Direct numerical simulation of a separated turbulent boundary layer. *Journal of Fluid Mechanics*, 374:379–405, 1998.

Appendix A

Transformation of the Navier-Stokes Equations

In this Appendix, we derive the Navier-Stokes equations of conservation of mass and momentum in generalized curvilinear coordinates. During the transformation between coordinate systems, one has the choice to either partially or fullly transform the Navier-Stokes equations. As described by Ge & Sotiropoulos [60], the partial transformation is chosen to avoid Christoffel symbols, which are a product of a full transformation, and as such, the full transformation becomes combersome and more expensive to calculate. A partial transformation is defined as one that transforms only independent variables, a full transformation however transforms both independent and dependent variables.

A.1 Continuity Equation

We begin by defining a general transformation,

$$\xi = \xi(x, y, z)$$

$$\eta = \eta(x, y, z)$$

$$\zeta = \zeta(x, y, z)$$

This transformation is essentially a mapping between the Cartesian coordinate system (that can have arbitrarily complex lines of constant ξ, η, ζ) to a curvilinear system that is regular and uniformly spaced in the virtual space. It is in this virtual space that the Navier-Stokes equations are solved.

To transform the governing equations, the differential operators must take a different form. First, the gradient operator is transformed by way of the chain rule,

$$\frac{\partial}{\partial x_j} = \frac{\partial}{\partial \xi_i}\frac{\partial \xi_i}{\partial x_j} = \frac{\partial}{\partial \xi_i}\xi_j^i$$

where repeated indices imply summation over $i = 1, 2, 3$ and ξ_j^i is termed the transformation metric. Using the gradient operator, the divergence operator can likewise be transformed as follows:

$$\begin{aligned}\nabla \cdot \vec{V} = \frac{\partial u}{\partial \xi}\xi_x + \frac{\partial u}{\partial \eta}\eta_x + \frac{\partial u}{\partial_e ta}\eta_x + \frac{\partial u}{\partial \zeta}\zeta_x \\ + \frac{\partial v}{\partial \xi}\xi_y + \frac{\partial v}{\partial \eta}\eta_y + \frac{\partial v}{\partial \zeta}\zeta_y \\ + \frac{\partial w}{\partial \xi}\xi_z + \frac{\partial w}{\partial \eta}\eta_z + \frac{\partial w}{\partial \zeta}\zeta_z \\ = \frac{\partial u_i}{\partial \xi_j}\xi_i^j\end{aligned} \tag{A.1}$$

Easily, we now transform the continuity equation,

$$\frac{\partial u_i}{\partial x_i} = 0 \implies \frac{\partial u_i}{\partial \xi_j}\xi_i^j = 0$$

Though, this form is not actually used. Instead we multiply and divide by J, the Jacobian of the transformation, and rewrite using the chain rule as,

$$\frac{J}{J}\frac{\partial u_i}{\partial \xi_j}\xi_i^j = J\left[\frac{\partial}{\partial \xi_j}\frac{(u_i\xi_i^j)}{J} - u_i\frac{\partial}{\partial \xi_j}\frac{\xi_i^j}{J}\right]$$

The Jacobian is defined as $J = |\partial(\xi_1, \xi_2, \xi_3)/\partial(x_1, x_2, x_3)|$. The last term on the right hand side is zero by way of a transformation metric property known as the conservation of metrics so that finally the conservation of mass takes the form,

$$J\frac{\partial}{\partial \xi_j}\frac{(u_i\xi_i^j)}{J} = J\frac{\partial U_i}{\partial \xi_i} = 0$$

taking note of the definition of the contravariant velocities, U_i. We note here that the Jacobian of the transformation is defined as the tensor,

$$J = \frac{\partial \xi_i}{\partial x_j}$$

The Jacobian physically represents the inverse of the computational cell volume.

A.2 Momentum Equations

For the sake of brevity, we only derive the x momentum equation, though it is similar for the other directions. This momentum equation in Cartesian coordinates is written as,

$$\frac{\partial u}{\partial t} + \frac{\partial}{\partial x}\left(u^2 + \frac{p}{\rho} - \nu\frac{\partial u}{\partial x}\right) + \left(uv - \nu\frac{\partial u}{\partial y}\right) + \left(uw - \nu\frac{\partial u}{\partial z}\right) = 0$$

where p is the static pressure, ρ is the density (which is constant since incompressible) and ν is the kinematic viscosity. First, we transform the convective terms on the left hand side (making use of the conservation of metrics and chain rule):

$$\frac{\partial u^2}{\partial x} + \frac{\partial uv}{\partial y} + \frac{\partial uw}{\partial z} =$$

$$= J\left[\frac{\partial}{\partial \xi}\frac{u^2\xi_x + uv\xi_y + uw\xi_z}{J} + \frac{\partial}{\partial \eta}\frac{u^2\eta_x + uv\eta_y + uw\eta_z}{J} + \frac{\partial}{\partial \zeta}\frac{u^2\zeta_x + uv\zeta_y + uw\zeta_z}{J}\right]$$

$$= J\frac{\partial}{\partial \xi_j}(u_i \cdot U_j)$$

Second, we transform the pressure term (making use of the conservation of metrics),

$$\frac{\partial (p/\rho)}{\partial x} = J\frac{\partial}{\partial \xi_j}\left(\frac{p\xi_i^j}{\rho J}\right)$$

Last, we transform the viscous terms as:

$$\nu\left(\frac{\partial^2 u}{\partial x^2} + \frac{\partial^2 u}{\partial y^2} + \frac{\partial^2 u}{\partial z^2}\right) = \nu\left(\frac{\partial}{\partial x_j}\left(\frac{\partial u_i}{\partial x_j}\right)\right) =$$

$$= \nu J \left[\frac{\partial}{\partial \xi_j} \left(\frac{\frac{\partial u_i}{\partial x_k}\xi_k^j + \frac{\partial u_i}{\partial x_k}\xi_k^j + \frac{\partial u_i}{\partial x_k}\xi_k^j}{J} \right) \right] =$$

$$= J \left[\frac{\partial}{\partial \xi_j} \left(\frac{\nu}{J} \left(g^{jk} \frac{\partial u_i}{\partial \xi_k} \right) \right) \right]$$

where

$$g^{jk} = \xi_l^j \xi_l^k$$

and are termed the contravariant metric tensors.

A.3 Flux Vector Format

The partially transformed Navier-Stokes equations can conveniently be written in flux vector format as follows:

$$\frac{1}{J}\Gamma\frac{\partial Q}{\partial t} + \frac{\partial E}{\partial \xi} + \frac{\partial F}{\partial \eta} + \frac{\partial G}{\partial \zeta} + \frac{\partial E_\nu}{\partial \xi} + \frac{\partial F_\nu}{\partial \eta} + \frac{\partial G_\nu}{\partial \zeta} = 0$$

where

$$\Gamma = \begin{pmatrix} 0 & 0 & 0 & 0 \\ 0 & 1 & 0 & 0 \\ 0 & 0 & 1 & 0 \\ 0 & 0 & 0 & 1 \end{pmatrix}$$

$$Q = \begin{pmatrix} p \\ u \\ v \\ w \end{pmatrix}$$

$$E = \frac{1}{J} \begin{pmatrix} U \\ uU + \frac{p}{\rho}\xi_x \\ vU + \frac{p}{\rho}\xi_y \\ wU + \frac{p}{\rho}\xi_z \end{pmatrix}$$

$$F = \frac{1}{J}\begin{pmatrix} V \\ uV + \frac{p}{\rho}\eta_x \\ vV + \frac{p}{\rho}\eta_y \\ wV + \frac{p}{\rho}\eta_z \end{pmatrix}$$

$$G = \frac{1}{J}\begin{pmatrix} W \\ uW + \frac{p}{\rho}\zeta_x \\ vW + \frac{p}{\rho}\zeta_y \\ wW + \frac{p}{\rho}\zeta_z \end{pmatrix}$$

$$E_\nu = \frac{\nu}{J}\begin{pmatrix} 0 \\ g^{11}\frac{\partial u}{\partial \xi} + g^{12}\frac{\partial u}{\partial \eta} + g^{13}\frac{\partial u}{\partial \zeta} \\ g^{11}\frac{\partial v}{\partial \xi} + g^{12}\frac{\partial v}{\partial \eta} + g^{13}\frac{\partial v}{\partial \zeta} \\ g^{11}\frac{\partial w}{\partial \xi} + g^{12}\frac{\partial w}{\partial \eta} + g^{13}\frac{\partial w}{\partial \zeta} \end{pmatrix}$$

$$F_\nu = \frac{\nu}{J}\begin{pmatrix} 0 \\ g^{12}\frac{\partial u}{\partial \xi} + g^{22}\frac{\partial u}{\partial \eta} + g^{23}\frac{\partial u}{\partial \zeta} \\ g^{12}\frac{\partial v}{\partial \xi} + g^{22}\frac{\partial v}{\partial \eta} + g^{23}\frac{\partial v}{\partial \zeta} \\ g^{12}\frac{\partial w}{\partial \xi} + g^{22}\frac{\partial w}{\partial \eta} + g^{23}\frac{\partial w}{\partial \zeta} \end{pmatrix}$$

$$G_\nu = \frac{\nu}{J}\begin{pmatrix} 0 \\ g^{13}\frac{\partial u}{\partial \xi} + g^{23}\frac{\partial u}{\partial \eta} + g^{33}\frac{\partial u}{\partial \zeta} \\ g^{13}\frac{\partial v}{\partial \xi} + g^{23}\frac{\partial v}{\partial \eta} + g^{33}\frac{\partial v}{\partial \zeta} \\ g^{13}\frac{\partial w}{\partial \xi} + g^{23}\frac{\partial w}{\partial \eta} + g^{33}\frac{\partial w}{\partial \zeta} \end{pmatrix}$$

Appendix B

Discretization of the Governing Equations

To numerically solve the conservation of mass and momentum, the transformed equations must be discretized both in time and in space. As originally proposed by Gilmanov & Sotiropoulos [61], CURVIB utilizes a hybrid staggered/non-staggered approach where the pressure and Cartesian velocities are stored at cell centers and the contravariant fluxes are stored at the cell faces in their respective directions. Here, we reprint the spatial discretizations first developed by Kang & Sotiropoulos [63].

B.1 Momentum Equations

B.1.1 Convective Term

First, the convective term is descretized as follows:

$$\frac{1}{J}\frac{\partial(U_j u_l)}{\partial \xi_j} = \frac{1}{J}\left(\frac{\partial(U_1 u_l)}{\partial \xi_1} + \frac{\partial(U_2 u_l)}{\partial \xi_2} + \frac{\partial(U_3 u_l)}{\partial \xi_3}\right)\Big|_{i+\frac{1}{2},j,k} \tag{B.1}$$

where i, j, k refer to the center of a given computational cell and $i+\frac{1}{2}$ denotes the cell's surface in the i direction. Here, each term is discretized as

$$\frac{\partial(U_1 u_l)}{\partial \xi_1}\Big|_{i+\frac{1}{2},j,k} = \frac{1}{2}\frac{\partial(U_1 u_l)}{\partial \xi_1}\Big|_{i,j,k} + \frac{1}{2}\frac{\partial(U_1 u_l)}{\partial \xi_1}\Big|_{i+1,j,k}$$

$$\frac{\partial(U_2 u_l)}{\partial \xi_2}\Big|_{i+\frac{1}{2},j,k} = \frac{1}{2}\frac{\partial(U_2 u_l)}{\partial \xi_2}\Big|_{i,j,k} + \frac{1}{2}\frac{\partial(U_2 u_l)}{\partial \xi_2}\Big|_{i+1,j,k}$$

$$\frac{\partial(U_3 u_l)}{\partial \xi_3}\Big|_{i+\frac{1}{2},j,k} = \frac{1}{2}\frac{\partial(U_3 u_l)}{\partial \xi_3}\Big|_{i,j,k} + \frac{1}{2}\frac{\partial(U_3 u_l)}{\partial \xi_3}\Big|_{i+1,j,k}$$

As mentioned, the contravariant fluxes are stored at the cell faces, so to obtain values at the cell centers (and likewise the Cartesian velocities), the following central differencing scheme is utilized:

$$\begin{aligned}\frac{\partial(U_1 u_l)}{\partial \xi_1}\Big|_{i,j,k} &= \frac{(U_1 u_l)\Big|_{i+\frac{1}{2},j,k} - (U_1 u_l)\Big|_{i-\frac{1}{2},j,k}}{\Delta\xi_1} \\ &= (U_1)\Big|_{i+\frac{1}{2},j,k}\frac{(u_l)\Big|_{i+1,j,k} + (u_l)\Big|_{i,j,k}}{2\Delta\xi_1} \\ &\quad -(U_1)\Big|_{i-\frac{1}{2},j,k}\frac{(u_l)\Big|_{i,j,k} + (u_l)\Big|_{i-1,j,k}}{2\Delta\xi_1}\end{aligned} \tag{B.2}$$

and similarly for the second and third terms on the right hand side of Equation B.1. The distance between lines of constant ξ (i.e., $\Delta\xi$) are equal to unity in the virtual space. Discretization is similar for other components of the contravariant velocity.

B.1.2 Diffusion Term

The diffusion term is discretized as follows:

$$\nu\frac{\partial}{\partial\xi_j}\left(\frac{g^{jm}}{J}\frac{\partial u_l}{\partial\xi_m}\right)\Big|_{i+\frac{1}{2},j,k} = \nu\left(\frac{\partial}{\partial\xi_1}\left(\frac{g^{1m}}{J}\frac{\partial u_l}{\partial\xi_m}\right) + \frac{\partial}{\partial\xi_2}\left(\frac{g^{2m}}{J}\frac{\partial u_l}{\partial\xi_m}\right) + \frac{\partial}{\partial\xi_3}\left(\frac{g^{3m}}{J}\frac{\partial u_l}{\partial\xi_m}\right)\right)\Big|_{i+\frac{1}{2},j,k}$$

and each term on the right hand side is discretized as

$$\frac{\partial}{\partial\xi_1}\left(\frac{g^{1m}}{J}\frac{\partial u_l}{\partial\xi_m}\right)\Big|_{i+\frac{1}{2},j,k} = \frac{1}{2}\frac{\partial}{\partial\xi_1}\left(\frac{g^{1m}}{J}\right)\Big|_{i+1,j,k} + \frac{1}{2}\frac{\partial}{\partial\xi_1}\left(\frac{g^{1m}}{J}\right)\Big|_{i,j,k}$$

$$\frac{\partial}{\partial\xi_2}\left(\frac{g^{2m}}{J}\frac{\partial u_l}{\partial\xi_m}\right)\Big|_{i+\frac{1}{2},j,k} = \frac{1}{2}\frac{\partial}{\partial\xi_2}\left(\frac{g^{2m}}{J}\right)\Big|_{i+1,j,k} + \frac{1}{2}\frac{\partial}{\partial\xi_2}\left(\frac{g^{2m}}{J}\right)\Big|_{i,j,k}$$

$$\frac{\partial}{\partial\xi_3}(\frac{g^{3m}}{J}\frac{\partial u_l}{\partial\xi_m})\Big|_{i+\frac{1}{2},j,k} = \frac{1}{2}\frac{\partial}{\partial\xi_3}(\frac{g^{3m}}{J})\Big|_{i+1,j,k} + \frac{1}{2}\frac{\partial}{\partial\xi_3}(\frac{g^{3m}}{J})\Big|_{i,j,k}$$

Now,

$$\frac{\partial}{\partial\xi_1}(\frac{g^{1m}}{J}\frac{\partial u_l}{\partial\xi_m})\Big|_{i,j,k} = \frac{\partial}{\partial\xi_1}\left(\frac{g^{11}}{J}\frac{\partial u_l}{\partial\xi_1} + \frac{g^{12}}{J}\frac{\partial u_l}{\partial\xi_2} + \frac{g^{13}}{J}\frac{\partial u_l}{\partial\xi_3}\right)\Big|_{i,j,k}$$

$$\frac{\partial}{\partial\xi_2}(\frac{g^{2m}}{J}\frac{\partial u_l}{\partial\xi_m})\Big|_{i,j,k} = \frac{\partial}{\partial\xi_2}\left(\frac{g^{21}}{J}\frac{\partial u_l}{\partial\xi_1} + \frac{g^{22}}{J}\frac{\partial u_l}{\partial\xi_2} + \frac{g^{23}}{J}\frac{\partial u_l}{\partial\xi_3}\right)\Big|_{i,j,k}$$

$$\frac{\partial}{\partial\xi_3}(\frac{g^{3m}}{J}\frac{\partial u_l}{\partial\xi_m})\Big|_{i,j,k} = \frac{\partial}{\partial\xi_3}\left(\frac{g^{31}}{J}\frac{\partial u_l}{\partial\xi_1} + \frac{g^{32}}{J}\frac{\partial u_l}{\partial\xi_2} + \frac{g^{33}}{J}\frac{\partial u_l}{\partial\xi_3}\right)\Big|_{i,j,k} \tag{B.3}$$

For brevity's sake, each term of the right hand side of Equation B.3 are discretized

$$\frac{\partial}{\partial\xi_1}(\frac{g^{11}}{J}\frac{\partial u_l}{\partial\xi_1})\Big|_{i,j,k} = \frac{(\frac{g^{11}}{J}\frac{\partial u_l}{\partial\xi_1})\Big|_{i+\frac{1}{2},j,k} - (\frac{g^{11}}{J}\frac{\partial u_l}{\partial\xi_1})\Big|_{i-\frac{1}{2},j,k}}{\Delta\xi_1}$$

$$\frac{\partial}{\partial\xi_1}(\frac{g^{12}}{J}\frac{\partial u_l}{\partial\xi_2})\Big|_{i,j,k} = \frac{(\frac{g^{12}}{J}\frac{\partial u_l}{\partial\xi_2})\Big|_{i+\frac{1}{2},j,k} - (\frac{g^{12}}{J}\frac{\partial u_l}{\partial\xi_2})\Big|_{i-\frac{1}{2},j,k}}{\Delta\xi_1}$$

$$\frac{\partial}{\partial\xi_1}(\frac{g^{13}}{J}\frac{\partial u_l}{\partial\xi_3})\Big|_{i,j,k} = \frac{(\frac{g^{13}}{J}\frac{\partial u_l}{\partial\xi_3})\Big|_{i+\frac{1}{2},j,k} - (\frac{g^{13}}{J}\frac{\partial u_l}{\partial\xi_3})\Big|_{i-\frac{1}{2},j,k}}{\Delta\xi_1}$$

and where

$$\frac{\partial u_l}{\partial\xi_1}\Big|_{i+\frac{1}{2},j,k} = \frac{u_l\Big|_{i+1,j,k} - u_l\Big|_{i,j,k}}{\Delta\xi_1}$$

$$\frac{\partial u_l}{\partial\xi_2}\Big|_{i+\frac{1}{2},j,k} = \frac{u_l\Big|_{i+1,j+1,k} + u_l\Big|_{i,j+1,k} - u_l\Big|_{i+1,j,k} - u_l\Big|_{i,j,k}}{4\Delta\xi_2}$$

$$\frac{\partial u_l}{\partial\xi_3}\Big|_{i+\frac{1}{2},j,k} = \frac{u_l\Big|_{i+1,j+1,k} + u_l\Big|_{i,j+1,k} - u_l\Big|_{i+1,j,k} - u_l\Big|_{i,j,k}}{4\Delta\xi_3}$$

Terms not detailed here can be discretized in a similar manner.

B.1.3 Pressure Gradient Term

Lastly, we discretize the pressure gradient term as follows:

$$\frac{1}{J}\frac{\partial}{\partial\xi_j}\left(\frac{\xi_l^j p}{J}\right)\Big|_{i+\frac{1}{2},j,k} = \left(g^{11}\frac{\partial p}{\partial\xi_1} + g^{12}\frac{\partial p}{\partial\xi_2} + g^{13}\frac{\partial p}{\partial\xi_3}\right)\Big|_{i+\frac{1}{2},j,k}$$

where each term on the right hand side is dicretized using a central differencing scheme

$$\left(\frac{\partial p}{\partial\xi_1}\right)\Big|_{i+\frac{1}{2},j,k} = \frac{p\Big|_{i+1,j,k} - p\Big|_{i,j,k}}{\Delta\xi_1}$$

$$\left(\frac{\partial p}{\partial\xi_2}\right)\Big|_{i+\frac{1}{2},j,k} = \frac{p\Big|_{i+1,j+1,k} + p\Big|_{i,j+1,k} - p\Big|_{i+1,j,k} - p\Big|_{i,j,k}}{4\Delta\xi_2}$$

$$\left(\frac{\partial p}{\partial\xi_3}\right)\Big|_{i+\frac{1}{2},j,k} = \frac{p\Big|_{i+1,j+1,k} + p\Big|_{i,j+1,k} - p\Big|_{i+1,j,k} - p\Big|_{i,j,k}}{4\Delta\xi_3}$$

The discretization for the pressure terms in the j,k directions are similar.

B.2 Poisson Equation

The Poisson equation ensures that the Navier-Stokes equations remain divergence free. Equation 2.12 is repeated here for convenience:

$$-J\frac{\partial}{\partial\xi_i}\left(\frac{1}{\rho}\frac{\xi_k^i}{J}\frac{\partial}{\partial\xi_j}\left(\frac{\xi_k^i\phi}{J}\right)\right) = \frac{3}{2\Delta t}J\frac{\partial U_j^*}{\partial\xi_j}$$

As detailed originally by Seokoo & Sotiropoulos [63], to discretize the left hand side, we first simplify the term via the chain rule and conservation of metrics:

$$J\frac{\partial}{\partial\xi_m}\left(\frac{1}{\rho}\frac{\xi_l^m}{J}\frac{\partial}{\partial\xi_n}(\frac{\xi_l^n\Pi}{J})\right)\Big|_{i,j,k} = J\frac{\partial}{\partial\xi_m}\left(\frac{1}{\rho}g^{mn}\frac{\partial\Pi}{\partial\xi_n}\right)\Big|_{i,j,k}$$

where $g^{mn} = \xi_l^m\xi_l^n$. For the sake of brevity, we show the discretization for the ξ_1 direction as follows:

$$\frac{\partial}{\partial \xi_1}\left(\frac{1}{\rho}g^{11}\frac{\partial \Pi}{\partial \xi_1}\right)\Big|_{i,j,k} = \frac{\left(\frac{1}{\rho}g^{11}\frac{\partial \Pi}{\partial \xi_1}\Big|_{i+\frac{1}{2},j,k}\right) - \left(\frac{1}{\rho}g^{11}\frac{\partial \Pi}{\partial \xi_1}\Big|_{i-\frac{1}{2},j,k}\right)}{\Delta \xi_1}$$

$$\frac{\partial}{\partial \xi_1}\left(\frac{1}{\rho}g^{12}\frac{\partial \Pi}{\partial \xi_2}\right)\Big|_{i,j,k} = \frac{\left(\frac{1}{\rho}g^{12}\frac{\partial \Pi}{\partial \xi_2}\Big|_{i+\frac{1}{2},j,k}\right) - \left(\frac{1}{\rho}g^{12}\frac{\partial \Pi}{\partial \xi_2}\Big|_{i-\frac{1}{2},j,k}\right)}{\Delta \xi_1}$$

$$\frac{\partial}{\partial \xi_1}\left(\frac{1}{\rho}g^{13}\frac{\partial \Pi}{\partial \xi_3}\right)\Big|_{i,j,k} = \frac{\left(\frac{1}{\rho}g^{13}\frac{\partial \Pi}{\partial \xi_3}\Big|_{i+\frac{1}{2},j,k}\right) - \left(\frac{1}{\rho}g^{13}\frac{\partial \Pi}{\partial \xi_3}\Big|_{i-\frac{1}{2},j,k}\right)}{\Delta \xi_1}$$

and, in the i direction,

$$\left(\frac{\partial \Pi}{\partial \xi_1}\right)\Big|_{i+\frac{1}{2},j,k} = \frac{\Pi\Big|_{i+1,j,k} - \Pi\Big|_{i,j,k}}{\Delta \xi_1}$$

$$\left(\frac{\partial \Pi}{\partial \xi_2}\right)\Big|_{i+\frac{1}{2},j,k} = \frac{\Pi\Big|_{i+1,j+1,k} + \Pi\Big|_{i,j+1,k} - \Pi\Big|_{i+1,j,k} - \Pi\Big|_{i,j,k}}{4\Delta \xi_2}$$

$$\left(\frac{\partial \Pi}{\partial \xi_2}\right)\Big|_{i+\frac{1}{2},j,k} = \frac{\Pi\Big|_{i+1,j,k+1} + \Pi\Big|_{i,j,k+1} - \Pi\Big|_{i+1,j,k} - \Pi\Big|_{i,j,k}}{4\Delta \xi_3}$$

Finally, the right hand side of the Poisson equation is discretized using central differencing as follows:

$$\frac{\partial U_m^*}{\partial_m}\Big|_{i,j,k} = \frac{U_1^*\Big|_{i+\frac{1}{2},j,k} - U_2^*\Big|_{i-\frac{1}{2},j,k}}{\Delta \xi_1} + \frac{U_1^*\Big|_{i,j+\frac{1}{2},k} - U_2^*\Big|_{i,j-\frac{1}{2},k}}{\Delta \xi_2} + \frac{U_1^*\Big|_{i,j,k+\frac{1}{2}} - U_2^*\Big|_{i,j,k-\frac{1}{2}}}{\Delta \xi_3}$$

Appendix C

A Framework for Dynamic Denticles

During our research concerning sharkskin, we originally planned to simulate swimming (i.e., dynamic) sharkskin. Here, is presented the framework we developed to simulate moving denticles.

C.1 Computational Setup

Shark swimming can be mimicked by simulating flow over a wavy surface with some specified frequency, ω, and wavelength, λ. There are two methods to simulate turbulent flow over a wavy surface. The first utilizes an Arbitrary Lagrangian Eulerian (ALE) method. When using this method, the mesh can move with the fluid (Lagrangian) or stay fixed (Eulerian) or some combination of either. The ALE method has the obvious advantage of obtaining high resolution grids near arbitrarily moving surfaces, though it also has its disadvantages–primarily that is more complicated than a simple Eulerian method and the moving mesh must be recreated every timestep. When using an Immersed Boundary (IB) method, the recreation of a background mesh can be computationally expensive due to the IB search (i.e., classification of IB nodes). The second method to simulate flow over a wavy surface is to maintain a stationary grid (an Eulerian method) and adjusting the Navier-Stokes equations such that the simulation takes place in a moving frame of reference. The

moving frame of reference type of simulation was chosen for this framework since it is far more simple to implement and one saves computational expense not having to recreate the background mesh every timestep. Now, although the wavy surface remains fixed in time, any denticles mounted on the surface do not. Each denticle mounted to the epidermis must move at the wave speed, c. Figure C.1 is a plot of a wavy surface computational domain that is static. In Figure C.1a, we plot the instantaneous position of the denticles, while in Figure C.1b, we show how the denticles move over the wavy surface and their time-averaged positions.

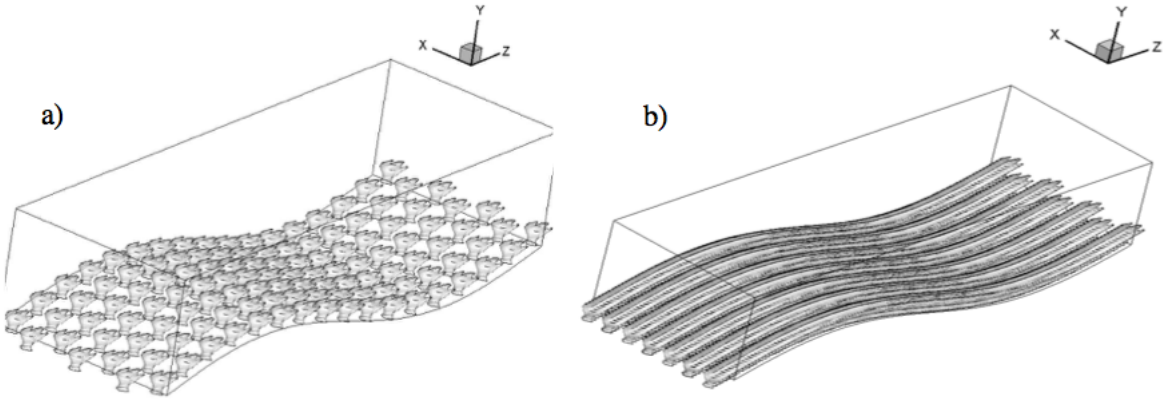

Figure C.1: a) Sharkskin denticles mounted on a static wavy surface at some instant of time. b) Time-averaged denticle positions on a static wavy surface.

In order to validate the moving frame of reference simulation method, we created the computational domain seen in Figure C.2. This is the same domain as that used in the simulation by Shen et al. [18], chosen for validation purposes. Equation C.1 describes the equation of the wavy surface.

$$y(x) = asin(k(x - ct)) \tag{C.1}$$

where the amplitude $a = 0.1$, wavenumber $k = 2\pi/\lambda$, wavelength $\lambda = 2.512$, and the wave speed is $c/W = 0.4$. The mean external streamwise velocity is defined as W. The Reynolds number for this validation case is $Re = \lambda W/\nu = 10,170$.

In order to perform this moving frame of reference simulation, the Navier-Stokes equations had to be modified. Overall, the modification is simple, the wave speed is added to

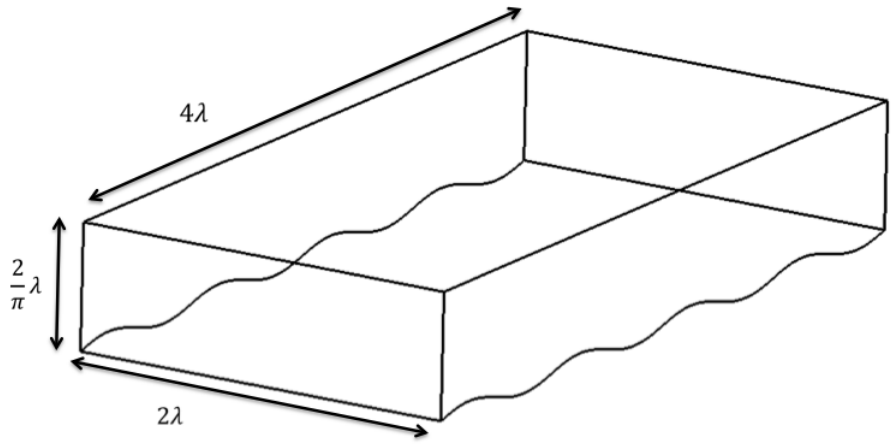

Figure C.2: Compuational domain size. Equation C.1 describes the wavy surface shape.

the appropriate velocity component. However, their is an additional term created in the momentum equations, specifically the convective term which is shown in Equation C.2.

$$(u_j + c_j)\frac{\partial(u_i + c_i)}{\partial x_j} = u_i\frac{\partial u_j}{\partial x_i} + c_i\frac{\partial u_j}{\partial x_i} \tag{C.2}$$

where c_i is the wavespeed vector. The second term of the right hand side is the new term. This term was discretized and added to the momentum equation. The governing equations were solved using LES with a dynamic Smagorinsky subgrid stress model. Periodic boundary conditions were employed in the streamwise and spanwise directions. The slip boundary condition was employed at the bottom of the domain. The velocity given to the surface varied along the streamwise direction as the derivative of Equation C.1 plus the convective velocity. Finally, a stress-free boundary condition was employed at the top of the domain.

C.2 Validation Case Results

As validation for the moving frame of reference simulation method, we present the following time-averaged results. Figure C.3 plots time-averaged streamlines downstream of a wave. The present simulation results are shown in the top frame and the results of Shen et al. [18] are in the bottom frame. Very good agreement is seen between the two simulations in

terms of location of the recirculation zone.

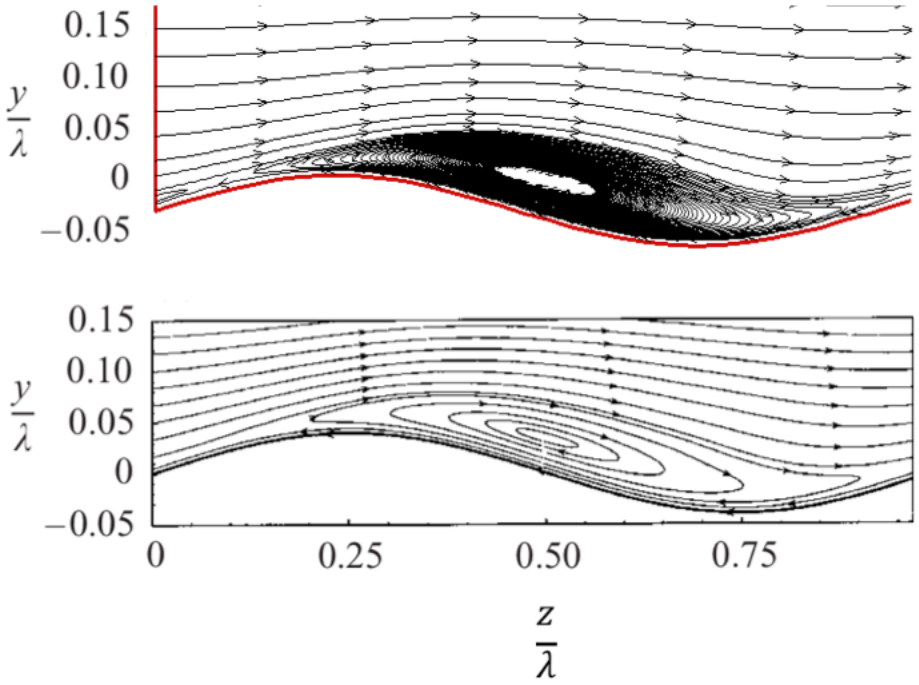

Figure C.3: Top) Present results of time-averaged streamlines. Bottom) Comparable computational data from Shen et al. [18].

Figure C.4 plots profiles of mean streamwise velocity, plotted in wall coordinates. Four different streamwise locations were sampled, which are specified in the inset. Excellent agreement is obtained when comparing two data sets.

We also compared turbulence statistics, which are not shown here, that also agreed well with Shen et al. [18]. With these results, we concluded that our implementation of the moving frame of reference method was validated.

In regards to simulating sharkskin, there are two important considerations. First is that shark undulation wavelength and frequency can vary and may be difficult to know without experimental knowledge. Second, it is very likely that the wavelength is much, much greater than the length of an individual denticle. In fact, it may be so great a ratio that one might approximate swimming sharkskin with a flatplate simulation. The characteristic length of a denticle is about 100 microns, whereas the wavelength of undulation is likely near a

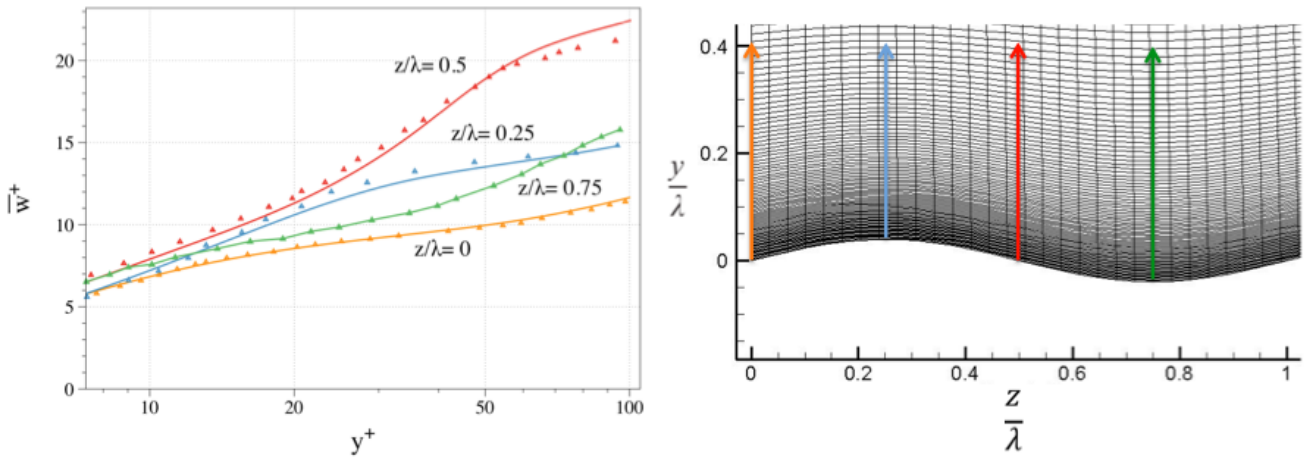

Figure C.4: Top) Present results of time-averaged streamlines. Bottom) Comparable computational data from Shen et al. [18].

meter. Whatever the exact ratio between denticle size and wavelength may be, it is certain that it is large and that to simulate the undulation, many denticles would be required. That corresponds to a computationally expensive simulation.